Advances in Raman and Surface-Enhanced Raman Spectroscopy: Instrumentation, Plasmonic Engineering and Biomolecular Sensing

A Dissertation

Presented to

the Faculty of the Department of Electrical and Computer Engineering

University of Houston

In Partial Fulfillment

of the Requirements for the Degree

Doctor of Philosophy

in Electrical and Computer Engineering

by

Ji Qi

August 2014

Advances in Raman and Surface-Enhanced Raman Spectroscopy:

Instrumentation, Plasmonic Engineering and Biomolecular Sensing

_____

Ji Qi

Approved

_____

Chair of the Committee
Wei-Chuan Shih, Assistant Professor,
Electrical and Computer Engineering

Committee Members:

_____

John C. Wolfe, Professor,
Electrical and Computer Engineering

_____

Zhu Han, Associate Professor,
Electrical and Computer Engineering

_____

Kirill Larin, Associate Professor,
Biomedical Engineering

_____

Richard C. Willson, Professor,
Chemical and Biomolecular Engineering

_____

Suresh K. Khator, Associate Dean,
Cullen College of Engineering

_____

Badrinath Roysam, Professor and Chair
Electrical and Computer Engineering

Acknowledgements

I would like to express my most sincere gratitude to my research advisor, Dr. Wei-Chuan Shih, for his continuous support and constructive guidance. I have been fortunate to have an advisor who always keeps me on the right path. I have learned from him how to be an excellent scientist, and at the same time an excellent engineer.

I would also like to thank Dr. John Wolfe, who helped me in my research from start to end. His collaboration was invaluable. I am also very grateful to Dr. Richard Willson, who provided strong support and guidance in the DNA biosensing project. I appreciate Dr. Kirill Larin, who provided support and guidance for our tissue classification work. I also would like to thank Dr. Badrinath Roysam and Dr. Zhu Han for their feedback and encouragement. Again, I would like to thank all of my committee members for their patience, guidance, and understanding throughout the course of this research.

My graduate studies are impossible without the help I constantly obtained from my colleagues. I would like to thank Dr. Jianbo Zeng, Dr. Ming Li, Fusheng Zhao, Jingting Li, and Pratik Motwani for their constant help and support. I enjoyed working with them.

Finally, I want to express my gratitude to my parents. Without their endless support and love, I would not have been the person I am. I also want to thank all my friends for their encouragement and support.

Advances in Raman and Surface-Enhanced Raman Spectroscopy: Instrumentation, Plasmonic Engineering and Biomolecular Sensing

An Abstract

of a

Dissertation

Presented to

the Faculty of the Department of Electrical and Computer Engineering

University of Houston

In Partial Fulfillment

of the Requirements for the Degree

Doctor of Philosophy

in Electrical and Computer Engineering

by

Ji Qi

August 2014

Abstract

Raman spectroscopy is a powerful technique for label-free molecular sensing and imaging in various fields. High molecular specificity, non-invasive sampling approach and the need for little or no sample preparation make Raman spectroscopy uniquely advantageous compared to other analytical techniques. However, Raman spectroscopy suffers from the intrinsic limitation of weak signal intensity. Therefore, time-sensitive studies such as diagnosis and clinical applications require improving the throughput of Raman instrumentation. Alternatively, surface-enhanced Raman scattering (SERS) improves the sensitivity by 10^6 to 10^{14} times, making the weak Raman intensity no longer a limitation. Nevertheless, it is still a big challenge to engineer plasmonic substrates with high SERS enhancement, good uniformity and reproducibility.

This thesis presents advances in: (1) Raman instrumentation towards high-throughput, environmental, biological and biomedical analysis; (2) SERS substrates with high enhancement factor (EF), uniformity and reproducibility; (3) biosensing applications including imaging of cell population and detection of biomolecules towards high time efficiency and sensitivity. In Raman instrumentation, we have built a high-throughput line-scan Raman microscope system and a novel parallel Raman microscope based on multiple-point active-illumination and wide-field hyperspectral data collection. Using the line-scan Raman microscope, we have performed chemical imaging of intact biological cells at the cell population level. We have also demonstrated more flexibility and throughput from the active-illumination Raman microscope in rapid chemical identification and screening of micro and nanoparticles and bacterial spores. Both Raman microscopes have been used to evaluate the large-area SERS uniformity of DC-sputtered

gold nanoislands, a low-cost means to fabricate plasmonic substrates. In plasmonic engineering, we have introduced patterned nanoporous gold nanoparticles that feature 3-dimensional mesoporous network with pore size on the order of 10 nm throughput the sub-wavelength nanoparticles. We showed that the plasmonic resonance can be tuned by geometrical engineering of either the external nanoparticle size and shape or the nanoporous network. As an example, we have developed disk-shaped entities, also known as nanoporous gold disks (NPGD) with highly uniform and reproducible SERS EF exceeding 10^8. Label-free, multiplexed molecular sensing and imaging has been demonstrated on NPGD substrates. Using the line-scan Raman microscope and the NPGD substrates, we have successfully developed a label-free DNA hybridization sensor at the single-molecule level in microfluidics. We have observed discrete, individual DNA hybridization events by *in situ* monitoring the hybridization process using SERS.

The advances and promising results presented in this thesis demonstrate potential impact in Raman/SERS imaging and sensing in environmental, biological and biomedical applications.

Table of Contents

List of Figures

List of Tables

Chapter 1 Motivation and Scope

Raman spectroscopy, as a type of vibrational spectroscopy, has proven to be a powerful and versatile tool in various fields, including biotechnology, environmental monitoring, food safety, forensic science, medical and clinical chemistry, diagnostics, pharmaceutical, material science, surface analysis, etc [1]. A tiny amount of light experiences energy transfer to molecules via inelastic scattering, resulting in a frequency shift of the scattered light. The frequency spectrum, known as Raman spectrum, that gives a unique fingerprint since the frequency shifts are distinct for each molecule, allows simple identification and interpretation of the chemical composition of analytes. Raman spectroscopy has been used as quantitative analysis tool since the intensity of Raman signal is linear to the concentration of the analyte. Besides, Raman spectroscopy provides many advantages over other analytical techniques such as fluorescence, primarily due to the label-free and non-invasive sampling approach as well as the capability of *in situ* monitoring. However, Raman scattering is an extremely weak phenomenon, only 1 in 10^8 of incident photons is Raman scattered [2]. Thus, Raman spectroscopy suffers from its intrinsic limitation of weak Raman signal that prevent the applications in large area mapping and time-resolved studies. The discovery of surface-enhanced Raman scattering (SERS) can alleviate this significant limitation. With SERS, the Raman intensity can be enhanced by 6 to 14 orders of magnitude, which improves the limit of detection (LOD) and time efficiency significantly. The enhancement effect requires nanostructured metal surface, known as SERS-active substrates. Nevertheless, it is still a big challenge to prepare the appropriate SERS-active substrates with high enhancement, good uniformity and reproducibility. Besides, SERS is a near field effect [3, 4], only Raman signals from

analytes reside within a few nanometers can be enhanced. In contract, Raman spectroscopy probes the analytes within a three dimensional focal volume. Thus SERS cannot take the place of Raman spectroscopy in some applications such as tissue and cell imaging.

Therefore the work in this thesis develops novel Raman instrumentation for high-throughput large-area imaging, versatile SERS-active substrates, and applications of Raman spectroscopy and SERS in rapid chemical mapping, diagnosis, studying biological process, etc. In design of novel Raman instrumentation, parallel and hyperspectral collection of multiple Raman spectra by a two-dimensional charge-coupled-device (CCD) is an efficient means to high throughput Raman imaging. Indeed, previous investigations have demonstrated line-scan Raman microscopes with the parallel collection approach [5-8]. One goal of this research is the improvement of line-scan Raman microscope to achieve higher throughput and evaluation of the performance in chemical mapping and biological studies. Since line-scan Raman microscope is not efficient in the case of sparse sample, we also aim to develop Raman microscope with more flexibility and higher throughput by using active-illumination enabled by spatial light modulator (SLM). The parallel Raman microscope is realized by projecting a multiple-point, semi-arbitrary laser illumination pattern using a SLM coupled with wide-field hyperspectral imaging collection. The line-scan and active-illumination Raman microscopes have been applied in several research projects, including rapid identification of polymer microspheres, large-area chemical mapping, performance and uniformity evaluation of SERS substrates, and imaging of biological cells.

In SERS substrates development, the goal is to obtain SERS substrates with large enhancement factor (EF), good stability, uniformity and reproducibility [9]. Besides, cost-effective fabrication process is also desirable. To meet these requirements, we focused on nanoporous gold (NPG) produced by dealloying. Our primary contribution is to pattern NPG thin films into sub-wavelength units. For example, NPG disks (NPGD), a SERS substrates, has been fabricated using nanosphere lithography. The large EF and uniformity have been evaluated by the home built line-scan Raman microscope. NPGD has been successfully applied in various research projects, including detection of biomolecules such as urea and acetaminophen, and *in situ* monitoring of DNA hybridization.

The thesis is divided into 10 chapters. The motivation and scope of the thesis are described in Chapter 1. A general introduction to the background is presented in Chapter 2, describing the basic principle of Raman spectroscopy and SERS, advancements in Raman instrumentation, and current status of SERS substrates. In Chapter 3, the home-built line-scan Raman microscope and its performance on various applications are presented. In Chapter 4, the active-illumination Raman microscope based on multiple-point illumination patterns and wide-field hyperspectral collection is demonstrated. Several applications including identification of polymer microspheres are shown. Further characterization and applications are described in Chapter 5. Chapter 6 discusses tissue analysis and tumor margin detection using Raman spectroscopy combined with optical coherence tomography (OCT). Characterization DC-sputtered gold nanoislands (GNI) in terms of EF, uniformity by both line-scan and active-illumination microscopes is presented in Chapter 7. Chapter 8 describes the NPGD SERS substrates, including the

determination of EF, evaluation of uniformity, and applications in biomolecular sensing. In Chapter 9, *in situ* monitoring of single DNA hybridization is demonstrated using NPGD. Chapter 10 briefly summarized the research work described in this thesis and outlines the future work.

Chapter 2 Introduction

2.1 Raman Scattering and Raman Spectroscopy

Raman scattering, an inelastic light scattering phenomenon, was discovered by C. V. Raman in 1928. It occurs when photons incident on a molecule and interact with the electron cloud of the molecule, resulting an energy transfer between photon and molecule and scattered photon with different frequency from the incident photon. The interpretation of Raman scattering phenomenon in classical electromagnetic theory is the perturbation of the molecule's electron field by the interaction with the incident photon. A dipole moment (P) is induced in the molecule by the oscillating electric field of the incident photon. It is linear with the polarizability, α, and the incident electric field, E. The induced dipole then radiates scattered light, with or without energy transfer with vibrations in the molecule. Raman scattering occurs only when a molecule vibration changes the polarizability of the molecule [10]. While in quantum mechanics, the Raman effect describes a scattering interaction between light and matter. Figure 2.1 gives a schematic diagram of energy level transitions for Raman scattering. When monochromatic light of energy $h\nu_0$ encounters a molecule, most of the scattered photons have the same frequency. This is known as Rayleigh scattering. While there is a small fraction of the photons (about 1 in 10^8 photons) undergoing inelastic scattering, of which the frequency is different from the incident photons, known as Raman scattering. A molecule may begin in the vibrational ground state and proceed via the virtual state to an excited vibrational state, called Stokes-Raman scattering. In Stokes-Raman scattering, the incident photon loses energy by exciting a vibration within the encountered molecule. In

this case, the Raman scattered photons have an energy of $h(v_0 - v_1)$, where v_1 is a vibrational frequency of the molecule. On the contrary, the molecule may begin in an excited vibrational state and proceed to the vibrational ground state via the virtual state. This process is called anti-Stokes Raman scattering and photons gain energy from the molecular vibrations. Thus the scattered photon has more energy, i.e., $h(v_0 + v_1)$, than the incident photon. According to the Boltzmann distribution, at room temperature, the population of molecules at ground state is much larger than that at excited states. Therefore, more Stokes photons are observed in Raman spectroscopy.

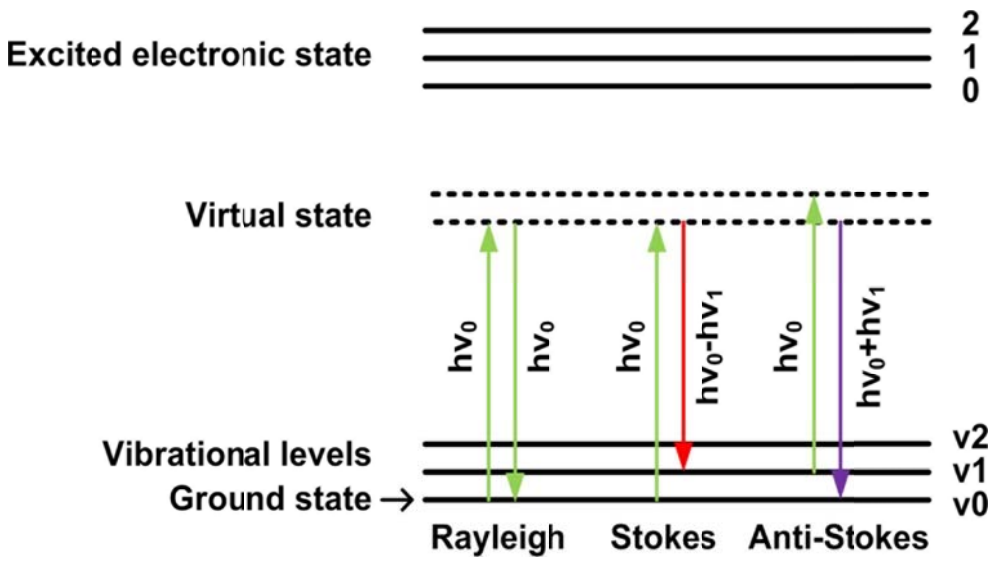

Figure 2.1 The energy level diagram of Raman scattering.

In summary, Raman spectroscopy probes molecular vibrations and provides the "finger print" due to distinct molecular structure (chemical bonds). It is not limited to intra-molecular vibrations. Other vibrations and motions, such as crystal lattice vibrations and rotation structures of gas, are also Raman active. Therefore Raman spectroscopy is widely applied in polymer study and the semiconductor industry. Compared to FTIR and

NIR absorption techniques that also probe molecular vibrations, Raman spectroscopy provides narrow linewidths and is not sensitive to water content. Furthermore, Raman spectroscopy is free of photobleaching and it does not require staining or fluorescence labeling. These attractive features of Raman spectroscopy make it a versatile tool in biological study and molecular sensing.

2.2 Surface-enhanced Raman Spectroscopy

The Raman scattering from a molecule located within a few nanometers of a nanostructured metal surface can be enhanced by 10^6 to 10^{14} times. This is known as surface-enhanced Raman scattering. SERS is first observed by Martin Fleischmann *et al.* from pyridine adsorbed on electrochemically roughened silver electrode in 1974 [11]. Later in 1977, Van Duyne and Creighton noted that the 10^6 enhancement of Raman signal was not because of the increased number of molecules adsorbed on silver electrode [12]. Subsequent studies show some distinct features of SERS as described in the following. First, SERS is surface sensitive and distance dependent [3, 4, 13-15]. Molecules in close proximity to the surface experience the largest enhancement. This enhancement decreases rapidly with the increasing distance between molecule and substrate. Second, SERS occurs on metal surface with micro- to nano-scale structures. Larger enhancements of signals are observed on noble metals, especially on silver and gold [16]. Flat and smooth metal surface does not provide effective enhancement. Third, SERS spectra are slightly different from normal Raman spectra because the molecular symmetry changed when a molecule adsorbs on the metal surface. It is possible that forbidden Raman bands in normal Raman scattering appear in SERS spectra [17].

Currently, there are two mechanisms to interpret SERS phenomenon. One is electromagnetic (EM) mechanism in which Raman scattering intensity scales as E^4, the corresponding enhancement is of order 10^4 [3, 4, 16, 18, 19]. The other one is chemical enhancement or charge transfer (CT) mechanism that contributes 10^2 to the total enhancement [3, 4, 20, 21]. In the EM mechanism, the enhancement originates from the localized surface plasmon resonance (LSPR) at the metal surface excited by the incident light, resulting in amplification of the incident photons as well as the scattered photons. LSPR occurs when the collective oscillation of valence electrons in metal surface is resonant with the frequency of the incident photons. And the LSPR effect decays rapidly from the nanostrucutres.

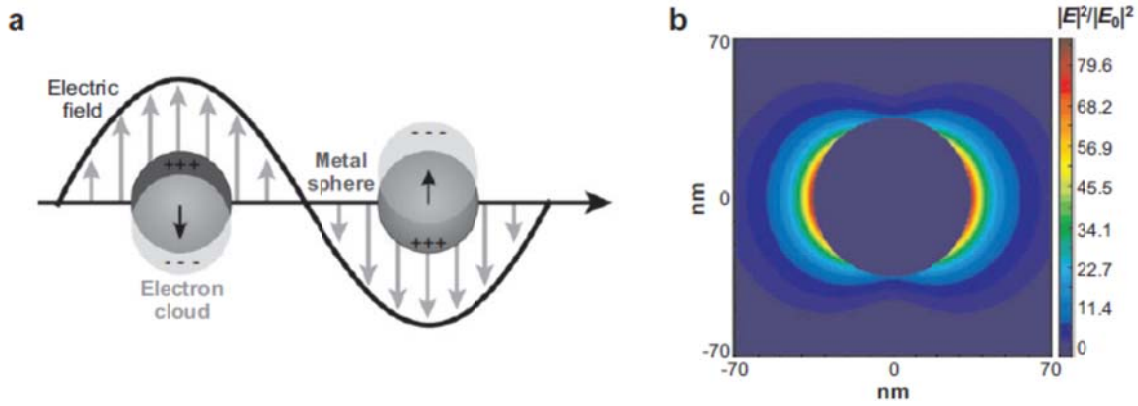

Figure 2.2 (a) Illustration of the LSRP effect. (b) Local E-filed near a spherical silver nanoparticle of 35-nm radius in vacuum. $|E|^2/|E_0|^2$ contours for a wavelength corresponding to plasmon resonance. Peak $|E|^2/|E_0|^2$~85.

Figure 2.2 (a) shows the local electric-field (E-field) distribution due to LSPR and (b) an example of a spherical silver NP of 35 nm radius in vacuum [4]. When the

electromagnetic field incident on spherical metal nanoparticles, the resulting electric field around the nanoparticle (NP) is expressed as

$$E_{out}(x,y,z) = E_0\hat{z} - \alpha E_0\left[\frac{\hat{z}}{r^3} - \frac{3z}{r^5}(x\hat{x} + y\hat{y} + z\hat{z})\right], \quad (1)$$

where x, y and z are Cartesian coordinates; r is the radical distance; $\hat{x}$, $\hat{y}$ and $\hat{z}$ are the unit vector in Cartesian coordinates; α is the polarizability of the metal nanoparticle and can be expressed as

$$\alpha = a^3 \frac{\varepsilon_{in} - \varepsilon_{out}}{\varepsilon_{in} + 2\varepsilon_{out}}, \quad (2)$$

where a is the radius of the nanoparticle, ε_{in} and ε_{out} are the dielectric constants of the metal particle and the surrounding medium, respectively [3, 4]. For metal nanoparticles, ε_{in} is greatly dependent on the incident wavelength. The LSPR effect occurs when $\varepsilon_{in} \approx \varepsilon_{out}$. The local field intensity enhancement factor (LFIEF) is defined as $|E_{out}|^2/|E_0|^2$. Since both the incident field and scattered field are amplified, the SERS enhancement factor (EF) is equal to LFIEF(ω_L)× LFIEF(ω_S), where ω_L and ω_S are the frequency of incident and scattered photons, respectively. Moreover, the difference between ω_L and ω_S is very small, i.e., $\omega_L \approx \omega_S$. Therefore the SERS EF can be expressed as

$$EF \approx LFIEF^2(\omega_L) = \frac{|E_{out}|^4}{|E_0|^4}. \quad (3)$$

This implies the Raman scattering intensity scales as E^4 due to LSPR.

2.3 Raman Instrumentation

Raman spectroscopy has been a powerful technique for biological study and generating chemical images based on the unique Raman spectrum from the molecule. The first Raman microscope for imaging was first proposed in 1975 by Delhaye and Dhamelincourt [22]. In general, the various Raman imaging approaches may be categorized into three types: wide-field, point-scan and line-scan.

2.3.1 Wide-field Imaging

In wide-field imaging, the entire sample field of view is illuminated with laser light and the Raman scattered light is projected onto a two-dimensional charge-coupled device (CCD). A wide-aperture filter is employed before CCD to study discrete wavenumbers instead of a full range spectrum [23, 24]. Liquid-crystal tunable filters (LCTFs) are electro-optically tunable devices that allow wavelength selection defined by users [25]. Other wide-field imaging approaches include Hadamard transform imaging [26] and fiber-bundle image compression method [27]. In Hadamard transform imaging, an entire Raman image is reconstructed from a series of images recorded with different masks. In fiber-bundle image compression method, two spatial dimensions and one spectral dimension of data are collected simultaneously from a grid of sample points with fiber arrays. Wide-field Raman imaging systems provide diffraction-limited spatial resolution. In contrast to point-scan and line-scan approaches, wide-field Raman imaging requires serial sectioning and digital deconvolution techniques to achieve same results. It is noted that serial tuning of LCTF band-pass is needed in order to obtain full spectral range information, which dramatically impede the overall throughput.

2.3.2 Point-scan Mapping

In point-scan mapping scheme, a tightly focused laser spot is scanned sequentially across a sample surface. This is known as raster scan [28]. A Raman spectrum is acquired at each spatial location to generate a hyperspectral data cube. Current point-scan Raman microscopes employ a confocal configuration to improve the spatial resolution as well as the axial resolution. Most commercial Raman microscopes employ the point-scan scheme. The actual spatial resolution depends on the sampling interval between adjacent laser spot. A smaller sampling interval increases the spatial resolution, and on the other hand, it also increases the total imaging time [29]. For materials with large Raman scattering cross-sections, the acquisition time can be as short as 1 msec. However, since most biological samples have very small Raman scattering cross-section which is proportional to the probability of an incident photon being Raman scattered with a particular Raman shift, the total acquisition time of a Raman image may be several hours. Thus, the throughput of the Raman microscope needs to be improved in order to perform larger area imaging and *in situ* monitoring of biological processes.

2.3.3 Line-scan Mapping

Line-scan Raman mapping is an extension of point-scan scheme. Instead of scanning a laser spot, a line-shaped laser beam is projected onto the sample and the Raman spectra from the line are simultaneously collected by a two-dimensional CCD. The spatial information is registered on the CCD on a line parallel to the laser line and the entrance slit of the spectrograph, while the spectral information is dispersed perpendicularly. A second spatial dimension is recorded by scanning the line perpendicularly to the line focus. By parallel collection of multiple spectra, line-scan

Raman mapping can achieve about 100 times larger throughput than point-scan mapping [30, 31]. Similar to point-scan, the spatial resolution of line-scan approach is dictated by the laser beam width and sampling interval [29], and can be somewhat worse along the laser line direction due to non-strict confocality.

2.3.4 Summary

The advantages of Raman imaging methodologies are discussed in several literatures [29, 32]. For point and line Raman mapping approaches, the required acquisition time depends critically on the laser power density and the number of spatial positions to be sequentially scanned. Line-scan method provides the fastest imaging speed at a reasonable spatial resolution. Further, the spatial resolution in the direction parallel to the laser line is nearly diffraction limited as wide-field imaging. In point-scan mapping, the throughput is relative low due to the sequential scanning especially for large sample areas with perimeter dimensions of hundreds of micrometers. On the other hand, high fidelity image quality and depth profiling render it preferable to point-scan approach. In contrast, the overall throughput for wide-field imaging depends primarily on the number of wavenumber positions recorded. Thus wide-field imaging is preferable for chemical heterogeneity study with priori knowledge of the chemicals. For imaging unknown chemicals, wide-field imaging may be time consuming due to increases in number of wavenumber positions. Therefore, the work in this thesis focuses on further improving the throughput of the line-scan mapping approach, and developing novel instrumentation that based on parallel collection method borrowed from line-scan mapping while taking the advantage of flexible sampling at region of interests instead of a line.

2.4 SERS Substrates

As mentioned in previously, SERS can enhance the Raman signal by 10^6 to 10^{14} times, depending on the SERS substrates and applied method. The design and fabrication of SERS substrates are essential for application. The enhancement ability of metal nanostructures is determined through the frequency-dependent dielectric function. Furthermore, the enhancement effect increases with the electric field gradient experienced by the adsorbed analytes. Thus, the metal nanostructures should be as sharp as possible to achieve larger enhancement, known as the antenna effect [33, 34]. Furthermore, the coupling effect between adjacent sharp structures can further increase the SERS enhancement [35-37], known as the lightning rod effect. These sites with highly localized electric field are known as SERS hot spots. Besides, several essential requirements for SERS active substrates are: (1) large EF which is capable to improve the sensitivity and detection of limit dramatically, (2) uniformity and reproducibility to obtain repeatable outcome, (3) chemical and biological compatibility with the analytes or cells, and (4) chemical and temporal stability [9, 38].

Numerous SERS substrates have been reported since first observation of SERS effect. Generally, SERS substrates can be categorized into roughen continuous metal surface, colloidal nanoparticles, and periodic SERS arrays.

2.4.1 Roughened Surface and Metallic Nanoislands

Electrochemically roughened electrodes [11], the first SERS substrates with EFs of 10^5-10^6 [12], have been used in potential-dependent SERS measurements. However, electrochemically roughened metal electrodes suffer from several intrinsic limitations. First, the EF is much lower than colloidal nanoparticles and periodic SERS arrays.

Second, the uniformity is poor due to the broad distribution of the surface geometry. Furthermore, the quality of the polished polycrystalline electrode surface influences the SERS activity significantly. Rough surfaces are attractive because their larger surface area may promote analyte adsorption. Metallic nanoislands as SERS substrates have been studied as early as in the 80s due to easy and cost-effective fabrication [39-42]. They are very attractive because of the simple fabrication. Recently, Klarite, a SERS substrate with gold nanoislands film on inverted pyramidal pits in silicon wafers, has become commercially available. The EF of Klarite is at least 1×10^6. Porous materials have attracted much attention for label-free sensing due to the large available surface area for molecular binding and their intrinsic capability of size-selective filtering [43, 44]. Since Raman signals are collected from a three dimension volume, typically $1\mu m^3$ by a tightly focused laser beam, large SERS-active surface area is preferable from the sampling efficiency aspect. Several groups have reported porous templates coated with metal films as SERS-active substrates. Nanoporous gold (NPG) is an emerging cost-effective porous material that can be fabricated in a straightforward approach with high reproducibility. NPG film SERS-active substrates prepared by dealloying Au:Ag alloy, as shown in Fig. 2.3, are capable to achieve an average EF of about 10^5-10^6 [45]. Patterning NPG films can further improve the SERS enhancement factor. Single molecule detection has been reported using thermal wrinkled NPG film. However, the winkled NPG film suffers from site-to-site EF variation, from 10^7 to 10^{11} [46, 47]. Few sites on the wrinkled NPG film have an EF of 10^{11}. Therefore, further exploration on patterning of NPG is of great interest.

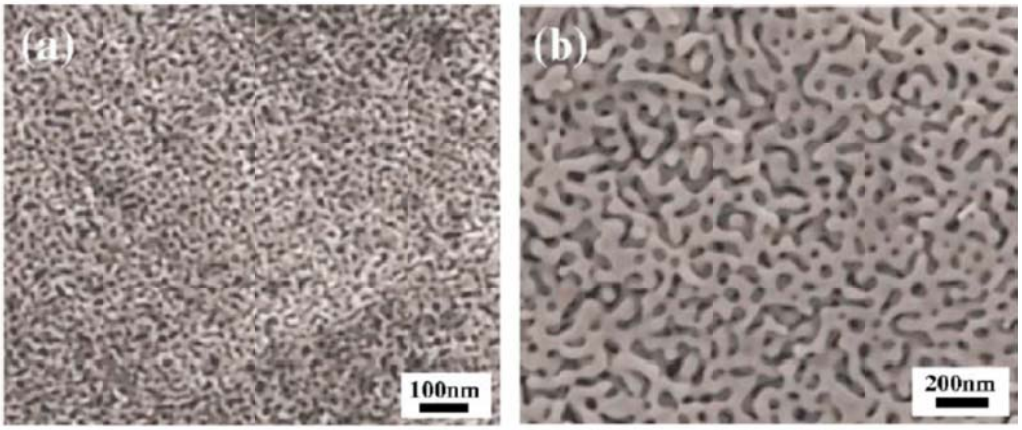

Figure 2.3 SEM micrographs of nanoporous gold with various nanopore sizes. (a) Nanoporous gold film after 5 min dealloying at room temperature; (b) dealloyed at room temperature for 48 h.

2.4.2 Colloidal Nanoparticles and Nanoshell

Colloidal nanoparticles have proven to be highly versatile and tunable materials for biophysical studies, imaging, medical diagnostics, and thermal therapy. Colloidal NPs are prepared by reducing the respective metal salts with various reduction agents using simple chemical laboratory equipment [33]. Nanoparticles in colloidal solution often experience a size and shape distribution, resulting in an undesired broadening of the resonance. Since the highest EFs are expected in the nanosized gap between two adjacent NPs, the controlled clustering of NPs is obtained by using different aggregation agents. Single molecule has been detected at junctions of silver colloidal NPs by several groups with EFs up to 10^{14} [48]. However, the pure aggregated colloidal NPs show specific Raman modes that can be assigned to citrated (reducing agent) or nitrate in some cases [49]. There are several derivatives of colloidal NPs such as star-shaped gold NPs and nanoshells. Metal nanoshells are a new type of nanoparticles. In contrast to pure silver or gold NPs, nanoshell consists of a dielectric core coated by a thin layer of metal film. As

shown in Fig. 2.4, the theoretical extinction spectra of gold nanoshells show tunable extinction peaks by controlling the core radius and thickness of gold film [50]. Due to the unique optical properties, gold nanoshells have a great potential in optical imaging, sensing and photothemeral therapy.

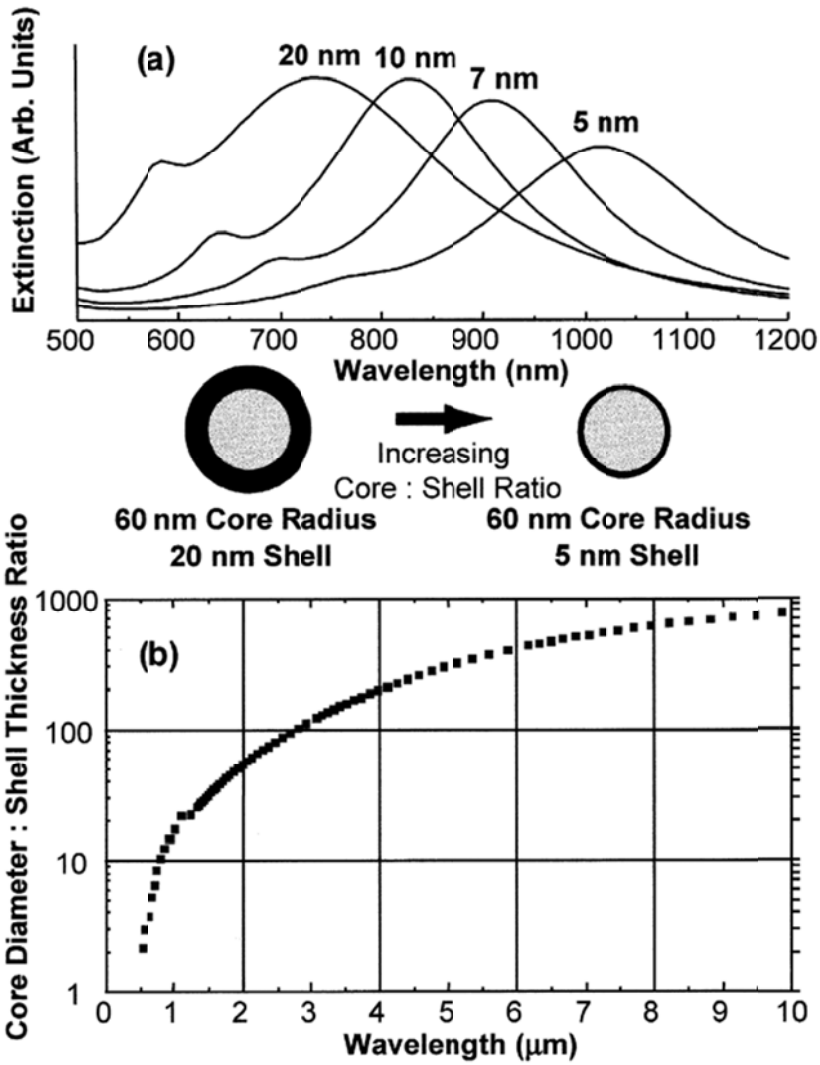

Figure 2.4 (a) Theoretically calculated optical resonances of metal nanoshells (silica core, gold shell) over a range of core radiusrshell thickness ratios; (b) calculation of optical resonance wavelength versus core radiusrshell thickness ratio for metal nanoshells.

2.4.3 Periodic and Reproducible SERS Arrays

SERS arrays are highly reproducible substrates. One approach to obtain SERS arrays is template-assisted fabrication. One of the most prominent templates consists of self-organized densely packed polystyrene or silicon dioxide (SiO_2) microspheres. The subsequent coating of these templates with silver or gold leads to metal film over nanosphere (MFON) substrates, as shown in Fig. 2.5 (a) [51, 52]. The template structure can be removed after metal coating, as this is common for some SERS array fabrication strategies such as nanosphere lithography (NSL). Since the microspheres are densely packed, the template serves as a mask and triangular shaped arrays are obtained after removal of the template. Figure 2.5 (b) shows an example atomic force microscopy (AFM) image of the triangular nanoparticle array [53]. The largest EF of NSL-fabricated nanoparticles is about 10^8. The electro-deposition of gold onto a microsphere template followed by dissolving of microspheres leads to sphere segment void (SSV) surfaces.

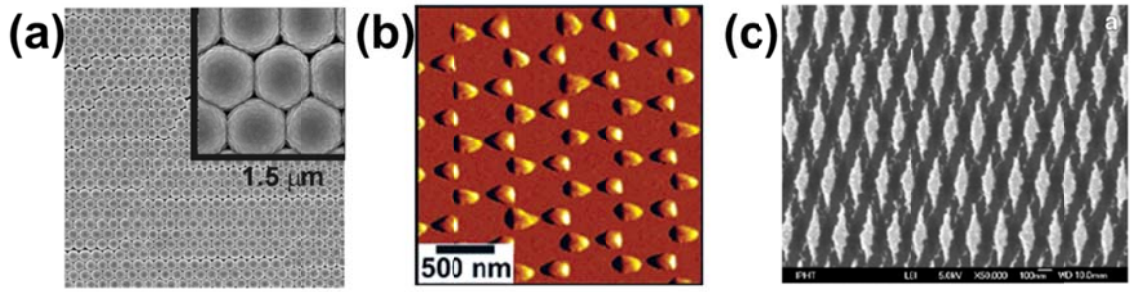

Figure 2.5 (a) SEM image of AgFON; (b) AFM image of triangular nanoparticle array by applying nanosphere lithography; (c) SEM image of gold diamonds by electron beam lithographic top-down fabrication.

Another approach to fabricate SERS arrays employs electron beam lithography (EBL). EBL is one the widely used top-down strategies for highly reproducible

fabrication of SERS substrates. Although high quality SERS arrays can be obtained, EBL approach is expensive and slow involving exposure and removal of resist. The scanning electron microscope image of a gold nanodiamond array presented in Fig. 2.5 (c) demonstrates the high degree of reproducibility of the EBL processes [54]. With different fabrication conditions, periodic micro- and nanostructures have been realized, such as rectangle structures, nanodisk and nanohole arrays, and metal nanorescents.

2.4.4 Summary

Beside the various SERS substrates mentioned above, there are many plasmonic substrates and sampling approaches are of great interest, for example, tip-enhanced Raman spectroscopy that employs metal coated AFM tip and affords single-molecule sensitivity and a lateral resolution down to 10 nm due to the size of the AFM tip. However, most plasmonic substrates cannot meet the requirements in the beginning of section 2.4. Roughened surface and metallic films show good uniformity and stability, but suffer from low SERS sensitivity. Colloidal nanoparticles provide ultrahigh enhancement while present poor uniformity and stability issue. SERS arrays provide decent enhancement, excellent uniformity, stability and reproducibility, leading to numerous applications in detection of biomolecules and biomarkers. However, most SERS arrays suffer from a small SERS-active area. Large SERS-active surface area is preferable to provide more analyte molecules to bind and consequently contribute to the total SERS intensity. In this thesis, the related work aims to apply nanosphere lithography on NPG, which provides a huge surface area compared to other substrates. Since the resultant structures are very uniform and reproducible from nanosphere lithography, plasmonics with desirable features is expected.

Chapter 3 Performance of Line-scan Raman Microscopy (LSRM) for High-throughput Chemical Imaging of Cell Population

3.1 Introduction

Raman scattering provides molecular "fingerprinting" capability due to the inelastic interaction between incident photon and molecular vibration. Using confocal Raman microscopy to study biological cells *in situ* is very attractive because molecular information can be obtained without exogenous stains or fluorescence labels [55]. Important examples include the studies of Matthaus *et al*. on the distribution of intracellular substances at different stages of cell mitosis [56]; the identification by Hartsuiker *et al.* and Haka *et al*. of representative constituents in breast cancer [57, 58]; time-lapse Raman imaging of a *single* lymphocyte by Pully *et al.* with 2 minute temporal resolution [59]; the identification of bacterial strains in biofilms by Beier *et al.* [60]; the study of intracellular delivery and degradation of polymeric nanoparticles by Chernenko *et al.* [61]; the compositional analysis of single microalgal cells [62] by Huang *et al.;* and, the mapping, by Weiss *et al*., of hydrocarbon deposits in *microalga Botryococcus braunii* [63]. The results from these studies show definitively that the mapping of spatiotemporal chemical composition by Raman spectroscopy can enable important discoveries in biology and biomedicine. However, the small spontaneous Raman scattering cross-section of biological samples, coupled with severe limits on laser power density (~2 $mW/\mu m^2$), leads to long pixel imaging times. In general, at least 100 ms of laser dwelling time is needed for a pixel volume of ~1 μm^3 (1 fL). This limits field size, resolution, and the molecular complexity that can be achieved in spatial chemical maps and the temporal

resolution of time-resolved studies. These limitations prevent the acquisition of chemical maps from cell population with optimal spatiotemporal resolution.

A high throughput instrument would enable Raman microscopy to become a viable detection and monitoring tool for analysis at cell population level, which could eventually lead to high throughput screening techniques. Recent advances in coherent anti-Stokes Raman scattering (CARS) and stimulated Raman scattering (SRS) techniques provide high-speed image acquisition at selected Raman bands, while plasmonics enables surface-enhanced Raman scattering when target molecules are adsorbed on Au or Ag nanostructures [64-66]. However, CARS is limited by non-resonant background and spectroscopic interpretation; SRS is not suitable for full-spectrum acquisition; SERS is a technique only sensitive to surface. In addition to techniques that fundamentally address the intrinsically small Raman scattering cross-section such as the coherent and SERS techniques mentioned above [64-66], an effective solution to the slow mapping speed is through approaches that exploit 2-dimensional detector technology to achieve parallel data acquisition. The approach has been used to improve throughput in slit-scan reflectance confocal microscopes [67] and line-scan fluorescence readers for DNA arrays [68]. In Raman spectroscopy domain, a fiber bundle has been employed as a shape-transforming component to relay a 2D scene onto the 1D slit of a spectrograph [69-73]. Free-space approaches have been implemented by Christensen *et al*. and Hamada *et al*. [6, 8]. Recently, we have implemented a parallel Raman microscopy scheme based on active-illumination by a spatial light modulator. An excellent study has been performed by Schlucker *et al.* to compare point-scan, line-scan and global illumination (GI) schemes [29], among which, the line-scan approach provides the highest throughput when full-

spectrum Raman images are acquired. Global illumination, in contrast, acquires narrow-band images within each frame and full-spectrum images are accomplished by scanning a bandpass filter. Strictly, speaking, GI is not a high-throughput technique because out-of-band Raman photons are not collected at each scanning step. GI might have an advantage when only a small number of Raman bands are needed.

In this chapter, we demonstrate that line-scan Raman microscopy (LSRM) can enable rapid classification and counting of hundreds of physically similar organic microparticles, as well as screening hundreds of bacterial spores within a manageable time frame. LSRM also enables the study of living colonial microalgal cells at the population and network levels and include the identification of intra and extracellular structural constituents, as well as cell metabolites such as protein, lipids, and hydrocarbons based on their distinct Raman fingerprints.

3.2 LSRM System Configuration and Characterization

To fully explore the throughput advantage of parallel acquisition, we have employed the 785 nm output of a continuous-wave (cw) titanium:sapphire laser (Spectra-Physics 3900S) pumped by a diode-pumped solid state 532 nm laser (Spectra-Physics Millennia 10X). As shown in Fig. 3.1 (a), the laser output is transformed by a line-generating optical system consisting of a Powell lens (L1, fan angle 7˚, Leading-Tech) and two cylindrical lenses (L2, 100 mm f.l. & L3, 50 mm f.l., Thorlabs) to form a uniform line. This line is relayed to the side-port focal plane of an inverted microscope (Olympus IX70). A dichroic mirror (785 nm RazorEdge dichroic, Semrock) is placed on the beam path to reflect the laser light. A galvanometric mirror (Thorlabs) is employed to scan and de-scan the line in the transverse direction. Epi-Raman is collected by a

microscope objective (60X or 10X) and sent through the dichroic mirror and an additional long-wave pass filter (785 nm RazorEdge long pass, Semrock) for laser intensity reduction, and imaged at the entrance slit of a spectrograph with a CCD detector (Princeton LS785).

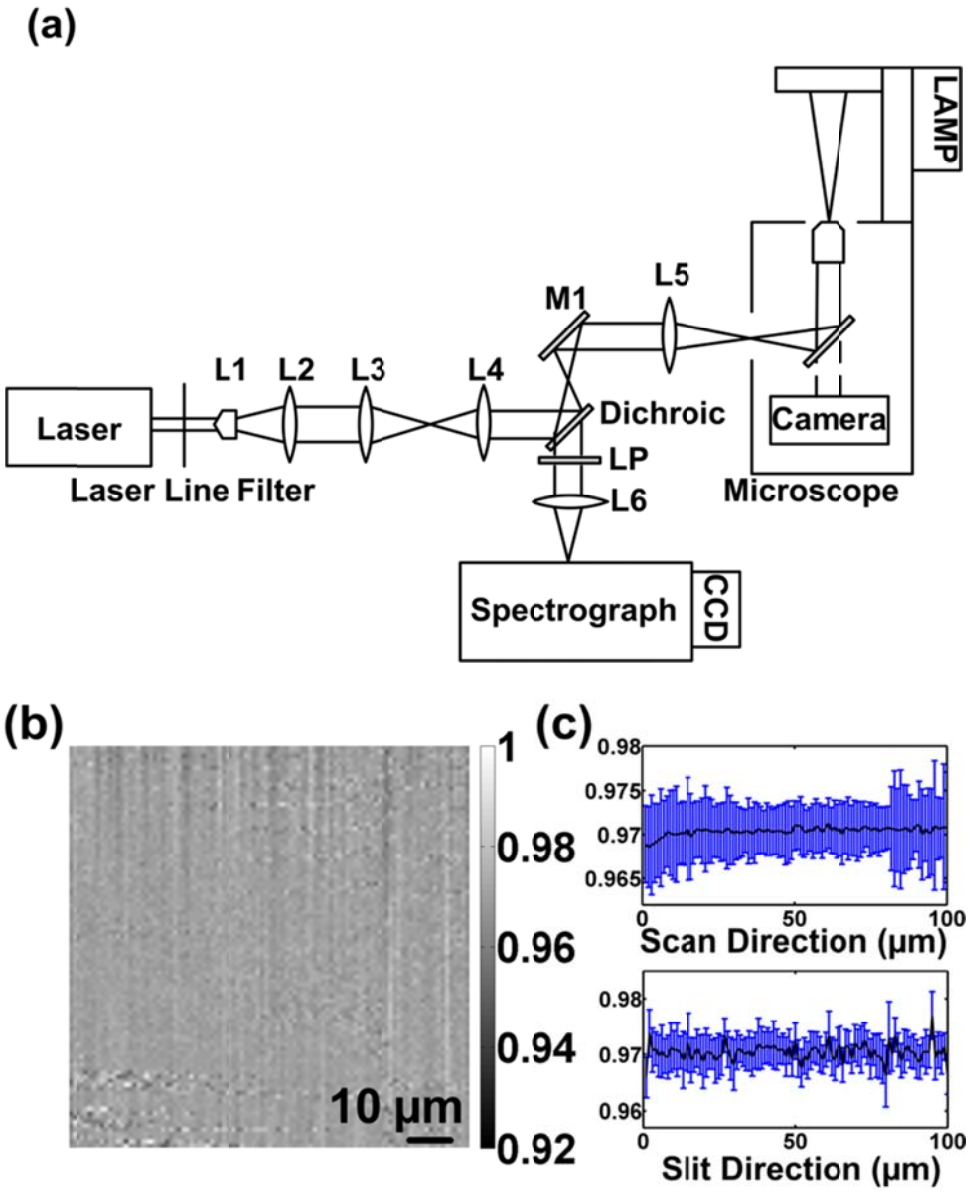

Figure 3.1 LSRM system configuration and intensity uniformity: (a) configuration; (b) map of polystyrene plate; (c) representative intensity profiles along the projected line and scanning directions.

An essential requirement for high performance LSRM is intensity uniformity of the excitation laser light along the projected line as well as across the scanning direction. We have evaluated the uniformity in both directions using a polystyrene plate. Figure 3.1 (b) shows an x-y map (area 100 μm × 100 μm) of the strongest Raman peak, which originates from polystyrene ring breathing mode at 1001 cm^{-1}. The standard deviation of the intensity values is less than 0.4% of the average intensity. To better evaluate the intensity uniformity, Figure 3.1 (c) displays intensity profiles along the scanning and the line directions. This confirms that the laser power has been evenly distributed along the projected line. The entire laser line was ~ 120 μm in length, from which the top and bottom 10 μm were not used. Thus the utilization percentage was ~85%. This map could also be used for intensity correction across the field of view. The imaging capability of the microscope has been characterized using polystyrene (PS) beads of size from 3 μm to 500 nm. Figures 3.2 (a) and 3.2 (b) show the maps of 3 μm and 1 μm PS microparticles generated using the PS peak at 1001 cm^{-1}, respectively. Figure 3.2 (c) shows the Raman map and intensity response in X and Y direction of a single 500 nm PS bead. The lateral resolution is estimated to be 600 nm and 800 nm in X and Y direction from the full width half maximum (FWHM) of the intensity response, respectively. The spectral resolution is better than 5 cm^{-1} according to manufacturer's specifications. The total acquisition time is 2.5 minutes for an area of 100 × 100 μm^2 using a 0.5 μm scanning step size and a 0.75 sec dwell time of the projected laser line. In comparison, it would take ~ 4 hours to acquire such a map with similar resolution, step size, and power density using a point-scan system. Assuming that 100% of the area in Fig. 3.2 (b) is packed by 1 μm PS beads, the equivalent imaging throughput is ~100 microparticles/sec with 0.5 s laser dwell time

and 0.5 μm step size. The power density has been set at ~3 mW/μm^2 for sample damage threshold considerations. Typically, the x-direction resolution is comparable for point-scan and line-scan systems as experimentally observed by Schulucker *et al*. in their comparison of point-scan, line-scan and global illumination systems. For line-scan system, the y-direction resolution is slightly worse than that for the x-direction, likely due to the lack of confocality along the spectrograph entrance slit, which has been observed by us and Schulucker *et al*.

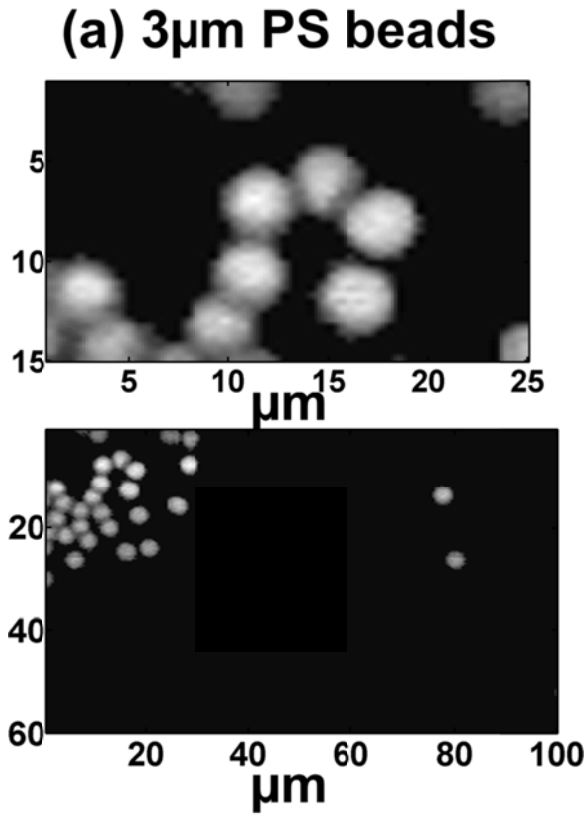

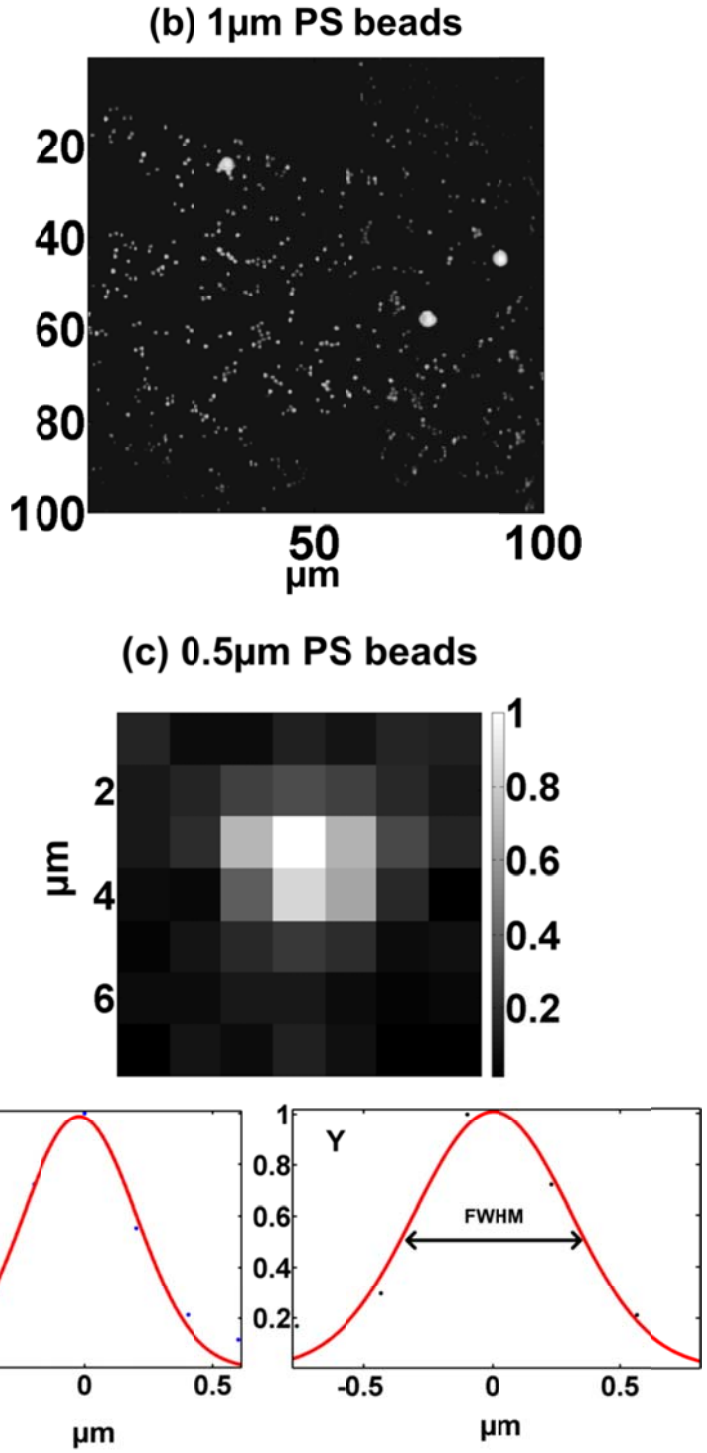

Figure 3.2 LSRM system characterization: (a) 3 µm PS beads within a 60 x 100 μm^2 area (lower), zoom-in of the upper left corner (upper); (b) image of 1 µm PS beads mixed with 3 µm PS beads; (c) 500 nm PS bead for estimating the lateral spatial resolution.

3.3 Rapid Counting and Identification of Microparticles

One of the most powerful features of chemical imaging is the ability to classify microparticles of similar size, shape and refractive index. Although Raman spectroscopy has been a great tool in analytical laboratories for material characterization, its slow imaging speed has prevented the possibility in counting many microparticles rapidly. To evaluate the capability of LSRM, we have prepared samples of mixed 3 μm polystyrene (PS) and polymethylmethacrylate (PMMA) microspheres. Figure 3.3 (a) shows the image acquired using a brightfield imaging channel, from which little difference can be observed among these microspheres. LSRM has been performed over a partially overlapping but larger area of the same sample. Images were generated using the PMMA peak at 813 cm^{-1} (Fig. 3.3 (b)) and PS peak at 1001 cm^{-1} (Fig. 3.3 (c)) with the corresponding Raman spectra of these two materials shown in Fig. 3.3 (d). These maps provide unambiguous classification of microspheres of different chemical compositions. Particle counting can be subsequently implemented using thresholding and edge finding algorithms. The Raman data cube has been collected within 100 seconds.

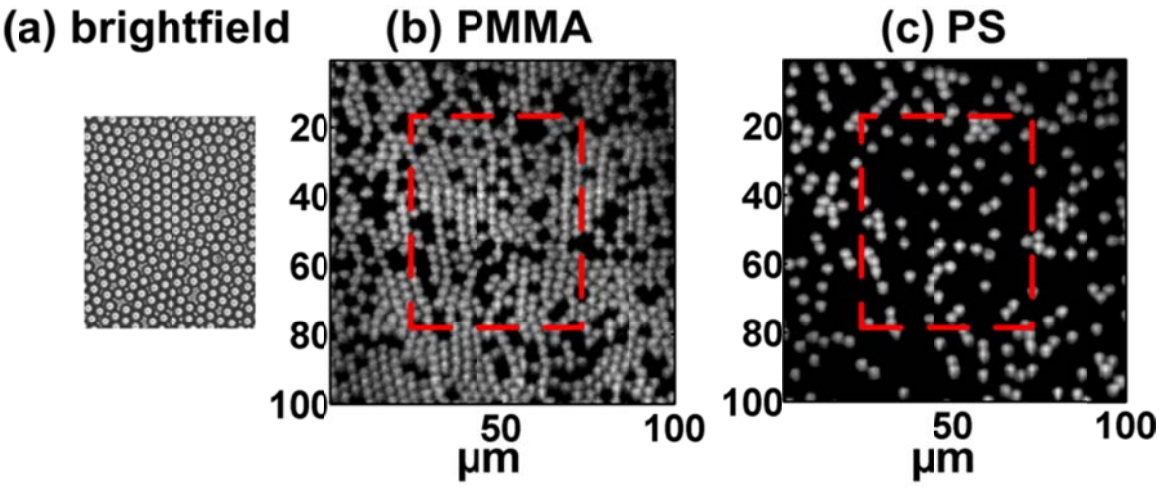

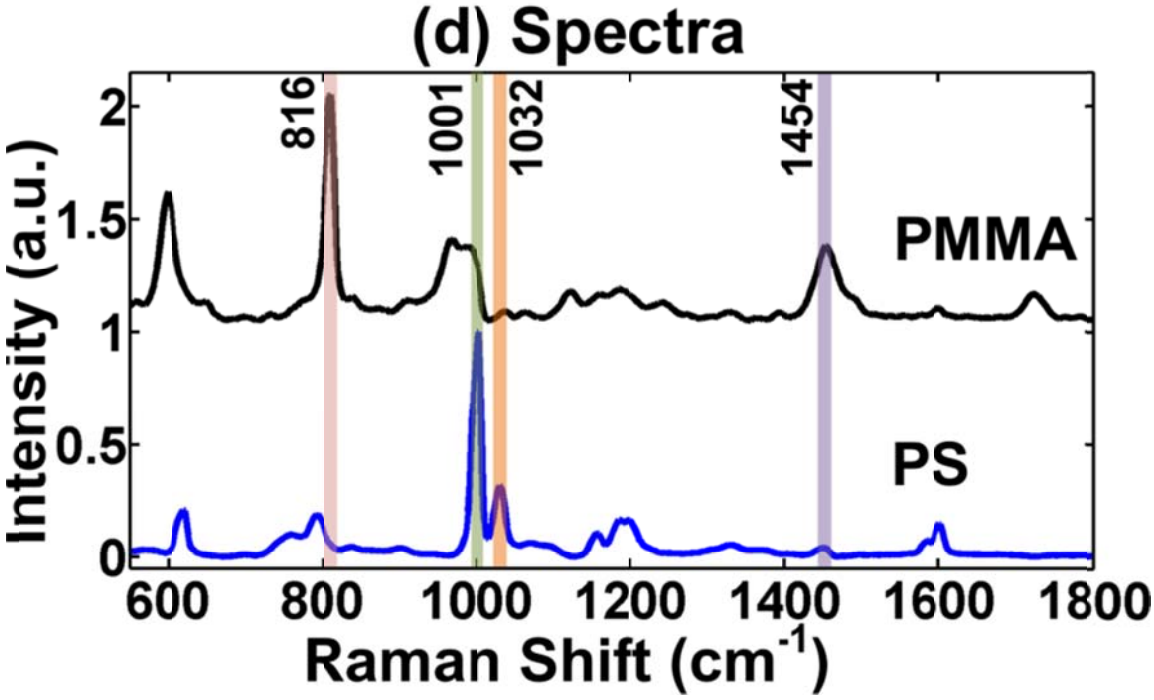

Figure 3.3 Rapid identification and counting of microparticles using LSRM: (a) brightfield image of mixed PS and PMMA microspheres; map generated using PMMA (b) and PS (c) Raman peak, respectively; (d) Raman spectra of PMMA and PS.

3.4 Rapid Counting and Identification of Bacterial Spores

A natural application for counting and classification of microparticles is bacterial cell analysis [74, 75]. Some bacteria are known to "sporulate" to survive harsh environmental conditions. Therefore, the study of spores is of great interest in microbiology. In addition, it is critical to detect and analyze spores in biofilms in order to develop optimal treatment strategies in biomedicine. Using Bacillus subtilis spore as a model, the brightfield image is shown in Fig. 3.4 (a) over an area of 60 x 30 μm^2. A corresponding Raman map acquired by LSRM using the calcium dipicolinate (CaDPA) Raman band at 1011 cm^{-1} is shown in Fig. 3.4 (b). Figure 3.4 (c) shows the full Raman

spectra from all the spores with the solid line denoting the mean spectrum and the shaded area 1 standard deviation. Strong Raman bands at 656 cm^{-1}, 826 cm^{-1}, 1011 cm^{-1}, 1395 cm^{-1}, 1445 cm^{-1} and 1576 cm^{-1} are assigned to CaDPA and are in good agreement with previous studies. Bands at 1655 cm^{-1} is assigned to protein amide I. The Raman image consisting of 151 spores was acquired within one hour, or 2.5 spores/min, which is already faster than one of the fastest results at 2 spores/min. LSRM throughput can be much higher with a sample with higher spore coverage. For example, an order of magnitude higher throughput can be easily achieved if the spatial coverage of bacteria is increased from the current value of 8% to 80%.

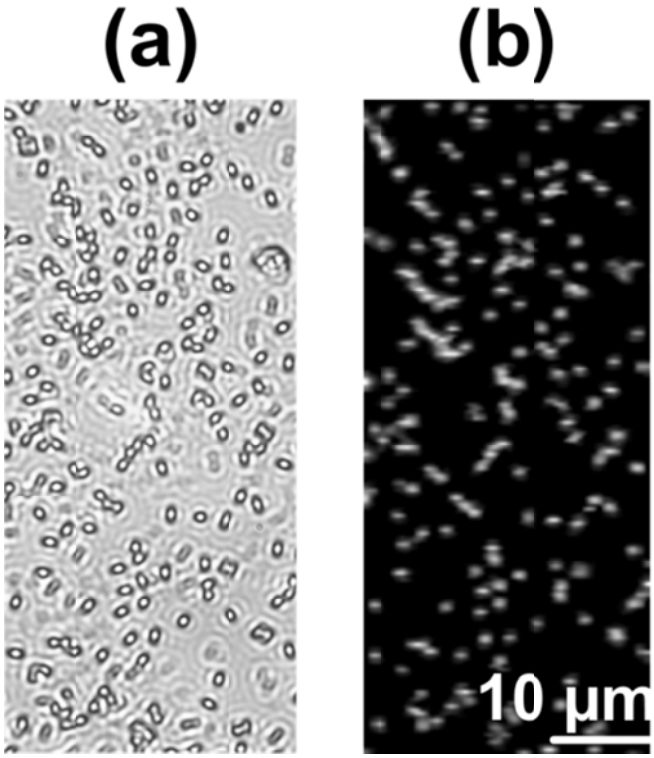

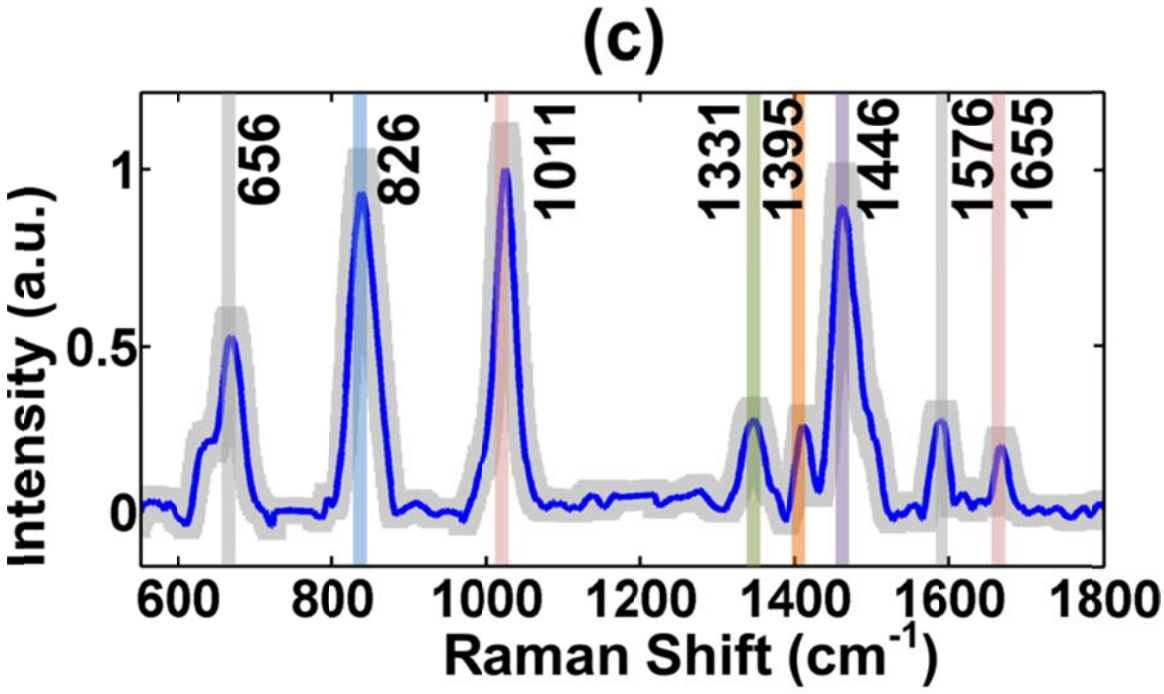

Figure 3.4 Rapid identification and counting of bacterial spores using LSRM: (a) brightfield image of more than 100 spores; (b) map generated using CaDPA Raman peak; (c) mean and standard deviation of Raman spectra of *Bacillus subtilis* spores.

3.5 Chemical Imaging of Colonial Microalgal Cell Using LSRM

Using Raman microscopy to study metabolites, lipids and hydrocarbons in intact microalgae bioreactors has recently attracted significant interest due to the importance of understanding spatiotemporal molecular composition and the associated biosynthesis pathways for nutrition product and biofuels [62]. For example, hydrocarbon botryococcenes are hypothesized to experience multi-step methylation as they migrate from the intracellular space to the extracellular environment [63]. However, such hypothetical pathway is still not well understood because of a lack of label-free molecular imaging technique. Existing mapping approaches are severely limited by slow mapping

speed, low signal-to-noise ratio, and interference by strong background fluorescence [62, 63], resulting in unsuccessful Raman mapping results. We have applied LSRM to study the chemical distribution in a colonial microalgae, *Botryococcus braunii*, B race for the analysis of intra- and extra-cellular lipids and hydrocarbons. This green microalga produce triterpenes known as botryococcenes that can be converted into high octane gasoline, kerosene and diesel fuels. Botryococcenes have unique Raman bands near 1647 cm^{-1} to 1667 cm^{-1}, while common lipids such as saturated and un-saturated triglycerides, and hydrocarbons have Raman band at 1440 cm^{-1}. The chlorophyll map (Fig. 3.5 (b)) generated from Raman band at 745 cm^{-1} and carotenoids map (Fig. 3.5 (c)) generated from Raman band at 1520 cm^{-1} clearly showed the cell morphology. Representative cell boundaries were highlighted using dotted lines. Total lipids shown in Fig. 3.5 (d) were found both inside the cell and in the extra-cellular matrix. Botryococcenes presented in Fig. 3.5 (e) were primarily found in the extra-cellular matrix, which suggests a more advanced methylation stage of triterpene. The relative amounts of individual can be assessed semi-quantitatively using the colorbar. The entire Raman data cube has been collected within 60 minutes without a pre-photobleaching step.

(a) Bright Field Image

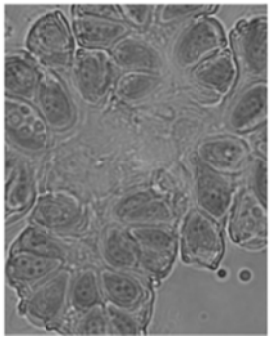

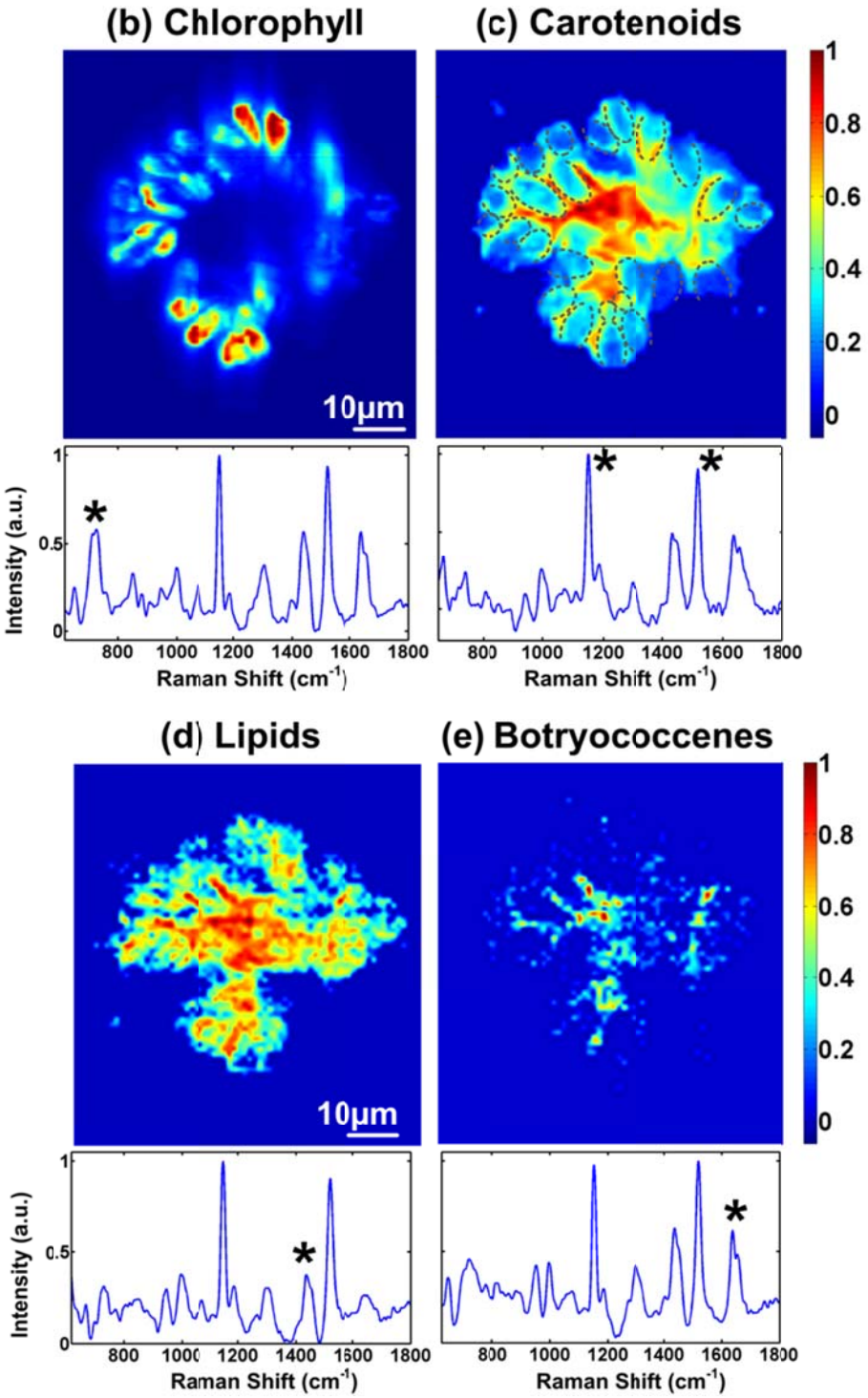

Figure 3.5 Chemical imaging of colonial microalgae using LSRM: (a) brightfield image; Raman maps generated for (b) chlorophyll, (c) carotenoids, (d) lipids and (e) botryococcenes with representative Raman spectrum under each map.

3.6 Analysis of ethyl and methyl centralite vibrational spectra for mapping organic gunshot residues

Detection of gunshot residues (GSR) is important in forensic science due to its potential use in criminal justice to provide evidence of whether a suspect discharged a firearm [76-78]. Methyl centralite (MC) and ethyl centralite (EC) are good indicators among various compounds in GSR to demonstrate the presence of GSR because they are highly specific to smokeless powders with very few significant environmental sources; whereas, the stabilizer diphenylamine, in addition to ammunitions, has known industrial and agricultural uses. Thus, centralites could become an alternative identifier that is presumably exclusive enough to smokeless powders so as to prevent false outcomes [79].

EC and MC were first simulated by DFT methods to investigate the molecular structures, as well as the vibrational spectra. The details of Density functional theory (DFT) calculations are presented in Appendix I. The IR spectra were obtained using a Perkin-Elmer Spectrum One spectrometer with an attenuated total reflectance (ATR) accessory. The Raman spectra of centralite powders were recorded by LSRM.

3.6.1 Vibrational Spectra

Theoretical Raman and IR frequencies of EC and MC, as well as their intensities, were calculated from the B3LYP [80, 81] using the extended 6-311++g(df,pd) basis set. Experimental Raman and IR spectra of powers were obtained to better identify the frequencies. The frequencies of the CH vibrations above 2500 cm^{-1} was scaled by a factor of 0.960 derived from the reported scaling factor for the valence A-H stretching force constants, while the harmonic frequencies below 2000 cm^{-1} were scaled by a factor of 0.982 [82]. For comparisons, Figure 3.6 and 3.7 show theoretical/experimental Raman

and IR spectra of EC, respectively. Moreover, the spectral characteristics of MC are shown in Fig. 3.8 and 3.9. Good agreement has been observed from both theoretical frequencies and experimental observed results.

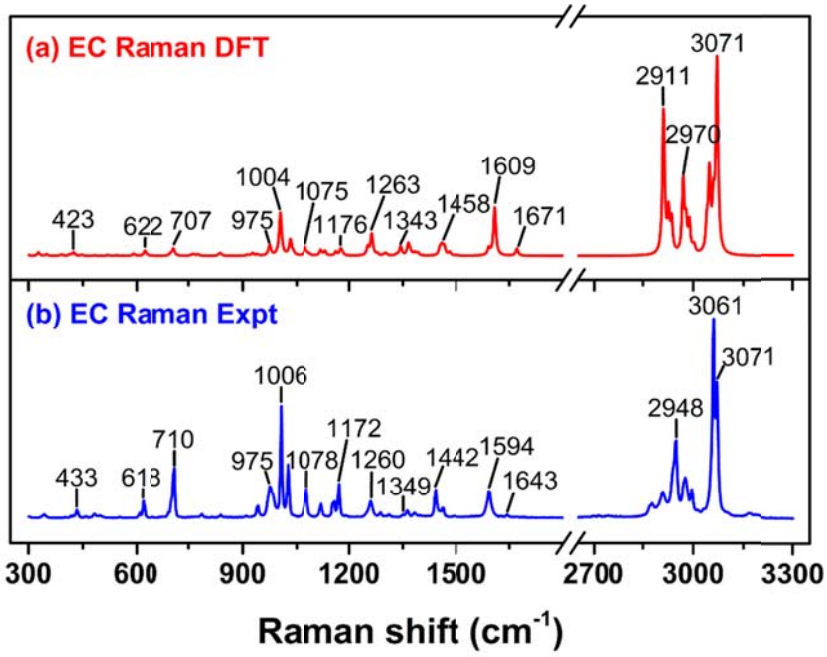

Figure 3.6 Raman spectra of ethyl centralite (1,3-diethyl-1,3-diphenylurea): (a) theoretical calculation based on DFT and (b) Raman spectrum obtained using 785 nm laser excitation.

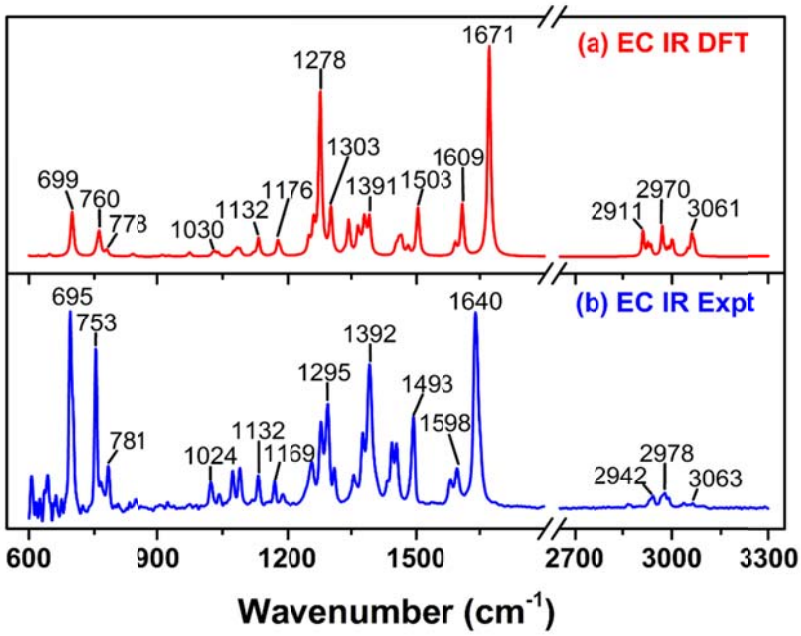

Figure 3.7 IR spectra of ethyl centralite (1,3-diethyl-1,3-diphenylurea): (a) theoretical calculation based on DFT and (b) IR spectrum obtained using ATR-IR.

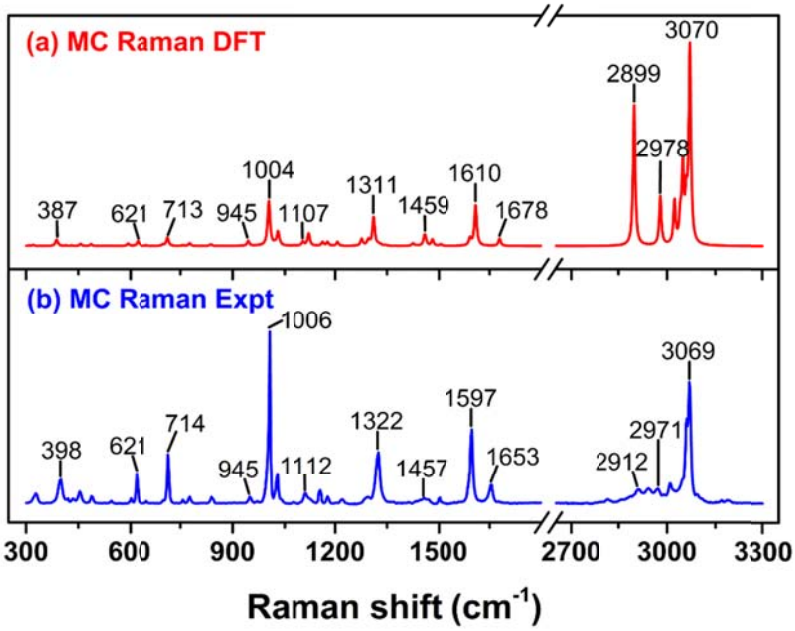

Figure 3.8 Raman spectra of methyl centralite (N, N'-Dimethyl-N,N'-diphenylurea): (a) theoretical calculation based on DFT and (b) Raman spectrum obtained using 785 nm laser excitation.

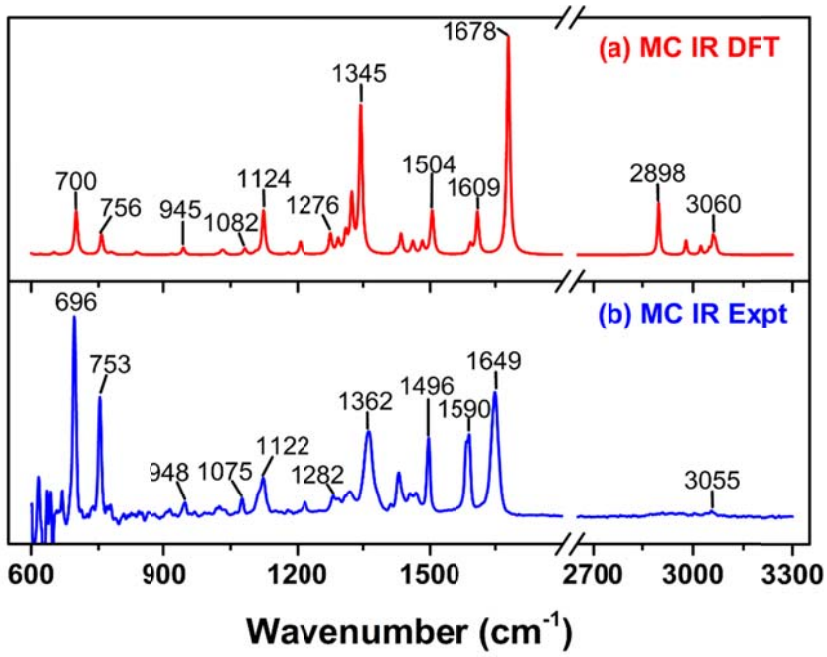

Figure 3.9 IR spectra of methyl centralite (N, N'-Dimethyl-N,N'-diphenylurea): (a) theoretical calculation based on DFT and (b) IR spectrum obtained using ATR-IR.

3.6.2 Raman Imaging of Centralites

Recently, Lednev and coworkers successfully detected macro and microscopic the inorganic and organic gunshot residue particles collected via "tape lifting" by using FTIR-ATR imaging [83], which demonstrates great potential in analyzing organic GSR through molecular fingerprinting. Compared to IR imaging, Raman imaging offers better spatial resolution, superb multiplexing capability and a low background [84]. Unfortunately, Raman imaging in detecting the gunshot residues is little explored. Herein, we applied Raman imaging to detect centralites particles on coverslips. The integration time is 10 sec for each scan step. Figure 3.10 (a) and 3.10 (b) show the bright-field image of the mapped area (left) and the corresponding Raman maps (right) for EC and MC, respectively. Both Raman maps were generated by the strong peak intensity at 1006 cm^{-1}

that is assigned to the ring breathing for EC and MC. The detected particle sizes are estimated to be from 2 to 13 μm. Overall, the Raman maps of EC and MC match the bright-field optical images well. Therefore, LSRM can be a rapid analytical instrument for analyzing centralites.

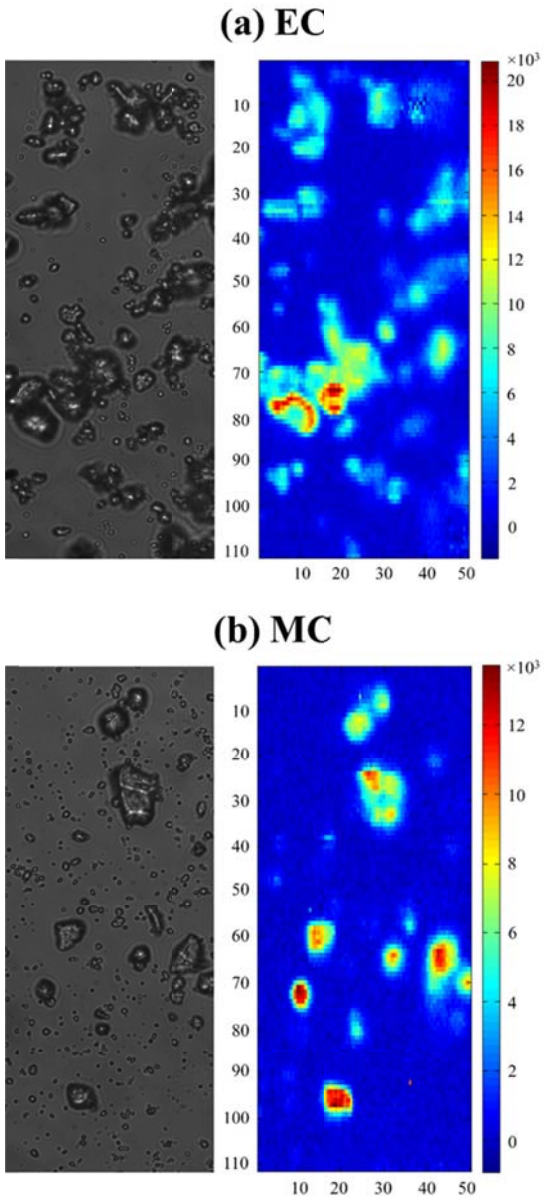

Figure 3.10 Raman imaging for detection of centralites: (a) and (b) are the visual image of the mapped area (left) and its corresponding Raman maps (right) for EC and MC powder particles on coverslips, respectively.

3.7 Conclusion

In conclusion, we have evaluated the performance of a high throughput line-scan Raman microscope for chemical microscopy of cell population. We have presented detailed system configuration and performed careful characterization for image uniformity and resolution. The overall image acquisition time is significantly reduced by ~100 times compared to conventional Raman imaging methods but provides comparable spatial and spectral resolution. We have demonstrated the rapid imaging capability of this instrument in test involving a) the identification and counting of organic microparticles that appear identical in brightfield image but differ in their chemical signature; (b) chemical imaging of bacterial spores, c) chemical mapping of colonial microalgal cells. These results suggest that LSRM can be a highly versatile tool for studying cells at the population level without the need for labeling. Moreover, ethyl and methyl centralites are characterized using LSRM. The simulated vibrational spectra are in a good agreement with the experimental results. The mapping of EC and MC represents the first attempt to produce rapid and effective analysis.

Related publication

This chapter has been published as:

"Performance of line-scan Raman microscopy (LSRM) for high-throughput chemical imaging of cell population", J. Qi and W. -C. Shih, *Appl. Opt.*, 2014, **53**, 2881-2885.

"Analysis of ethyl and methyl centralite vibrational spectra for mapping organic gunshot residues", J. Zeng, J. Qi, F. Bai, J. C.-C. Yu and W.-C. Shih, *Analyst*, 2014, doi**:** 10.1039/C4AN00657G

Chapter 4 Parallel Raman Microspectroscopy Using Programmable Multipoint Illumination

4.1 Introduction

Raman spectroscopy can provide molecular information via inelastic light scattering without physical contact. Coupled with microscopic imaging, Raman microspectroscopy is a powerful technique for material analysis, for example, stress and temperature measurement in silicon and compositional analysis of polymer microparticles [29]. Three methodologies are commonly employed in contemporary Raman microspectroscopy, namely, points-can, line-scan and global illumination [29].

As described in Chapter 2, the point-scan operation involves the collection of Raman spectra in a point-by-point fashion. Since Raman scattering is a relatively weak phenomenon, the laser spot dwelling time at each point is typically on the order of milliseconds to seconds. In addition, the data needs to be read-out after each point acquisition, which typically adds another few hundred milliseconds for a standard charge-coupled device (CCD) detector. As a result, conventional point-scan Raman mapping is a time-consuming process and can take as long as a few hours to map a $50 \times 50\ \mu m^2$ region.

To improve efficiency, parallel acquisition has been implemented based on time-sharing or power-sharing schemes. In the former, the laser is rapidly scanned over multiple points of interest during the time of a single CCD recording frame [85, 86]. In the latter, the laser is shaped into an elongated line and the entire line is imaged by a single CCD frame [6, 29, 87]. Thus, both schemes can substantially reduce multiple read-out times. A key difference, however, lies in the temporal power fluctuation within a CCD frame: For time-sharing, the total laser power is focused on one spot at any given

time but for power-sharing the laser power is distributed on all spots. Therefore, the frame-averaged power is identical to the instantaneous power for power-sharing but not for time-sharing. Another significant difference is there is no scanning within each frame for power-sharing. Recently, the time-sharing approach has been demonstrated to provide flexibility for imaging multiple points not aligned on a line, which is particularly advantageous for sparse samples such as bacteria or environmental particles [85].

In this chapter, we present a novel power-sharing approach that allows the simultaneous imaging of multiple points not aligned on a line. This is achieved by combining programmable multi-point laser illumination with wide-field Raman imaging. Our scheme can significantly improve the sampling flexibility compared to the line shaped illumination approach while maintaining the parallel acquisition efficiency, 100% laser power duty cycle on all spots, and the non-scanning nature within a single CCD frame. Although imaging multiple spots simultaneously using a spatial light modulator (SLM) has been developed for multi-photon fluorescence microscopy [88], it has not been implemented in Raman microspectroscopy.

4.2 System Configuration and Characterization

The system configuration is shown in Fig. 4.1 (a). The 785 nm output of a CW Titanium:Sapphire laser (Spectra-Physics 3900 S) is filtered by a laser-line filter (Semrock LL01-785-12.5) and expanded to ~1 cm in diameter before the spatial light modulator (SLM) liquid crystal on silicon (LCOS) Hamamatsu. The output from the SLM is fed through the back port of an inverted microscope (Olympus IX71) with an addition of a tube lens.Adichroic mirror (Semrock LPD01-785RU-25) is placed in the microscope turret for epi-Raman acquisition via a microscope objective (Olympus

UPLSAPO 60XW, 1.2 NA). The Raman light is redirected out via the microscope side port, filtered by a long-wave pass filter (Semrock LP02-785RS-25), and sent into a spectrograph (Acton SpectroPro 300i) with a thermal-electrically cooled CCD camera (Princeton 400BRexcelon). We use the code developed by Grier's group to program the SLM to generate illumination patterns [89]. The CCD data acquisition and the SLM pattern generation are synchronized by Labview (National Instruments). The spectral resolution of our system is ~8 cm^{-1} by comparing spectra taken by this system and a calibrated confocal Raman system, respectively. As shown in Fig. 4.1 (b), the Raman spectra of polystyrene (PS) and polymethylmethacrylate (PMMA) are measured by both systems and no appreciable differences are noticed. The spatial (x-y-z) resolution is ~0.9, 0.9 and 4.5 μm, respectively at 785 nm excitation using 0.5 μm PS beads fixed on a glass coverslip [Figs. 4.1 (c) – 4.1 (e)].

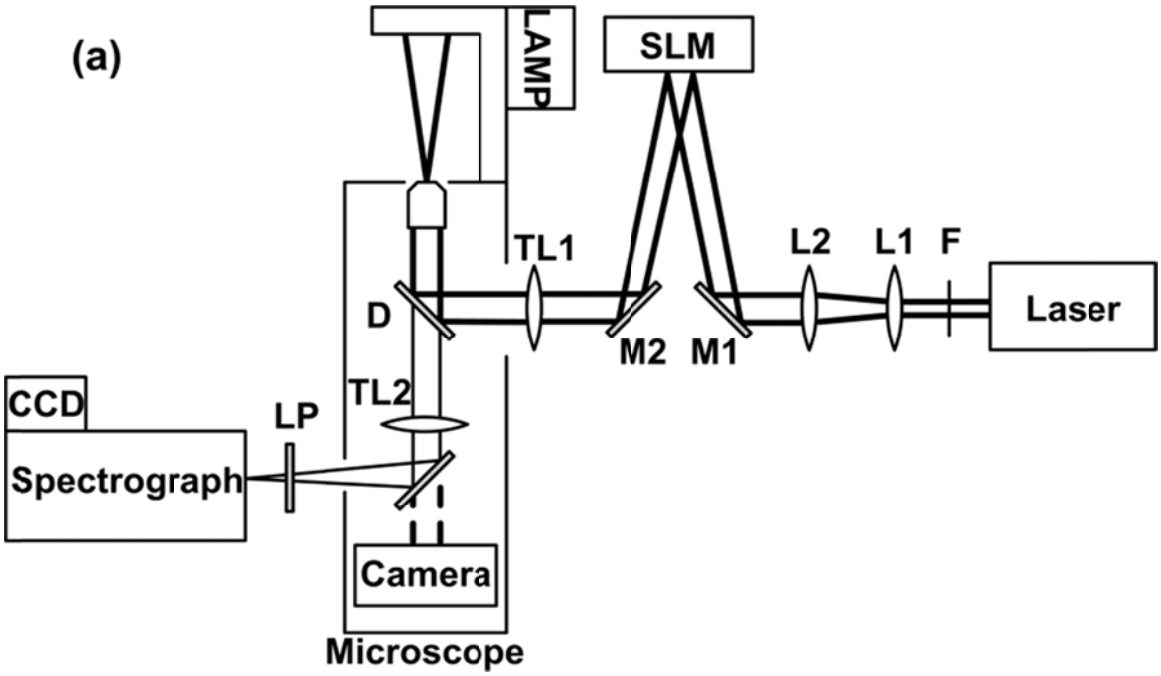

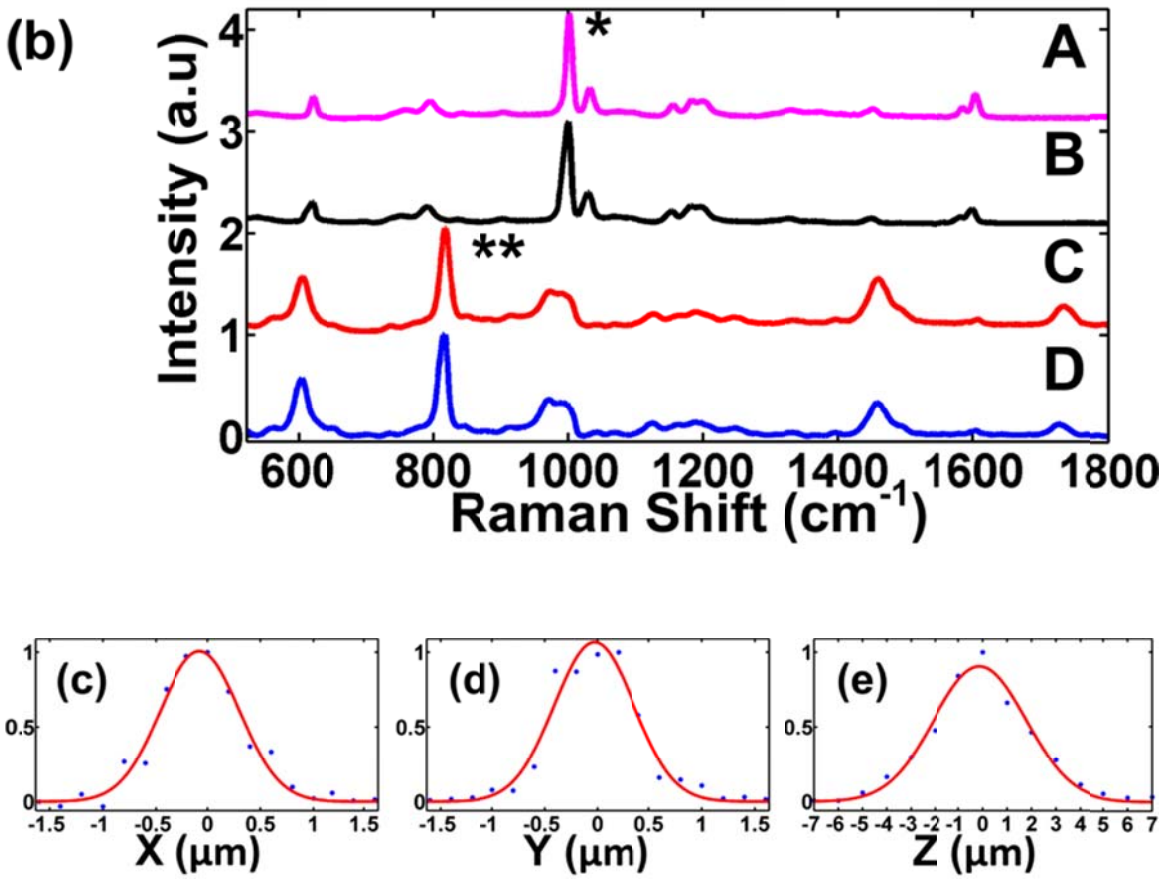

Figure 4.1 (a) System configuration; (b) Raman spectra of PS (A) and PMMA (C) measured using the proposed system vs PS (B) and PMMA (D) measured by a confocal Raman system; spatial resolution in (c) x, (d) y and (e) z direction.

4.3 Programmable Illumination Patterns on Silicon

We first demonstrate the performance of our scheme using a uniform silicon sample. The patterns shown in Fig. 4.2 (a) – 4.2 (c) are the raw images cropped from the 520 cm^{-1} silicon Raman peak region after polynomial-based background removal. Since there are no other Raman features near this peak, these Raman images appear to be identical to the illumination pattern with slight additional spread in the x direction due to dispersion. A design constraint on the illumination pattern is that no two points are

allowed to completely overlap along the direction perpendicular to the grating dispersion direction, preventing data mixing from adjacent points.

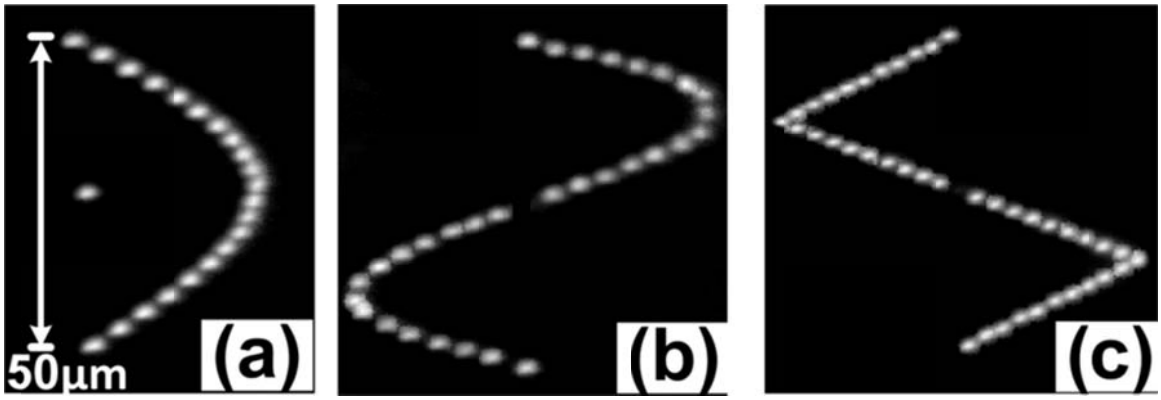

Figure 4.2 20-, 30- and 40-point illumination patterns: (a) half-sine; (b) full-sine; and (c) triangular patterns using the Raman peak of Si @ 520 cm^{-1}.

4.4 Identification of Polymer Microparticles

Next, we analyze a mixed population of a total of 138 PS and PMMA microparticles (each 3 μm in diameter, Sigma — Aldrich). A snapshot visual image in Fig. 4.3 (a) shows little difference between them even though the index of these two materials are quite different (PS 1.55 – 1.59; PMMA ~ 1.49). Using a centroid finding algorithm over the snapshot image, we first identify the centers of individual microparticles. Then the centroids are grouped into 11 sub-groups, resulting in 11 patterns as the SLM input. For example, pattern no. 5 is shown in Fig. 4.3 (b) with the laser spots overlaid with 17 microparticles. After collecting the Raman spectra from all microparticles, chemical identification can be made by using the characteristic Raman features of PS and PMMA, e.g., the peaks marked out in Fig. 4.1 (b) with results shown in Fig. 4.3 (c) where PS beads are marked red. We note that due to the relatively large size of the particles compared to the laser spot size, more patterns are needed to satisfy

the no overlapping constraint mentioned earlier. With smaller particles, our current field of view (~ 60 × 60 μm^2) would allow ~30 points per pattern without overlapping.

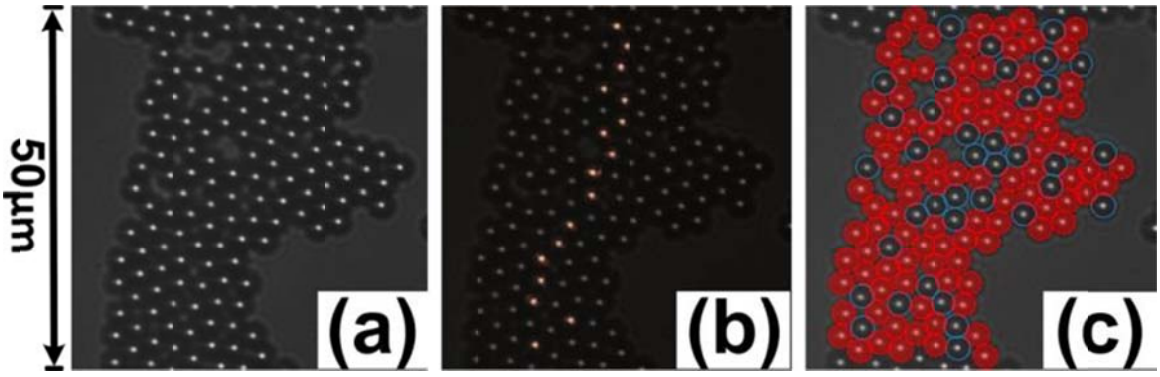

Figure 4.3 Visual image of mixed population of PS and PMMA; (b) laser spots from pattern no. 5 overlaid with the visual image; (c) identification of PS and PMMA microparticles.

The previous example demonstrates a scenario when the microparticles are densely packed. We then prepare a different sample with sparse particle distribution (28 PS particles) as shown in Fig. 4.4 (a). Following a similar scheme, complete chemical identification can be achieved using three patterns. Figure 4.4 (b) shows the grouping scheme for the three illumination patterns. Figure 4.4 (c) shows the corresponding Raman image using the PS Raman peak at 1001 cm^{-1} by overlaying all three frames. We note that the first illumination pattern has 17 points and each one is significantly dimmer than those in the second (6 points) and the third (5 points) patterns. This is due to the laser power distribution among more points. Next we assess the intensity uniformity within each pattern by measuring the silicon Raman peak (@520 cm^{-1}) intensity using a uniform silicon sample.

Together with measuring the laser power, we can assess the image intensity uniformity across patterns with different number of points. Figure 4.5 (a) shows the

average power and standard deviation per point versus the number of points in the 11 SLM patterns employed in Fig. 4.3 with the same total laser power (100 mW before the SLM; ~30 mW at the sample). A gradual decrease in power per point is observed when more points are included in the illumination pattern.

The silicon data in Fig. 4.5 (a) can be employed for intensity calibration within an illumination pattern as well as across different patterns with variable number of points. For example, Fig. 4.5 (b) shows an intensity-corrected PS image corresponding to the raw image shown in Fig. 4.4 (c), indicating remarkable improvement.

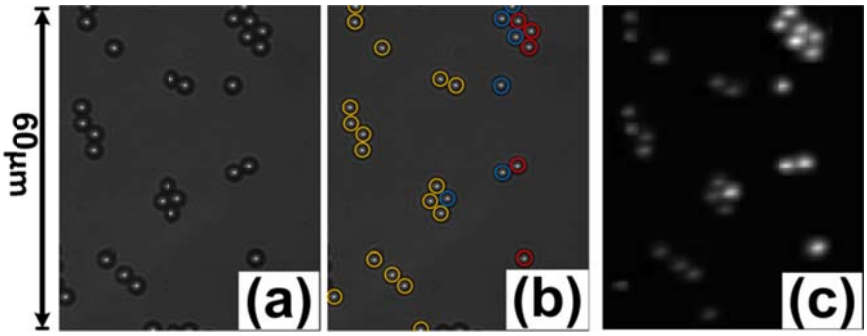

Figure 4.4 (a) Visual image of 28 PS microparticles; (b) grouping scheme for the 3 projected patterns (17-6-5) overlaid with the visual image; (c) resulting overlaid Raman image from three illumination patterns.

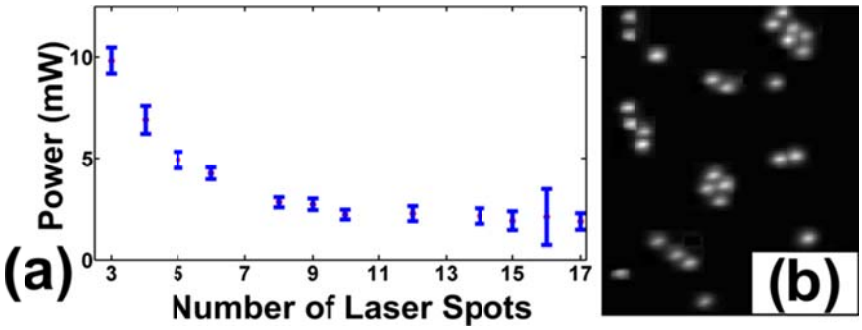

Figure 4.5 (a) Average intensity and standard deviation versus the number of laser spots in the 11 SLM patterns employed in Fig. 4.3; (b) intensity corrected Raman image corresponding to the raw image in Fig. 4.4 (c).

4.5 Multiple Optical Trapping

Since tightly focused laser spots can readily form optical traps, the proposed scheme can trap multiple polystyrene beads in a non-straight line as shown in Fig. 4.6 (a) – 4.6 (b) [89]. To generate the Raman image, we have employed the PS Raman spectrum and the major peak intensity of 1001 cm^{-1} as marked with an asterisk in Fig. 4.1 (b). We note that a potential advantage of the proposed scheme is its trapping stability against flow due to the 100% illumination duty cycle during trapping, i.e., constant optical gradient is maintained without instantaneous power fluctuations. An on-linemovie shows effective trapping against background flow as evidenced by the motion of untrapped microparticles. The proposed scheme can also trap multiple microparticles at different depths as shown in Fig. 4.7 (a) with the raw images of PMMA's Raman peak at 813 cm^{-1} from two beads with 5 μm separation shown in Fig. 4.7 (b). Apparently the spectrum from the out-of-focus bead is blurred, however, this could be improved via deconvolution techniques.

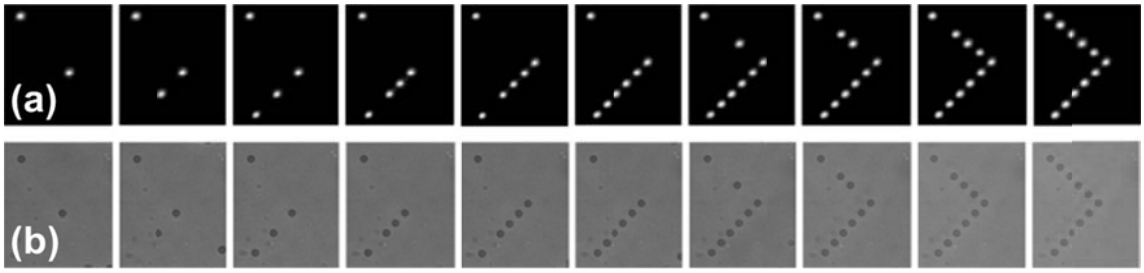

Figure 4.6 Simultaneous trapping and Raman imaging of 2 to 11 PS microparticles: (a) PS Raman image and (b) visual image.

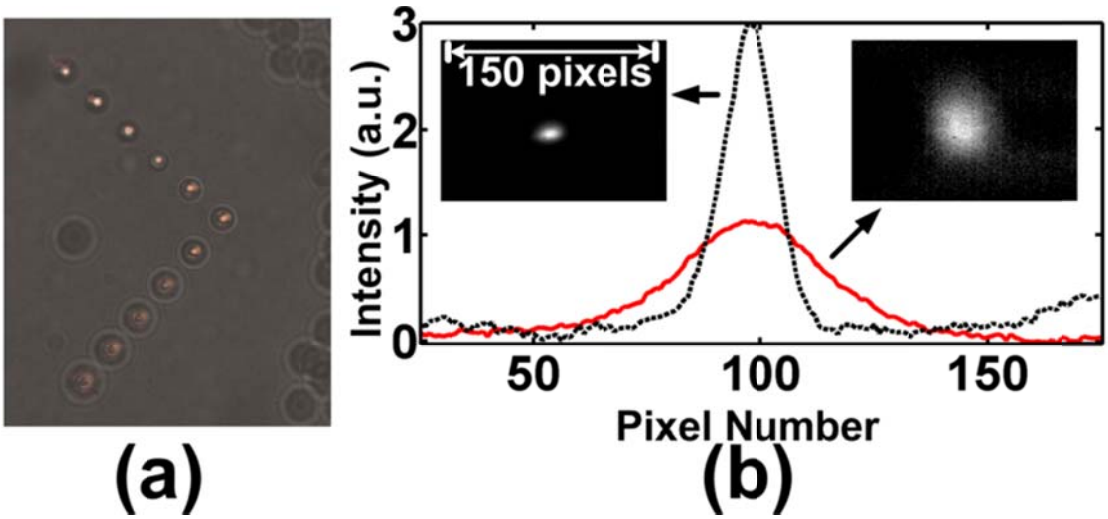

Figure 4.7 Multiple traps at different depths: (a) laser spots overlaid on 11 PMMA microparticles at different zs; (b) Raman intensity on the CCD of the in-focus (dotted) and out-of-focus (solid) PMMA microparticles by binning all rows.

4.6 Conclusion

In conclusion, we have demonstrated a novel scheme for parallel Raman microspectroscopy by combining programmable multi-point illumination and wide-field Raman imaging. This scheme provides flexibility to simultaneously image multiple points not aligned along a line in contrast to traditional power-sharing scheme using a line-shape illumination while retaining other features such as non-scanning, 100% duty cycle and constant power distribution on all spots within one CCD frame. This novel scheme may be applicable for ultra-high throughput Raman microspectroscopy and imaging, particularly when the sample is sparse or has unevenly distributed information density. In addition, this scheme can be effectively combined with optical traps with 100% duty cycle for facile multiplexed trapping and simultaneous Raman microspectroscopy.

Related publication

This chapter has been published as "Parallel Raman Microspectroscopy using Programmable Multi-point Illumination", J. Qi and W. C. Shih, *Opt Lett*, 2012, **37**, 1289-1291.

Chapter 5 High-speed Hyperspectral Raman Imaging for Label-free Compositional Microanalysis

5.1 Introduction

As mentioned previously, conventional laser scanning confocal Raman microscope involves long data acquisition time due to its sequential operation, as well as the additional latency from the readout time of low noise charge coupled device (CCD) detectors. As a result, conventional point-scan Raman mapping speed is about one to a few spots per second, or a few Hertz (Hz) [55].

To achieve a higher speed, point-scan is employed in more recent commercial Raman systems with an electron-multiplied CCD (EMCCD) detector. For strong Raman scatterers, an integration time ~ 1 ms per spot is possible, resulting in a speed ~ 300 Hz after taking into account the readout time. Although EMCCD can boost signal-to-noise ratio (SNR) under Raman photon-starving situation, amplification noise is unavoidable. For weaker Raman scatterers commonly seen in biological samples, however, the speed of the EMCCD-based system is severely lowered and approaches that of conventional non-EMCCD systems because much longer integration time per spot is needed. This barrier cannot be overcome simply by increasing laser power because of damaging and phototoxicity issues.

In contrast, parallel acquisition using a line-shaped laser pattern can achieve similar throughput without rapid scanning, and provides a means to fully utilize the available laser power without introducing phototoxicity. Raman photons originating from the entire line, equivalent to many spots, are imaged to the entrance slit of an imaging spectrograph. Therefore, the data acquired in one single frame is two-dimensional, i.e.,

hyperspectral in (x,λ), in the sense that it contains spatially resolved Raman spectra from multiple spots. Three-dimensional (x,y,λ) data can be obtained by scanning the laser line in the transverse direction [8]. Although effective, the line-scan approach suffers from a major limitation: parallelism is only possible for points lying on a line, which is not flexible for sparse scenes.

To overcome this inflexibility, we implemented a scheme to simultaneously collect hyperspectral Raman spectra from on average 12 spots per CCD frame using SLM generated active illumination patterns and wide-field image collection, as described in Chapter 4 [90]. However, high-speed Raman imaging was not demonstrated. In this Chapter, we present several key improvements. First, we have optimized the excitation optical path to achieve as many as 120 spots per pattern, which results in an unprecedented imaging throughput (~ 1 kHz) for strong Raman scatterers. Second, we have automated the centroid-finding, random spot pattern selection and hologram generation, thus eliminating the need for human intervention and enabling rapid imaging from non-uniform polymer microspheres and bacterial spores at unprecedented speed. Compared to the point-scan approach using an EMCCD camera, our system not only provides significant imaging speed advantage for various types of samples, but also permits substantially longer integration time per spot, leading to superior signal-to-noise ratio (SNR) data.

5.2 System Configuration

We have developed an integrated software and hardware approach as shown in Fig. 5.1 (a). Based on the active-illumination system described in Chapter 4, camera 1 (Dalsa, Pantera 1M30) is added to take bright-field image, which is analyzed to extract

centroids from samples. A series of "optimal" illumination patterns were then calculated automatically to avoid completely spectral mixing. Beside the CCD camera (Princeton 400BR), an EMCCD (Andor DU970) was employed with the same optical system for SNR comparison.

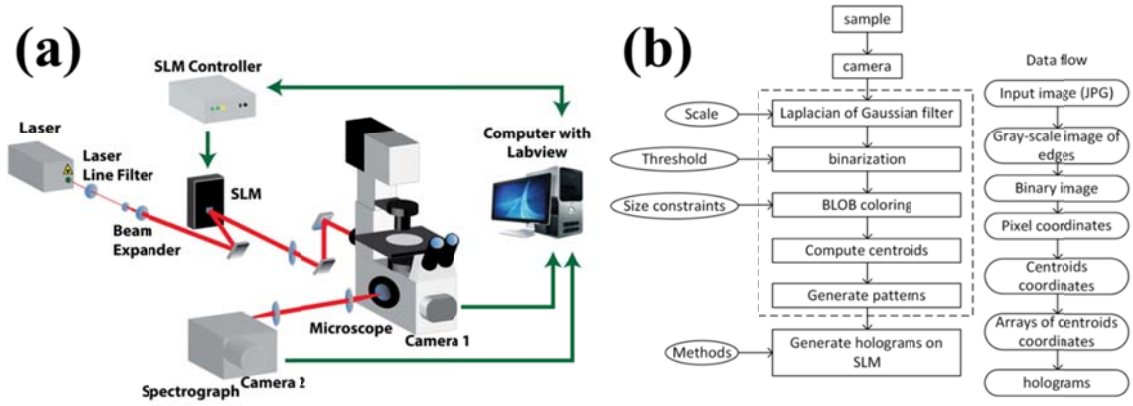

Figure 5.1 (a) System configuration; (b) image feature extraction, random pattern selection and hologram computation flow chart.

5.3 Image Feature Extraction, Hologram Computation and System Calibration

Figure 5.1 (b) shows the image analysis modules and data flow from a bright-field snapshot to hologram generation, implemented in Labview (National Instrument) with embedded MATLAB (Mathworks Inc.) script nodes in the dotted block. The image acquired by camera 1 was first passed to a second-derivative based Laplacian of Gaussian (LoG) filter for edge detection. The image was then binarized. Object detection was implemented by binary large object (BLOB) coloring. Connected areas were analyzed and assigned with a common label. Size constraint was added to eliminate outliers to avoid false positives of edge detection.

Once every object had a unique label, the centroids of individual objects were calculated by averaging the pixel coordinates within each object. These centroids were

the targets where focused laser spots would illuminate. To reduce spatio-spectral mixing from multiple points, the centroid image was split into several patterns automatically by maximizing the number of spots within one pattern under a constraint on the minimal vertical distance between any two spots. This was repeated until all the points were covered. Each pattern was represented by multiple spot positions (x,y) with respect to the SLM projection field coordinates. The spot positions were input into the hologram generation module one pattern at a time. The "generating holograms on SLM" module was implemented using Fourier transform-based Gerchburg-Saxton 3D algorithm.

Typically, the bright-field imaging coordinates and the SLM projection field coordinates did not co-register due to imperfect alignment. Thus, the laser spot "aiming" precision was not guaranteed. For uniform samples, this resulted in position errors in the final image, similar to registration or "stitching" errors commonly seen in point-scan imaging; for nonuniform samples, sub-optimal Raman spectra was obtained due to misaiming. In addition, mixed Raman spectra would have been obtained if the spot illuminates near the boundary of two microparticles of different composition. To address this issue, we have developed an automated calibration procedure using a uniform silicon wafer. First, an 11 × 11 spot array with 8 μm center-to-center distance was employed to form a grid covering the entire field of view. This grid array was then imaged and registered on the coordinates of the front port camera. In this way, we established a one-to-one mapping between the SLM projection field coordinates and the bright-field imaging coordinates. The grid array was then shifted in steps of 0.5 μm vertically and horizontally to improve the density of the mapping until a finer grid with 0.5 μm spacing between adjacent spots were established within the field of view. This calibration

procedure resulted in a look-up table for guaranteed precision ~0.5 μm. In our experience, precision ~ 0.2 μm can be achieved, which is smaller than the system resolution.

5.4 Experimental Results

5.4.1 Performance on Silicon Substrates

Since the Raman scattering cross-section of silicon is orders of magnitude larger than common materials, it represents a good model for us to test the ultimate speed of our system. In this experiment, 19 random patterns, each with 121 spots, were employed with 15 ms integration time per CCD frame, resulting in 2299 spots in 2.3 seconds, or equivalently ~ 1 kHz. We note that the minimum integration time was limited by the mechanical shutter which requires ~ 10 ms to open and close. Figure 5.2 (a) shows the overall image using silicon's Raman peak at 520 cm^{-1} after background removal.

5.4.2 Wavenumber Calibration

To examine the dependence of Raman shifts on the lateral (x) position of laser spot, we have performed experiments using acetaminophen powder and silicon wafer samples. A single laser spot was scanned across the entire field of view (100 μm) at 5 μm step size. The results shown in Fig. 5.2 (b) suggest that the motion of the peak positions is highly linear with respect to the laser spot motion, as expected. These curves have been employed in previous results to calibrate the Raman shifts for each laser excitation spot and as the fitting result indicates, the calibration error is far less than one pixel.

5.4.3 Signal-to-noise Ratio Comparison between Different CCD Detectors

A distinct advantage of our system is that significantly longer integration time can be used compared to rapid point-scan systems using EMCCD, where an integration time on the order of milliseconds are necessarily for high throughput. As shown in Fig. 5.2 (c)

and 5.2 (d), the signal-to-noise ratio (SNR) of silicon obtained by the EMCCD was 1.9 and 4 for 1 ms and 10 ms CCD integration time, respectively. In contrast, as shown in Fig. 5.2 (e), the SNR obtained by the low-noise CCD is 27 for 25 ms integration time. We note that a similar SNR was obtained in our previous silicon data at nearly 1 kHz. Therefore, our system not only is 3 times faster than the point-scan-EMCCD approach, but also provides superior SNR in the acquired images.

5.4.4 Chemical Classification of Polymer Microparticles

Next, we demonstrate the system performance using a mixture of 1679 2 μm polystyrene (PS) and melamine resin (MR) microspheres, which appeared identically in the bright-field image shown in Fig. 5.3 (a). Figure 5.3 (b) shows the identified centroids, among which ~15% were randomly selected and split into 4 sub-groups under the condition that >2 μm vertical separation between any two centroids in the same sub-group, preventing substantial spatiospectral mixing. Nevertheless, as long as two spots did not completely aligned horizontally, pure spectra from either bead can always be obtained from the edges of the beads for identification purpose under the assumption that these are homogeneous beads (discussed later). Figure 5.3 (c) shows the 4 color-coded sub-groups with the corresponding 4 holograms in Fig. 5.4 (a) – 5.4 (d), using which Raman images were collected in Fig. 5.4 (e) – 5.4 (h). As summarized in Fig. 5.5 (a), a total of 245 microspheres were sampled, among which 129 were PS (blue) and 116 were MR (red) based on their distinct Raman spectra shown in Fig. 5.5 (b). The data acquisition duration was 1.5 sec, or 163 Hz.

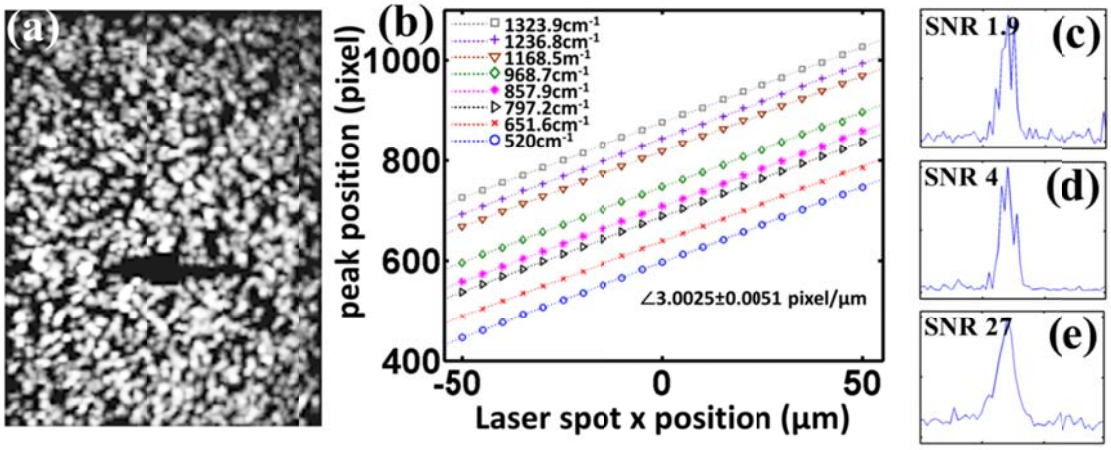

Figure 5.2 (a) Silicon image using the 520 cm^{-1} peak; (b) Measured peak positions vs. laser spot x position using acetaminophen Raman peaks and silicon Raman peak; (c), (d) and (e) silicon spectra acquired by EMCCD, and low-noise CCD, respectively.

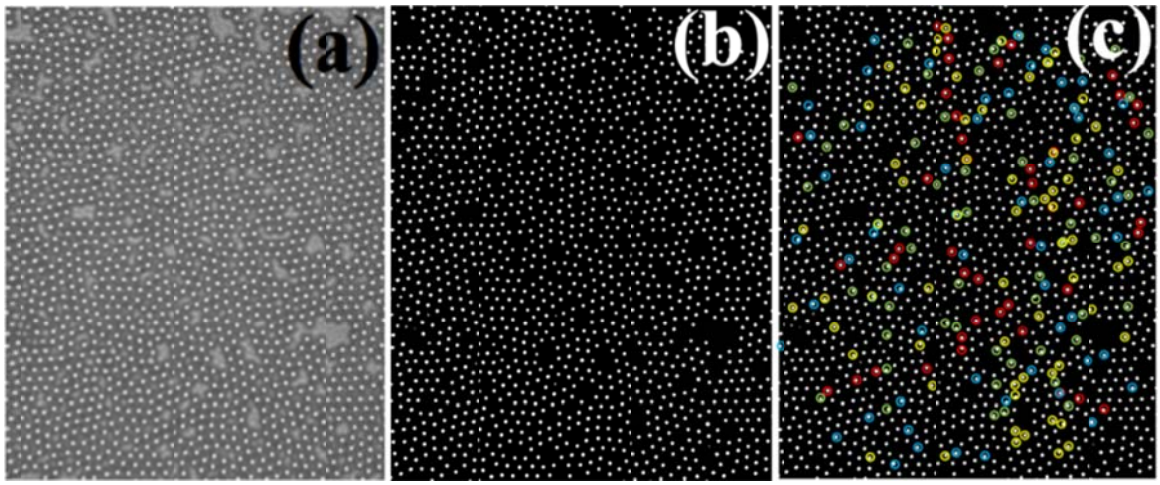

Figure 5.3 (a) Bright-field image of a mixed sample of 2 μm PS and MR microspheres; (b) binarized centroid image after image processing; (c) random selection of 15% of microspheres and splitting into four color-coded groups (patterns).

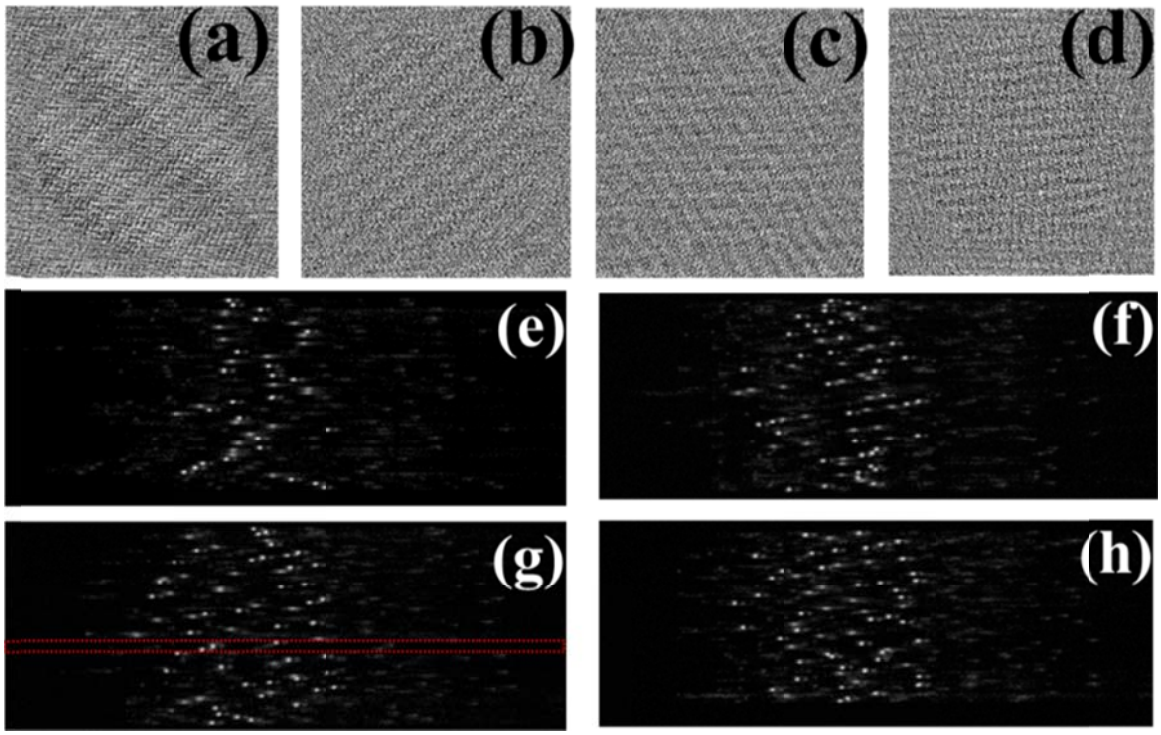

Figure 5.4 (a-d) Holograms corresponding to the four groups (patterns) selected in Fig. 5.3 (c); (e-h) raw Raman images corresponding to the illumination patterns according to the holograms in (a-d).

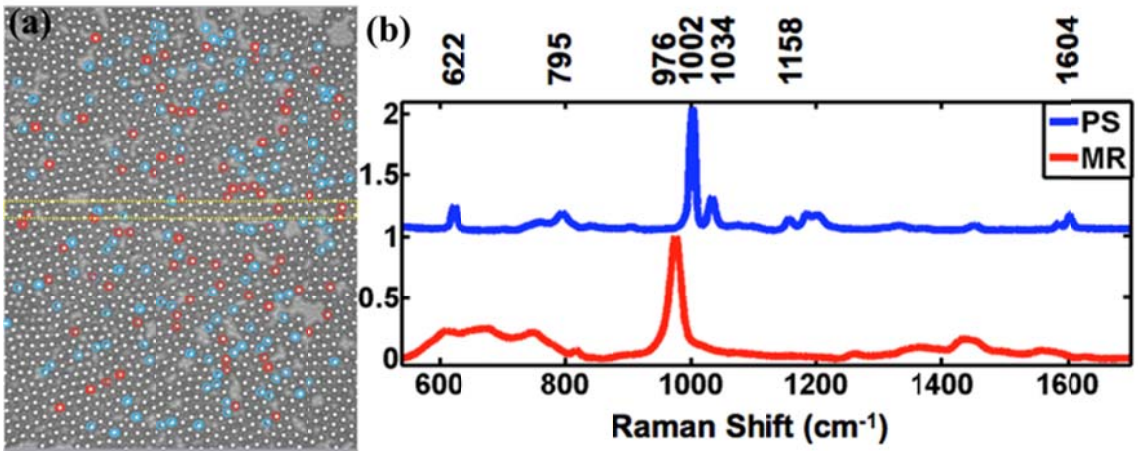

Figure 5.5 (a) Classification of polymer microparticles with PS marked by blue circles and MR red circles; (b) Raman spectra of PS and MR with major peaks used in classification.

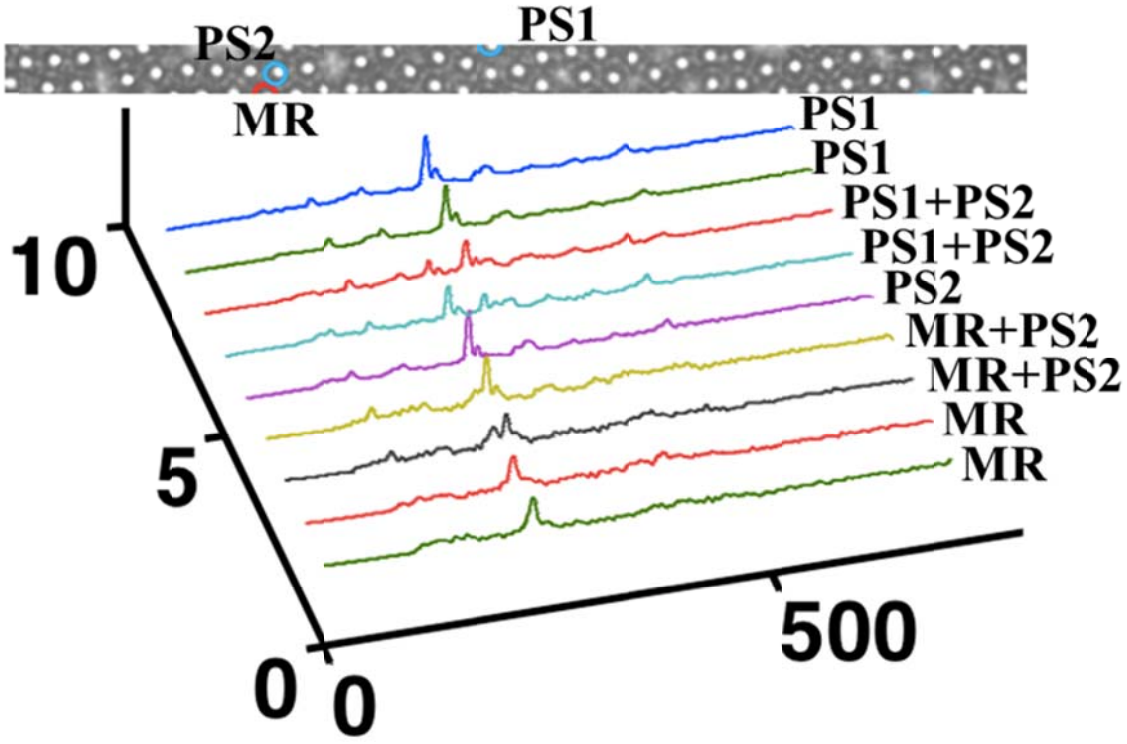

Figure 5.6 (top image) Three microparticles of interest are illuminated by three laser spots in the windowed region in pattern #3, or Fig. 5.4 (g); (bottom spectra) Raman spectra from the nine CCD rows corresponding to the same region in the top image.

As mentioned earlier, in most situations, the patterns satisfy the condition that the vertical separation between any two centroids selected in the same sub-group are larger than ~2 μm. To further elucidate how the minor spatiospectral mixing is not an issue, we take a closer look at a region outlined by a red window in Fig. 5.4 (g), i.e., pattern #3. As shown in Fig. 5.6 (top image), three laser spots were employed in the windowed region of illumination pattern #3 to sample three microspheres, PS1, PS2 and MR. The spectra from nine adjacent CCD rows corresponding to this region are also plotted in Fig. 5.6 (bottom), where spatiospectral mixing was observed. However, we can correctly classify these spectra into PS1, PS1 + PS2, PS2, MR + PS2 and MR since we know exactly what

the Raman spectra of PS and MR are and the locations of the laser spots with respect to the microparticles.

5.4.5 Chemical Identification of Bacterial Spores

The study of spore formation under harsh environmental conditions is of great interest in microbiology. In addition, it is critical to detect and analyze spores in biofilms in order to develop optimal treatment strategies. Using Bacillus subtilis spore as a model specie, we are interested in learning the chemical changes during sporulation and the germination processes at the population level. As shown in Fig. 5.7 (a), we have split ~100 spores into 4 sub-groups and employed 4 illumination patterns to acquire their Raman spectra within 40 seconds, equivalent to 2.5 Hz, which compares favorably against 2 spore/min or 0.033 Hz in the best throughput ever reported [91]. A map was generated in Fig. 5.7 (b) using the prominent peak at 1017 cm^{-1} of dipicolinic acid abundant in spores. Representative spore spectra are shown in Fig. 5.7 (c).

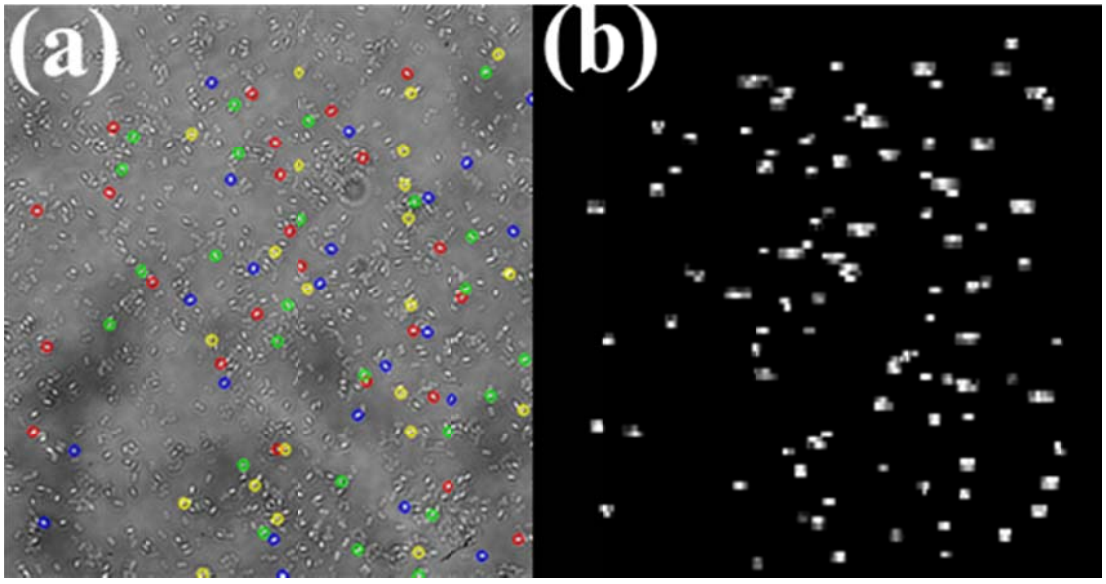

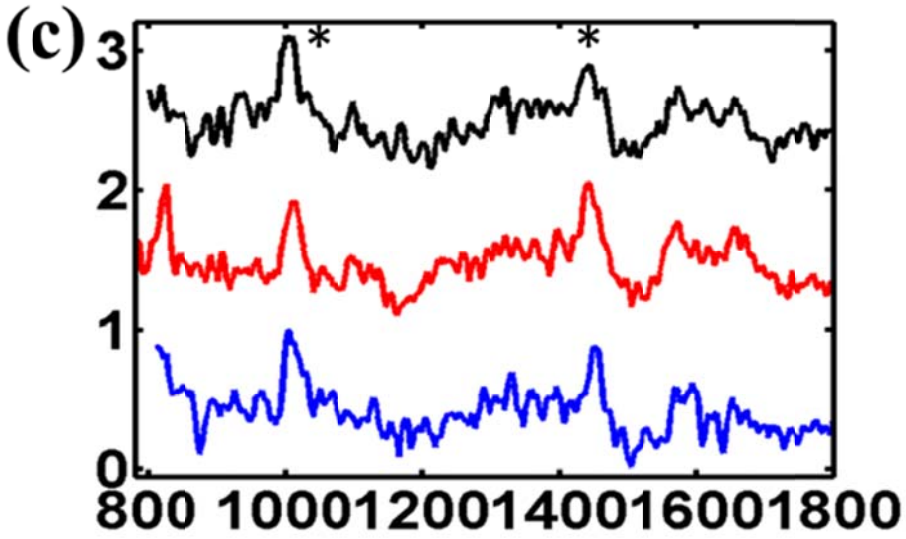

Figure 5.7 (a) bright-field image of spores and 4 color-coded sub-groups for 4 illumination patterns; (b) corresponding Raman image by 4 illumination patterns; (c) representative spore Raman spectra with characteristic peaks marked by *.

5.5 Conclusion

In conclusion, we have developed a high-speed hyperspectral Raman imaging system with integrated image-guided active illumination. We have shown that high-quality Raman spectra can be acquired from as many as ~1,000 micron-sized spots/sec semi-randomly distributed among a ~100x100 μm^2 field of view without mechanical scanning. We have demonstrated rapid compositional microanalysis of three types of samples with various Raman scattering strength. Compared to the point-scan with EMCCD approach, the results suggest that our system not only provides significant imaging speed advantage for various types of samples, but also permits substantially longer integration time per spot, leading to superior signal-tonoise ratio (SNR) data. The demonstrated new capabilities could have significant impact in Raman image acquisition in biological or biomedical applications.

Related publication

This chapter has been published as “High-speed hyperspectral Raman imaging for label-free compositional microanalysis”, J. Qi, J. T. Li and W. C. Shih, *Biomed. Opt. Express*, 2013, **4**, 2376-2382.

Chapter 6 Analysis of Biological tissue and Tumor Margin Detection Using Raman Spectroscopy and Optical Coherence Tomography

6.1 Introduction

The ability of detect disease rapidly has manifold advantages, including simpler and more effective treatment at early stage, monitor the progression of therapy and significant reduction in morbidity [92]. It is known that some of the clinical tests are prolonged and unreliable [93-96]. Thus, improving the accuracy in the early diagnosis and quantitative identification of severity are of great interest. Besides, current technique for tumor resection involves biopsy and histological confirmation, which is time consuming and requires sacrifices of healthy tissue, motivating the development of novel techniques to enable real-time and accurate margin detection. Raman spectroscopy which provides molecular specificity and optical coherence tomography (OCT) that is capable to perform real-time cross sectional imaging with micrometer-scale resolution, has been employed to early diagnosis and identify intraoperative margin [58]. In this Chapter, we present the first application of combining information from line-scan Raman microscopy (LSRM) and optical coherence tomography (OCT) imaging for tissue analysis and the assessment of diseased/normal boundary.

6.2 Resection Margins

Accurate and real-time intraoperative tumor margin assessment is of utmost importance in tissue-preserving surgical procedures such as partial mastectomy for breast cancer [97, 98], prostate [99] and brain tumor excision [100], organ-sparing surgery for liposarcoma [101], and many others. In these surgical procedures, complete excision of the primary tumor is the major determinant of the rate of local cancer recurrence.

Minimizing the removal of normal tissue is the main factor in preserving proper organ functions as well as cosmetic appearance. Thus, in successful procedures, complete resection of the cancer must be balanced with tissue conservation. To ensure that all malignant tissue is removed, a small margin of normal tissue surrounding the lesion is excised to ensure that the surgeon removed the entire malignant lesion. Margin status is gauged by pathologic examination of the border of the excised lesion – a two-step process. The first step is intraoperative gross (macroscopic) examination by a surgeon with a naked eye; the second step is postoperative histologic (microscopic) examination using frozen sections stained with hematoxylin and eosin to evaluate a representative area of concern. Achieving negative resection margins, typically defined as the absence of malignant tumor cells, provides lower associated rates of future local recurrence [102]. Positive or unknown histological margins usually prompt re-excision surgery because of the elevated risk for local recurrence even when chemo/radiation therapy is administered [103]. In the case of breast cancer, for example, as many as 20% to 55% of patients undergoing partial mastectomy require a second surgical procedure due to positive margins indicative of incomplete cancer resection that were missed on intraoperative margin assessment [58].

Currently, a variety of optical imaging and spectroscopic techniques are being explored to improve disease diagnosis, such as diffuse reflectance spectroscopy and fluorescence spectroscopy. However, the application of these methods for intraoperative surgical margin assessment is very limited. Preliminary in vivo results have shown the efficacy of diffuse reflectance spectroscopy in the diagnosis of breast lesions, as well as in the assessment of tumor margins [104]. This technique has shown great promise in the

assessment of large-volume tumors, but cannot provide localized information regarding tumor margins due to low resolution. OCT, in contrast, can provide high resolution images in three dimensions. OCT has been employed in various real-time applications, for example, monitoring blood flow *in vivo* and anterior segment imaging, based on detection of optical attenuation and elastic properties. However, OCT cannot provide efficient accuracy to identify tissues with similar optical and structural properties, such as small intestine and kidney. Raman spectroscopy, on the other hand, has been employed to identify intraoperative margin based on tissue variations at the molecular level. In recent literatures, a dual-mode system has been developed to collect point-wise Raman spectra and OCT images from biological tissue [105-107].

6.3 Material and Methods

6.3.1 OCT Systems

Two OCT imaging systems are involved in this work, a time domain system and a spectral domain system. Measurements are performed *in vivo* for mouse tissue analysis using time domain OCT and *ex vivo* for cancer diagnosis and margin detection using spectral domain OCT.

The time domain system [108] applies a low-coherence light source with a central wavelength of 1310 nm, and a bandwidth of ~ 30 nm. The axial resolution of the system is ~ 25 μm in air. Light in the sample arm of the interferometer is directed into the tissues through a miniature scanning endoscopic probe with the diameter of ~ 3 mm (Imalux Corporation, Cleveland, Ohio). The in-depth (z axis) information of the sample is achieved by the piezoelectric modulation of the optical path in the reference arm. Two-dimensional images of samples were obtained with the size of 450 pixels × 450 pixels

and the dimension of 2.2 mm (axial) × 2.4 mm (transversal). The B-mode imaging rate was ~0.25 Hz and the operation of the OCT system was fully controlled by PC.

The spectral domain system comprises of a broadband superluminescent laser diode (broadlighter S840, Superlum, Russia, 840±25 nm wavelength range, 20 mW output power) at the source end, Michelson interferometer with 50/50 split ratio to the sample and reference arms and a spectrometer at the detector end. The spectrometer comprises of a diffraction grating (Wasatch Photonics, 1200 grooves/mm) and a CCD line scan camera (Basler L104K, 2048 pixel resolution, 29.3 kHz line rate). The interference signal from the sample and the reference arms of the Michelson interferometer is detected by the spectrometer and digitized by an image acquisition card (NI-IMAQ PCI-1428). Depth profile (A-line) is obtained by converting the interference signal detected by the IMAQ into linear k-space and then performing fast Fourier transform (FFT) algorithm on it. 3D imaging is performed by scanning the laser beam across the surface of the sample, at the sample arm, using galvanometer mounted mirrors. The SDOCT system has an axial (at 3 dB drop) and transverse resolution of 8 μm and an imaging depth of 4.5 mm (in air).

6.3.2 Line-scan Raman Microscope (LSRM)

The LSRM system used in this study is described in Chapter 3. Measurements are performed *ex vivo* in the same organ as with the OCT experiment. Tissue samples were placed on fused silica coverslips and fixed at the sample holder of microscope. The laser line projected at the sample was 133 μm long. 133 spectra were collected simultaneously with a total acquisition time of 60 s at a power density of 1 $mW/\mu m^2$ to obtain decent SNR. The spectra were based line corrected using adaptive iterative reweighted penalized

least squares algorithm (airPLS) [109] and the 133 corrected spectra were averaged as one spectrum representing one position.

6.3.3 Animal Manipulation

All the animal manipulation procedure described below has been approved by the Institutional Animal Care Committee (IACUC) of University of Houston. Six mice were housed under specific pathogen-free conditions in the animal facility. In OCT experiments, three mice were utilized and these mice were deeply anesthetized through the use of isoflurane gas mixed with oxygen for the *in vivo* experiments. Another three mice were used for the RS experiments with *ex vivo* tissue conditions. For RS experiments, the animals were euthanized and organs such as kidney, small intestine, and liver were harvested. The RS study followed immediately after extracting the organs from the mice. The total process of organ extraction was within 20 minutes.

6.3.4 Cancer Tissue Preparation

Tissue samples were obtained after surgical resection at The University of Texas, M.D Anderson Cancer center (UTMDACC) hospital under an IRB approved protocol with patient consent, stored in sterile phosphate buffered saline (PBS) and imaged using SDOCT system on the same day. A small part of the sample was dissected to be imaged by the LSRM. The rest of sample was fixed in formalin and prepared for histological analysis. Tissue samples to be imaged by LSRM were placed onto No.1 coverslips and fixed at the sample holder of microscope. The total acquisition time for each spectrum is 60 sec at a power density of 1 mW/ μm^2. The Protocols for tissue processing were approved by the University of Houston Biosafety committee.

6.3.5 Classification by Support Vector Machines

Multi-support vector machine is a common machine-learning tool used to classify new unknown data (testing data) based on experiences from a data set of known data (training data) among multiple classes. We selected one-versus-all (OVA) method [110] with a radial basis function (RBF) kernel. The OVA method is one of the methods to decompose a multiclass problem into two-class problems. The aim of OVA is to classify the data into the class that has the highest decision value compared with the remaining classes. The 5-fold cross validation is applied to verify this model. An example of this method is shown in Fig. 6.2 (c). First, all the data points on the Fig.6.2 (c) are split randomly into five groups and the classification model (RBF kernel) is trained with four groups. The fifth group is considered as the testing sample for predicting the accuracy. This is repeated for 5 times. During each time, classifiers are internally constructed with M times if there are M classes of the training data. In the prediction stage, the classifiers follow the "winner takes all" principle that the testing sample is classified into the class with highest decision value. In addition, the classifiers with different cost and gamma parameters indeed influence the prediction accuracy, thus, we search the best cost and gamma parameters by a grid search method. Also, 5-fold cross validation is utilized to optimize best parameters.

6.4 Results and Discussion

6.4.1 Classification of Mouse Tissue using OCT and LSRM

In this study, we present a combined analysis of OCT/RS with the proof-of-principle experiments performed on mouse abdominal organs, including intestine, kidney and liver. Typical OCT images of the small intestine, kidney and liver are shown in Fig.

6.1. It is fairly difficult to find the structure difference based on visual observation. The slope values of small intestine, kidney and liver were quantified as 0.67 ± 0.102 μm^{-1}, 0.84 ± 0.038 μm^{-1} and 0.95 ± 0.046 μm^{-1}, respectively, as shown in Fig. 6.2 (a). The standard deviation (SD) values were computed as 112.06± 2.89, 112.97 ± 1.49, and 106.20 ± 0.70 in an arbitrary unit. From the statistical results, the mean slope value of liver is the largest because of much denser distribution of erythrocytes within connective tissues and capillary vessels than the others [111]. On the other hand, based on the aspect of image speckles, the result of the SD values in Fig. 6.2 (b) suggests that the variations of refractive index in the structure of small intestine and kidney are greater than liver. To further verify the significant difference, two-dimensional Kolmogorov–Smirnov test (K–S test) has been performed on the OCT data in Fig. 6.2 (a) and 6.2 (b), and it turns out that the P values of the slope among the three types of samples are all smaller than 0.001, but the P values of the SD between kidney and SI are more than 0.05, which suggests that the SD values of intensity A-lines cannot correctly differentiate small intestine from kidney.

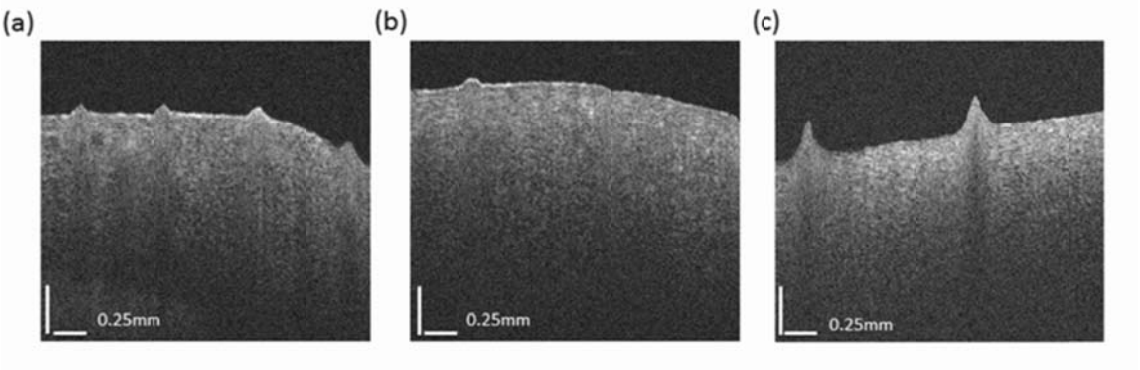

Figure 6.1 Typical OCT images from different organs, (a) small intestine, (b) kidney and (c) liver, the sharp pulses in (a)-(c) were caused from the body motion. Scalar bars are equal to 0.25 mm.

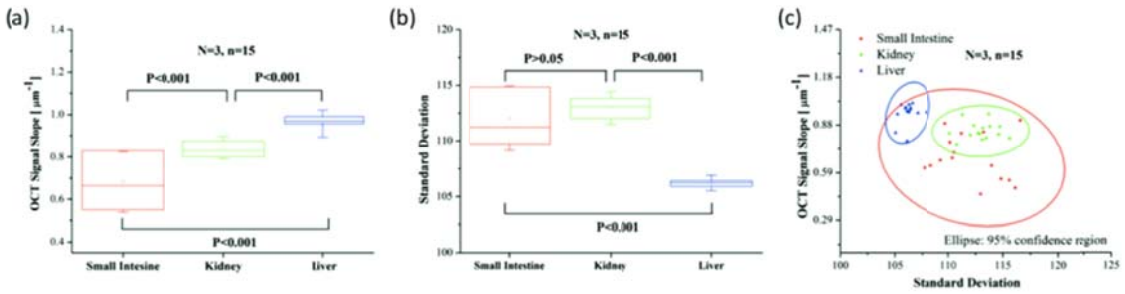

Figure 6.2 Box plots of (a) the slope and (b) the SD for the organs of small intestine, kidney, liver; N=3, n=15 (N and n are the sample size of mice and measured position respectively). (c) Scatter plot of the 2D distribution of the values of slope and SD.

The two-dimensional scatter plot with 95% confidence region reveals that small intestine and kidney cannot be well differentiated, as shown in Fig. 6.2 (c). In Table 6.1, the predication accuracy of simply OCT texture analysis is 84.4%. Also, Table 1 demonstrates that OCT analysis has relatively better performance to classify liver because of its distinct optical and structural properties while SI and kidney show worse prediction than liver. This result demonstrates that OCT analysis alone is not sufficient to identify small intestine and kidney although it provides high-resolution images and optical properties. Consequently, the performance of the organ classification can possibly be further improved by means of the assistance of LSRM due to its superior molecule specificity.

Table 6.1 Confusion table for the SVM classification model based on OCT detection only. The optimized cost value and gamma are 5 and 0.25respectively for the training model.

		Predicted Labels		
True Label		Small Intestine	Kidney	Liver
	Small Intestine	11	4	0
	Kidney	2	13	0
	Liver	1	0	14

Figure 6.3 (a) presents the average Raman spectra from small intestine, kidney and liver. Tentative band assignments are shown in Table 6.2. In Fig. 6.3 (a), the average Raman spectrum of normal liver indicates the prominent peaks at 1132, 1169, 1207, 1307, 1395, 1450, 1549, 1601 and 1659 cm^{-1}. Similar observance can be found in the literature [112]. The characteristic Raman peaks of kidney are 1132, 1276, 1306, 1456, 1549, 1617, 1662 cm^{-1}. These fingerprints are consistent with previous studies. Furthermore, the predominant peaks of small intestine at 1166, 1213, 1306, 1457, 1660 cm^{-1}, are in accord with the literature [113]. Among the comparison of the three in Fig. 6.3 (a), the Raman bands of liver show the identifiable peaks based on molecular information at 1169 cm^{-1} (C-H in-plane bending mode of tyrosine), 1207 cm^{-1} (Amid III), and 1601 cm^{-1} (phenylalanine). Particularly, in high frequency band, the strong Raman intensity at 1601 cm^{-1} is observed as the most obvious feature for identifying the liver from the others. Besides, the characteristic peaks of kidney at 1549 cm^{-1} (C-N stretching mode/Amid II), 1617cm^{-1} (Tyrosine), and 1662 cm^{-1} (Amid I) have the major difference compared with the liver and small intestine while the Raman band of small intestine has the strongest peak at 1660 cm^{-1} but no peaks from the range of 1500 cm^{-1} to 1620 cm^{-1}.

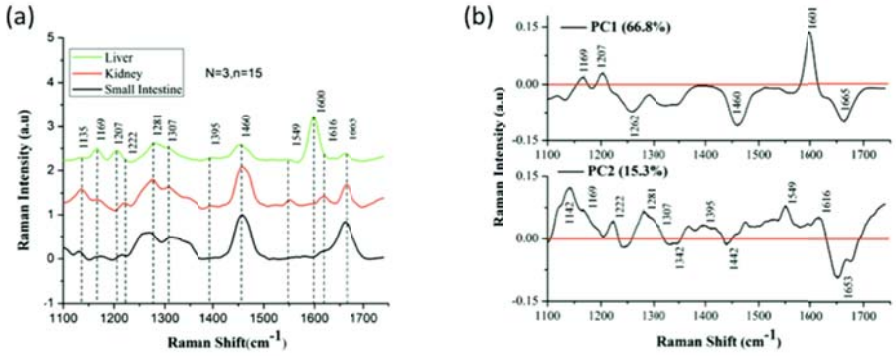

Figure 6.3 (a) Average spectra of the different types of organs and (b) the loading plot of PC1 and PC2.

Table 6.2 Tentative band assignments for small intestine, kidney and liver.

Band Assignment			
Liver	Kidney	Small Intestine	
1132	1132	1134	C-N stretching [114]
1169	1169	1166	Tyrosine [114]
1207		1213	Amid III [115]
1281	1276	1281	Collagen [115]
1307	1306	1306	CH_2 bending, Collagen [112]
1395			Hemoglobin [112]
1450	1456	1455	CH_3/CH_2 bending [116, 117]
1549	1549		C-N stretching/Amid II [118]
1601			Phenylalanine [115]
	1617	1614	Tyrosine [113, 115]
1659	1662	1660	Amid I [113, 115]

The data of Raman spectra were analyzed using principle component analysis (PCA) to extract the principal components and their associated scores. In Fig. 6.3 (b), the spectral variances of PC1 and PC2 were computed as 66.8% and 15.3% respectively. The principal component loadings suggest that liver can be clearly differentiated by PC1 at the peaks 1169, 1207, 1460, 1601, 1665 cm^{-1} as well as kidney at the peaks 1142, 1169, 1222, 1281, 1395, 1460, 1549, 1616, 1653 by PC2. The score plot of PC1 versus PC2 is shown in Fig. 6.4 (a). Compared with the scores of PC1, the scores of PC2 are more confident to identify intestine and kidney. By calculating the two-sample unequal-variance t-test, all the P values of PC2 among intestine, kidney and liver show significant differences (< 0.001), demonstrating that the PC2 values can successfully detect small intestine, kidney and liver. The computed result of multi-SVM shows that PC2 combined with PC1 has 100% prediction accuracy for classifying these three types of organs. From Fig.6.4, the scores of PC2 are suitable to improve the inability of OCT images for differentiating small intestine, kidney. Besides, the scores of PC1 can be utilized to

further assist the performance of OCT signal slope (OCTSS) for liver classification. In the comparison with the SD result, the values of OCTSS have less overlap area between small intestine and kidney. Thus, we combined the scores of PC2 and PC1 with OCTSS based on the homogeneous assumption on the sample surface and achieved Fig. 6.4 (b).

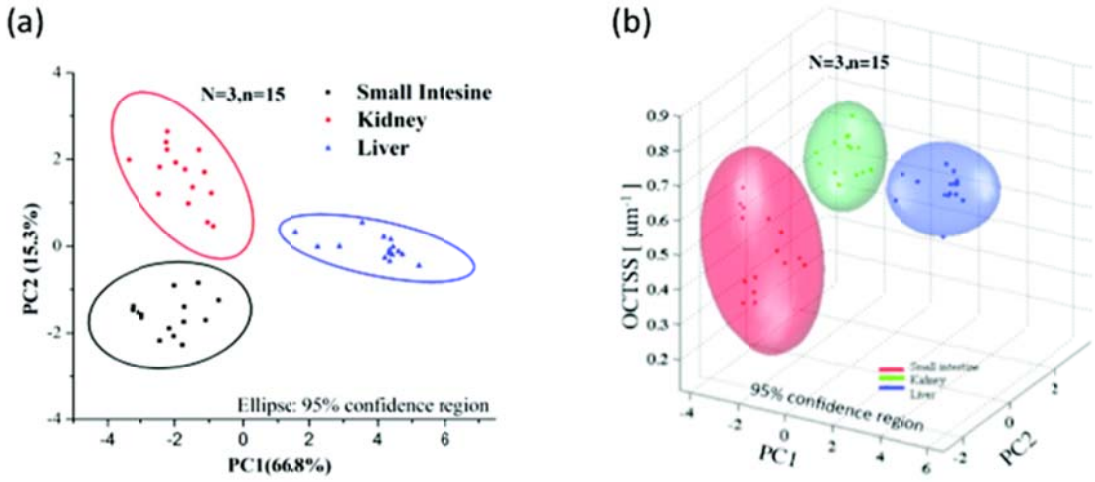

Figure 6.4 (a) Scatter plot of PC1 and PC2 and (b) scatter plot of the three-dimensional distribution of the values of OCTSS, PC1 and PC2.

6.4.2 Cancer Diagnosis and Margin Detection

In this study, we present the prospect of combining structural information from OCT and molecular information from LSRM, for tumor border identification during tumor resection surgeries. The similarity between OCT structural images and H&E histology images of normal fat, well differentiated liposarcoma (WDLS) and dedifferentiated liposarcoma (DDLS) has already been shown previously [119]. These results suggested that the structural differences between normal fat, WDLS and DDLS are easily identifiable from their corresponding OCT structural images. Hence, OCT can be used for used for gross inspection of tumor margins. However, in cases where

differences in OCT structural images are not very obvious, LSRM can be used for confirming the molecular information from the suspicious regions. To check consistency, Raman spectra were obtained from 7 different samples of normal fat tissue. The averaged Raman spectral information from normal fat samples is depicted in Figure 6.5. The gray shade represents the ±1 standard deviation that is less than ±5%.

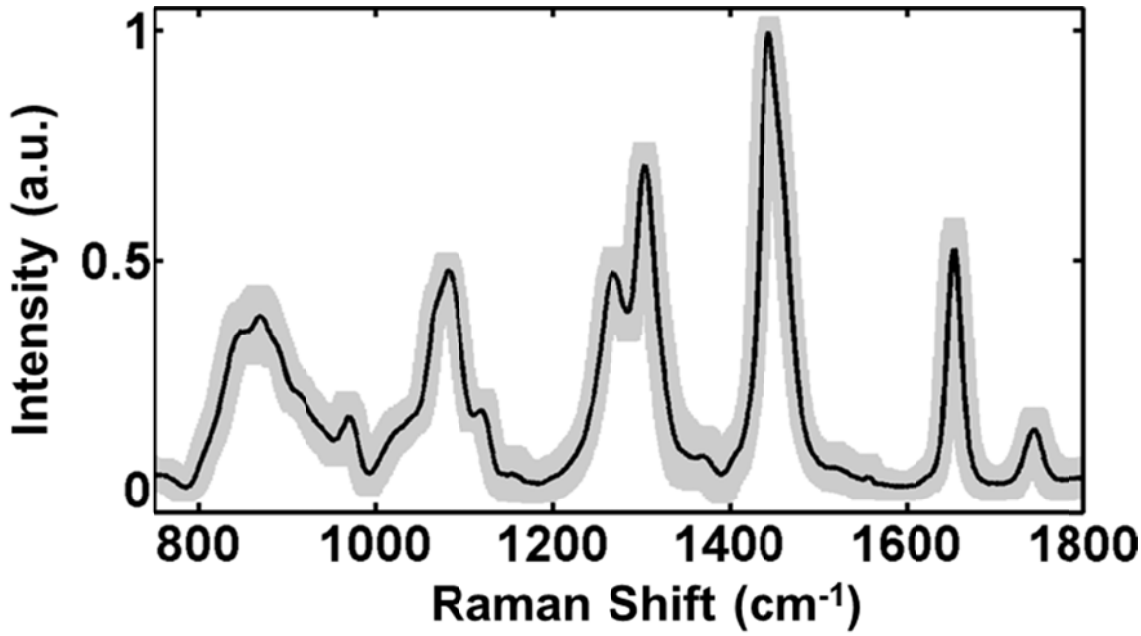

Figure 6.5 Average Raman spectra from normal fat tissue with gray shade representing ± 1 standard deviation.

Figures 6.6 (a) and 6.6 (b) shows OCT structural image and the corresponding H&E histology of myxoid liposarcoma, respectively. Myxoid liposarcoma is comprised of copious amorphous mucoid material with admixed small, stubby spindle cells and a variable number of neoplastic adipocytes of various sizes [120], as evident by the white and black arrows in Fig. 6.6 (a) and 6.6 (b), respectively. Figure 6.6 (c) is a representative OCT structural image of normal surrounding fat tissue. The margin between normal fat

and myxoid liposarcoma is shown by the white arrow in Fig. 6.6 (d). There is a clear difference in the OCT structural images between normal fat and myxoid liposarcoma. This obvious difference in structures will be very helpful to the surgeon to determine the tumor margin while performing resection surgery. We also studied capability of LSRM to differentiate between normal tissue and tumor regions. A bright field microscopic image of the surface of the sample was captured by a CMOS camera which is shown in Fig. 6.7 (a). The black dashed curve on Fig. 6.7 (a) indicates the boundary between myxoid liposarcoma (Region 1) and normal fat (Region 2). The laser line projection on the sample, imaged by the LSRM, is indicated by the solid red line in Fig. 6.7 (a). We emphasize that spatially resolved Raman spectra from this entire line (133 μm long) were captured in one CCD image of Raman shift (x-axis) and spatial coordinates (y-axis) (Fig. 6.7 (b)). The spectra from the abnormal region have lower Raman intensity compared to the normal spectra, possibly due to the lack of cellular structures and thus less elastic back scattering, agreeing with the OCT measurements. Figure 6.7 (c) compares the spectra, averaged over 21 spectra from cancerous region (A) and the normal region (B) respectively, These spectra are post-processed by first subtracting a glass coverslip fluorescence background followed by an automated background subtraction method [121]. Comparing the normal and the abnormal spectra, the intensity ratio of lipid bands at 1448 cm^{-1} (CH_2 bending) and 1655cm^{-1} (C=C stretching) changes from 2:1 in the normal to 1:1 in the abnormal region, agreeing with previous studies [122]. Biochemically, this agrees with the decrease in the ratio of monounsaturated lipids to polyunsaturated fatty acyl chains of lipids in liposarcoma compared to normal tissue. We also observe the broadening of the 1655 cm^{-1} peak in the abnormal region. A Raman

spectrum acquired from a separate healthy tissue is shown in Fig. 6.7 (d), which appears to be virtually identical to trace B in Fig. 6.7 (c).

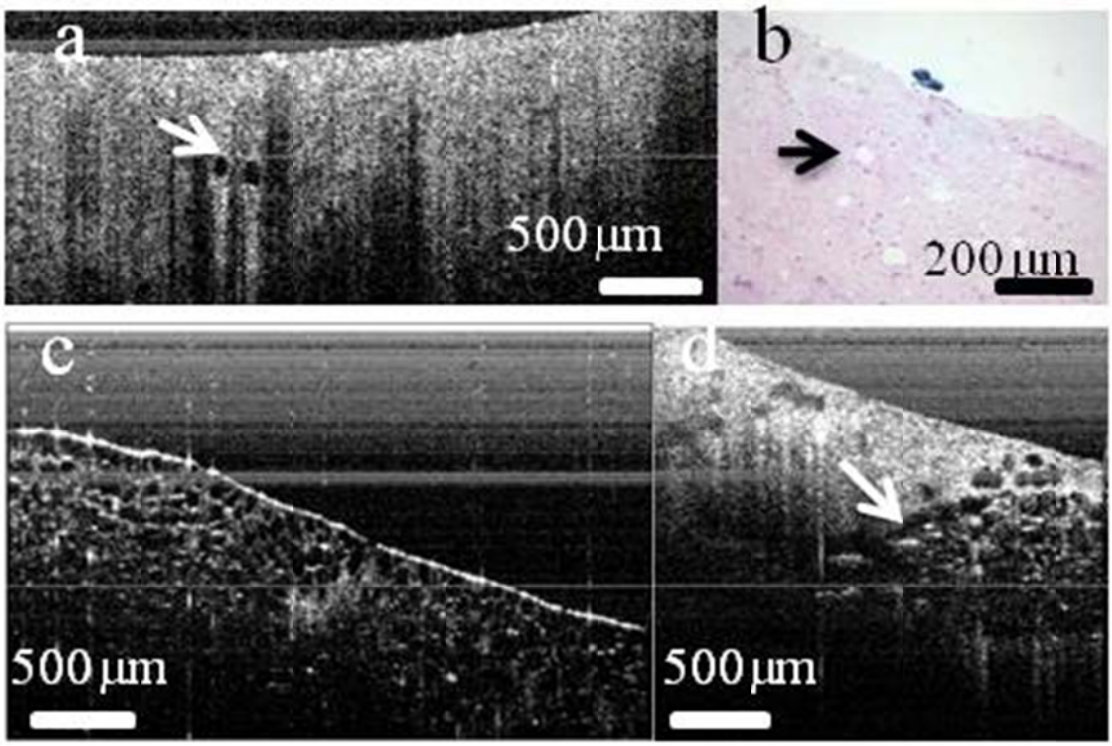

Figure 6.6 (a) 2D OCT structural image of myxoid liposarcoma; (b) H&E histology section corresponding to (a); (c) 2D OCT structural image of normal fat; (d) 2D OCT structural image depicting boundary between myxoid liposarcoma and normal fat.

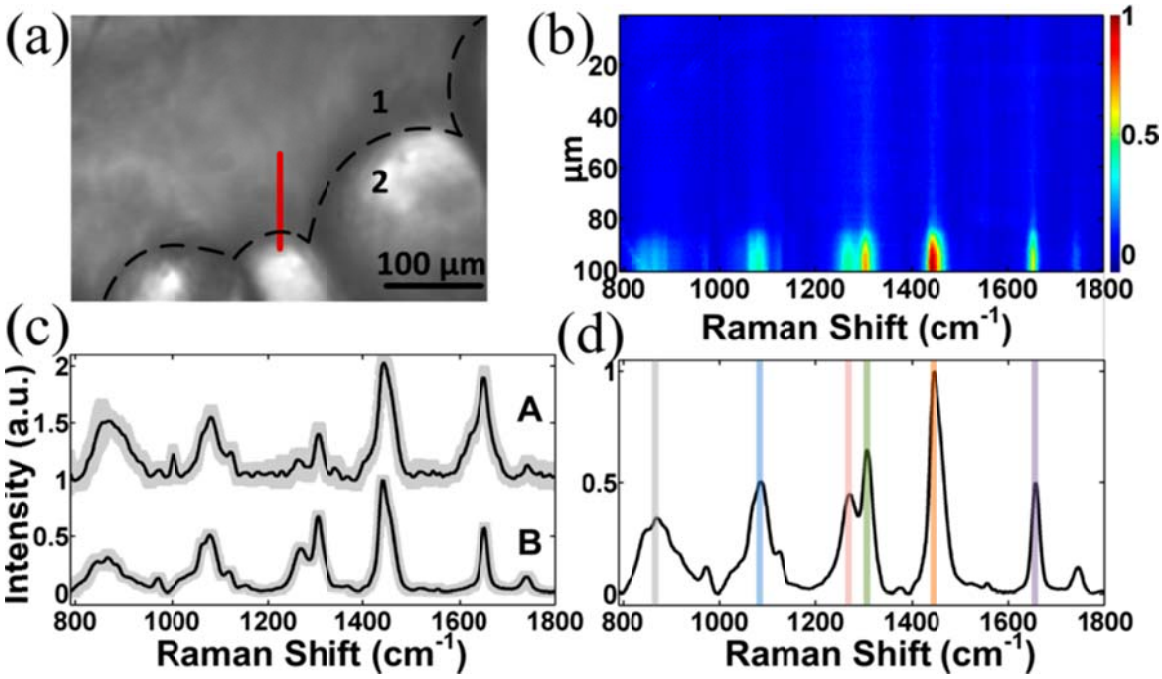

Figure 6.7 (a) Bright field image; (b) LSRM image corresponding to red line in (a); (c) averaged Raman spectrum from regions corresponding to myxoid liposarcoma (A) and normal fat (B); (d) averaged Raman spectrum from a different normal fat tissue.

In the case of myxoid liposarcoma and normal fat tissue, the differences in their corresponding OCT structural images (Fig. 6.6) are obvious by visual inspection and their corresponding LSRM image (Fig. 6.7) further supports the diagnosis. However, the difference between normal fat and WDLS cannot be confirmed by visual inspection of their corresponding OCT structural images (Fig. 6.8 (a) and 6.8 (b)). However, LSRM can provide critical intrinsic chemical composition information that would identify WLDS and normal fat. Figure 6.8 (c) presents the Raman spectra the normalized to 1440 cm^{-1} from WLDS (black) and normal fat sample (red). The Raman spectra shown here are averaged from 80 different locations and normalized to Raman bands at 1448 cm^{-1} (CH_2 bending). Broadening of 1655 cm^{-1} and decrease of 1655 cm^{-1} (C=C stretching) and

1734 cm^{-1} (C=O stretching) [123] in WDLS are observed. Although tissue Raman spectra are highly complex and typically requires advanced chemometrics [72, 73], we have obtained highly-distinguishable spectra from fat and WDLS. Thus, univariate statistical analyses are effective to quantify the difference between WDLS and normal fat tissue. The histogram of peak area under 1655 cm^{-1} is shown in Fig. 6.8 (d), where a threshold of 15.5 can separate WDLS from normal fat tissue, as indicated by a dashed orange line. Spectra with peak areas larger than 15.5 are identified as WDLS. The associated p-value is less than 0.01. We also use peak area under 1734 cm^{-1} to differentiate WDLS and normal fat, as shown in Fig. 6.8 (e), where a threshold of 1.28 can be used to separate WDLS and normal fat. Spectra with peak area of less than 1.28 are identified as WDLS with an associated p-value less than 0.01. In both statistical studies, all spectra are normalized to 1655 cm^{-1} band.

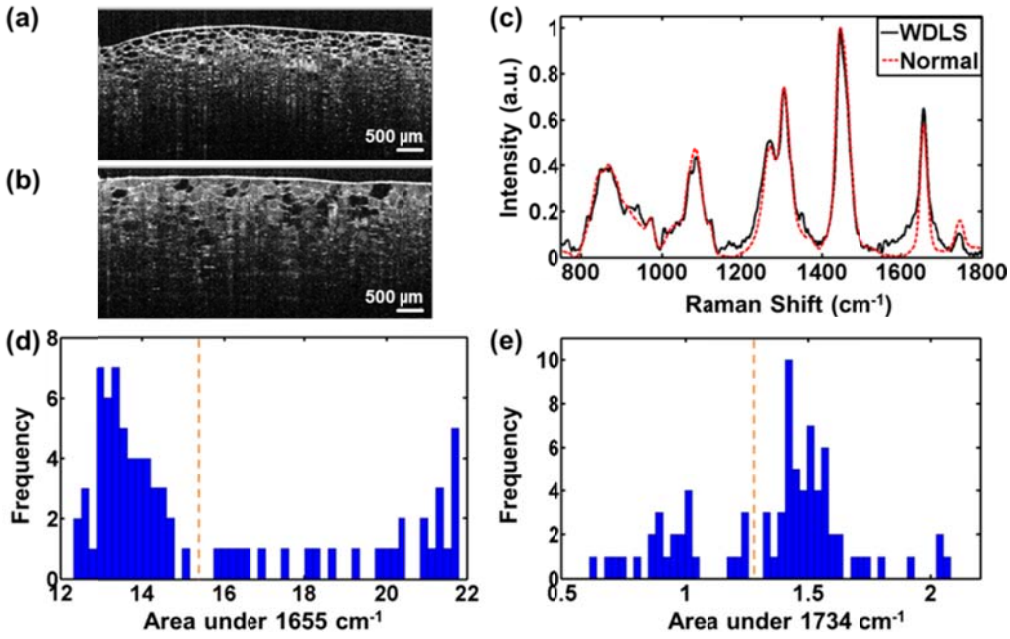

Figure 6.8 OCT images from normal fat tissue (a) and WDLS (b); (c) Raman spectra from normal fat tissue (red dotted) and WDLS (black); histogram of area under Raman bands at 1655 cm^{-1} (d) and 1734 cm^{-1} (e).

Similarly, there is no clear distinction between gastrointestinal sarcoma tumor (GIST) and Myxoma from their corresponding OCT structural images (Fig. 6.9 (a) and 6.9 (b)). However, Raman spectra acquired from GIST (red) and Myxoma (black) show different chemical features as shown in Fig. 6.9 (c). Both spectra are normalized to Raman bands at 1448 cm^{-1} (CH_2 bending). GIST shows a stronger band around 1000 cm^{-1} (CC aromatic ring breathing) [124]. Raman bands at 845 cm^{-1} (CCH aromatic deformation), 935 cm^{-1} (CCH deformation), 1028 cm^{-1} (CH stretching), 1261 cm^{-1} (Amide III) and 1302 cm^{-1} (Palmitic acid) are not observed in Myxoma [124]. Spectrum acquired from Myxoma also shows distinct features at 750 cm^{-1} (symmetric ring breathing), 774 cm^{-1} (ring vibration), 1254 cm^{-1} (CH_2 in plane) and 1340 cm^{-1} (CH_2 deformation) [124]. Both spectra show a 1:1 intensity ration of lipid bands at 1448 cm^{-1} and 1655cm^{-1} and a broadening at 1655 cm^{-1}. These distinct Raman features can effectively differentiate GIST from Myxoma.

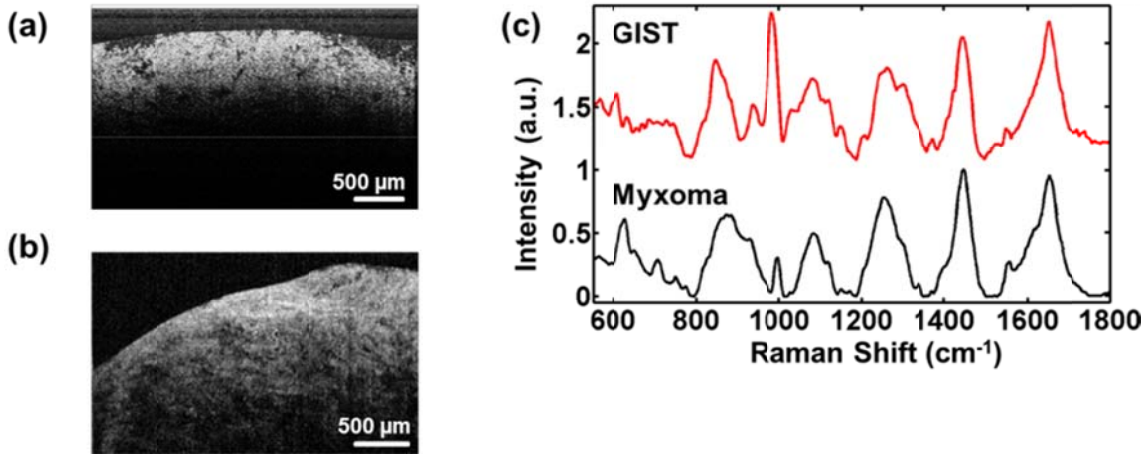

Figure 6.9 OCT images from Gastrointenstinal Sarcoma Tumor (a) and Myxoma (b); (c) Raman spectra from Myxoma (red) and GIST (black).

6.5 Conclusions

We have presented a tissue analysis and classification method using both the slope of OCT intensity signal versus depth and the principle components from the Raman spectrum as the indicators for tissue characterization. Compared to using OCT alone, the prediction accuracy has been improved from 84 % to 100 % by combination of two techniques on classification of mouse tissue. Therefore, the combined OCT/LSRM method is potentially useful as a noninvasive optical biopsy technique for rapid and automatic tissue characterization during surgery.

Combination of OCT and LSRM has also been demonstrated in cancer diagnosis and margin detection. OCT is preferable for real-time screening. In cases where OCT images are indistinguishable, for example, in normal fat and well differentiated liposarcoma (WDLS) or gastrointestinal sarcoma tumor (GIST) and Myxoma, distinct Raman spectra have been obtained. The results suggest LSRM can effectively complement OCT to tumor boundary demarcation with high specificity. In this study, the tissue samples were imaged on separate SDOCT and LSRM systems, but our future studies will focus on combining OCT and LSRM system into a single probe based system that can be used for real-time application during tumor resection surgeries.

Related Publication

"Improvement of tissue analysis and classification using Optical Coherence Tomography combined with Raman spectroscopy", C.-H. Liu, J. Qi, J. Lu, S. Wang, C. Wu, W.-C. Shih, and K. V. Larin, *Journal of Innovative Optical Health Sciences*, 2014, 140601175004007.

"Line-scan Raman microscopy complements optical coherence tomography for tumor boundary detection", N. Sudheendran, J. Qi, E. D. Yong, A. J. Lazar, D. C. Lev, R. E. Pollock, K. V. Larin and W. -C. Shih, (submitted).

Chapter 7 Morphological, Plasmonic, and SERS Characterization of DC-sputtered Gold Nanoislands

7.1 Introduction

Rapid chemical analysis of molecular adsorbates on plasmonic nanostructures is a powerful technique in molecular sensing and in the study of surface chemistry and plasmon-matter interactions. Due to either surface plasmon resonance (SPR) or localized surface plasmon resonance (LSPR), optical energy can be coupled into either propagating or non-propagating electron oscillation, respectively. Therefore, both SPR and LSPR can be conveniently investigated by extinction spectroscopy in the transmission configuration [125]. Besides optical extinction, plasmonic resonance also produces highly localized electromagnetic field enhancement near the surface of metallic nanostructures, which subsequently enhances fluorescence and Raman scattering of nearby surface adsorbates [41, 126]. Raman spectroscopy is a versatile technique for compositional analysis via inelastic light scattering due to molecular vibrations. It is particularly suitable for the study of thin surface adsorbates on plasmonic nanostructures via surface-enhanced Raman scattering (SERS) for its high sensitivity, specificity, and non-photobleaching property [127, 128].

Among various plasmonic nanostructures, metallic nanoislands have been studied as early as in the ‘80s [39-42]. Since 1997, the interest was shifted to Au for its potentially better structural and environmental stability. The SERS activity of gold nanoisland (GNI) fabricated by a slow deposition process was first observed by Maya [129]. Subsequently Rubinstein *et al*. carried out a series of studies on plasmonic properties of *evaporated* GNI which were shown to be “metastable” even at room

temperature [130-132]. Merlen *et al*. carried out a series of studies [133, 134] on *sputtered* GNI with significantly higher deposition rate compared to the work by Maya. They further employed GNI to analyze compounds such as dye molecules which exhibit resonance or pre-resonance effects near the absorption wavelength. More recently, GNI structures were employed in plasmon-enhanced catalysis for decomposition of methyl orange and splitting of water [135, 136]. It appears that sputtered GNI provides much better structural and environmental stability for practical applications. Therefore, we are interested in further characterizing its plasmonic properties for SERS applications.

In this Chapter, we provide multimodal characterization of GNI with respect to different deposition time. We correlate GNI morphological evolution imaged by scanning electron microscopy (SEM), LSPR spectra by extinction spectroscopy, and SERS spectra by hyperspectral Raman microscopy. We report systematic determination of the magnitude and spatial uniformity of SERS activity on GNI substrates. We also report, for the first time, a rigorous determination of the SERS enhancement factor (EF) for benzenethiol self-assembled monolayers, a commonly used marker for performance evaluation across various SERS substrates. Further, we demonstrate a parsimonious sampling scheme for large-area SERS mapping enabled by active-illumination Raman microscope described in Chapter 4 and Chapter 5. Finally, we compare image statistics obtained from parsimonious sampling to those from full-coverage sampling (LSRM).

7.2 Material and Methods

7.2.1 DC-sputtered GNI

GNIs were deposited on glass coverslip in a 2 inch DC-diode sputtering system (Anatech/Technics "Hummer") with a gold foil target of 99.99% purity. Sputtering

conditions were as follows: a) 10 mA current, 100 mTorr Ar pressure, and 25 mm target-to-substrate distance.

No. 1 coverslips (VWR Scientific Products) were first immersed in piranha solution (3:1 mixture of 98% H2SO4 and H2O2) for 30 minutes to remove any organic residue. The cleaned coverslips were then rinsed in DI water and blow-dried with nitrogen before sputtering.

7.2.2 Hyperspectral Raman Imaging Systems

We have employed two parallel, hyperspectral imaging systems, line-scan and active-illumination described in Chapter 3 and Chapter 4, respectively, to characterize the SERS EF and uniformity of GNI substrates.

7.2.3 UV-Vis Extinction Spectroscopy

A Cray 50 Scan UV-Visible spectrometer (Varian Inc.) was used to measure the UV-Vis spectra from 250 to 1100 nm. A spectrum from a clean coverslip was acquired as the reference and subtracted from raw data. The UV-Vis spectra presented below were averaged from five measurements.

7.2.4 Benzenethiol Self-assembled Monolayer

Benzenethiol (BT) was employed as the SERS marker for its ability to form a self-assembled monolayer (SAM) on gold. Briefly, we incubated the GNI substrates in 5 mM benzenethiol (99.9%, Sigma-Aldrich) dissolved in ethanol for 30 minutes, followed by rinse in pure ethanol for 1 minute and nitrogen dry [137]. Using benzenethiol SAM for the quantitative determination of SERS enhancement factor (EF) is advantageous because its surface density on gold is well known, thus enabling an accurate quantification of number of molecules. The choice of the laser wavelength (785 nm) avoids any resonant

or pre-resonant effect due to the weak absorption by BT molecules. SERS EF was estimated by comparing to normal Raman signals obtained from neat BT solutions. SERS EF was alternatively estimated by comparing to a commercial substrate (Klarite, Renishaw Diagnostics Ltd.) with a specification of 1million EF for BT.

7.3 Results and Discussion

7.3.1 Morphology Study of DC-sputtered GNI

The deposition rate of the sputtering machine was first calibrated by coating a gold layer on silicon for 300 sec. An SEM image of the cross-section showed that the thickness of the film was ~ 27 nm. Thus, the average deposition rate was determined to be 0.09 nm/sec. Since the GNIs are isolated units, it is not suitable to estimate thickness simply by multiplying the average rate with deposition time. Instead, we use the deposition time to distinguish our samples.

Figure 7.1 (a-e) show the SEM images of GNI substrates prepared by 52, 104, 156, 208, and 260 sec of deposition, respectively. We analyzed the size of the islands from the SEM images via ImageJ (NIH) by first trimming the SEM images to the same size and smoothed the image twice using a 3 × 3 moving average filter. We then binarized the images and performed watershed process to separate the connected objects to isolated particles. The processed images are shown in the inset of each image in Fig. 7.1 (a-e). Average radii of GNI measured in these images are shown in Fig. 7.1 (f) with each data set fitted by Gaussian distribution with μ = 3.36, 4.20, 4.95, 6.06 and 6.00, and σ = 0.90, 0.94, 1.20, 1.71, and 1.78, respectively. We observed an increase of GNI radius from 52 to 208 sec substrates. However, the growth of nanoisland size stopped after the 208 sec sample when additional fine structures began to form on existing nanoislands.

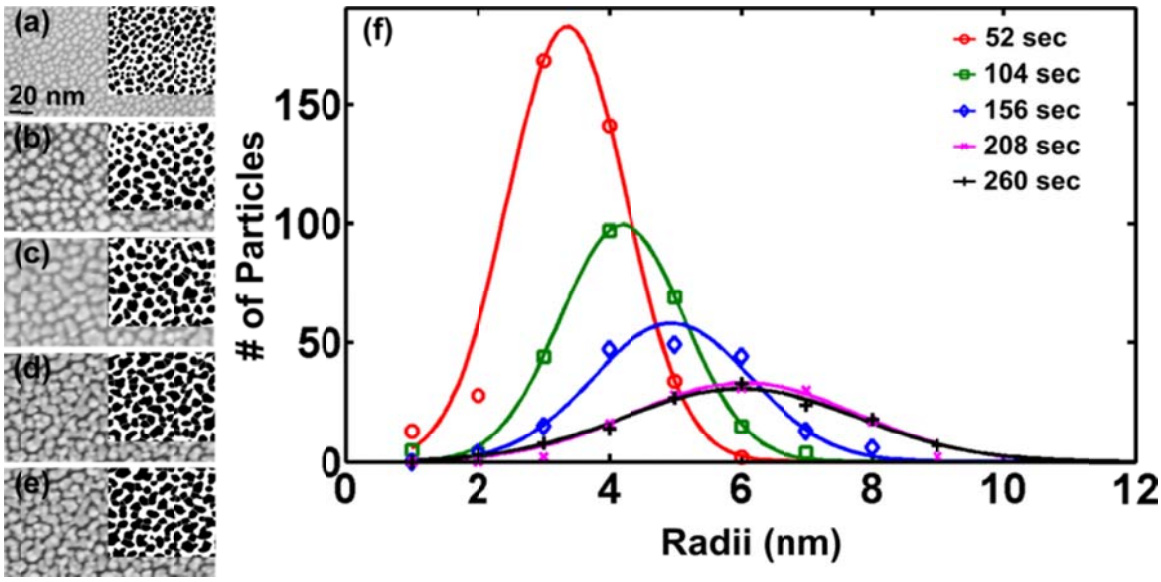

Figure 7.1 SEM images of GNI substrates with various deposition time: (a) 52 sec, (b) 104 sec, (c) 156 sec, (d) 208 sec, and (e) 260 sec; (f) corresponding GNI size distribution.

7.3.2 UV-Vis Extinction Spectroscopy

As shown in Fig. 7.2, we measured the UV-Vis spectra of GNI substrates in ambient environment of air (n = 1), water (n = 1.333), ethanol (n = 1.362) and toluene (n = 1.492). First of all, unlike in previous reports, our GNIs were stable in various solvents. One characteristic LSPR band ("*") was observed in all GNI samples in air, which shifted from 690 to 1100 nm as the deposition time increased (see Fig. 7.2 (a)). A new LSPR band ("x") at ~ 620 nm emerged after the deposition time reached 156 sec, and shifted to 660 nm in the 208 sec sample. Similar behavior was also found in extinction spectra measured in other media. However, 156 sec, 208 sec, and 260 sec samples showed a clearer band at ~ 650 nm in higher refractive index media, agreeing with the literature [138, 139]. This observation is consistent with the size analysis of nanoislands discussed earlier. The nanostructural changes due to size variations are reflected in the

plasmonic resonance. With a short sputtering time, the GNIs were small, and appeared isolated from each other. As the deposition time increased, these isolated islands grew and thus caused the LSPR band to redshift of from 690 nm to 1100 nm. The 156 sec sample entered a transition stage: as the deposition time further increased, the bases of the nanoislands began to coalesce, resulting in the new LSPR band. We also observed stronger extinction with increased deposition time, which might also contribute to a larger SERS EF besides the redshift.

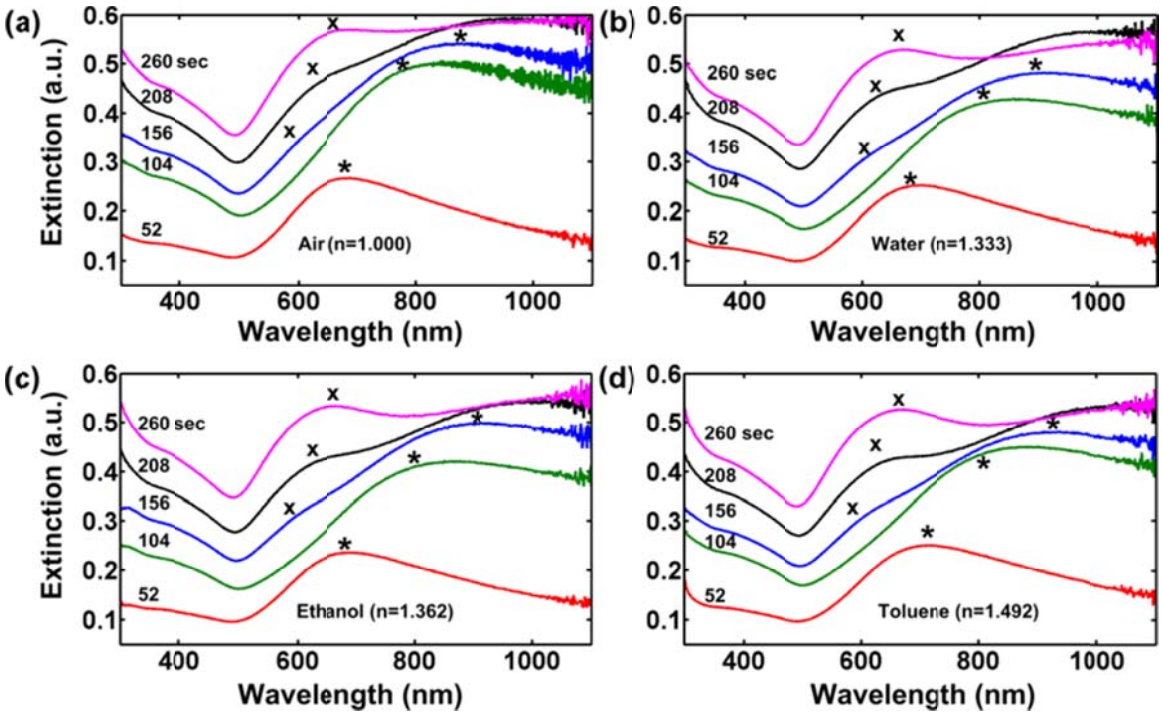

Figure 7.2 UV-Vis spectra of GNI of various deposition time in different refractive index media: (a) air, (b) water, (c) ethanol, and (d) toluene.

7.3.3 SERS EF of GNI Substrates

We have characterized the SERS enhancement of GNI substrates using the line-scan and active-illumination Raman systems. GNI substrates coated with benzenethiol SAM were mapped 10 to 20 times at random location across a 22 × 22 mm^2 area. The

average spectra over an area of six 100 × 100 μm^2 are presented in Fig. 7.3. Among the major SERS bands observed in all GNI substrates, we selected to study 1075 cm^{-1} (CCC stretch, CS bending) and 1575 cm^{-1} (CC stretching), as marked by asterisk and triangle, respectively. The inset figure shows the dependence of SERS intensity on the deposition time, exhibiting an upward increasing trend. The average SERS intensity of 260 sec GNI at 1075 cm^{-1} and 1575 cm^{-1} band were 50.7 and 54.5 times larger than that of 52 sec GNI, respectively. This implies the EF is very sensitive to GNI size. By comparing to the normal Raman intensity from neat benzenethiol, the EF was ~ 5.2 ×1 0^6. By comparing the 1575 cm^{-1} band from 260 sec GNI and Klarite, we obtained an average of 2.2 times larger SERS intensity from GNI. Since the EF of Klarite is specified at least 1.0 × 10^6 for benzenethiol SAM, the EF of 260 sec GNI was at least ~ 2.2 × 10^6, in-line with the other value.

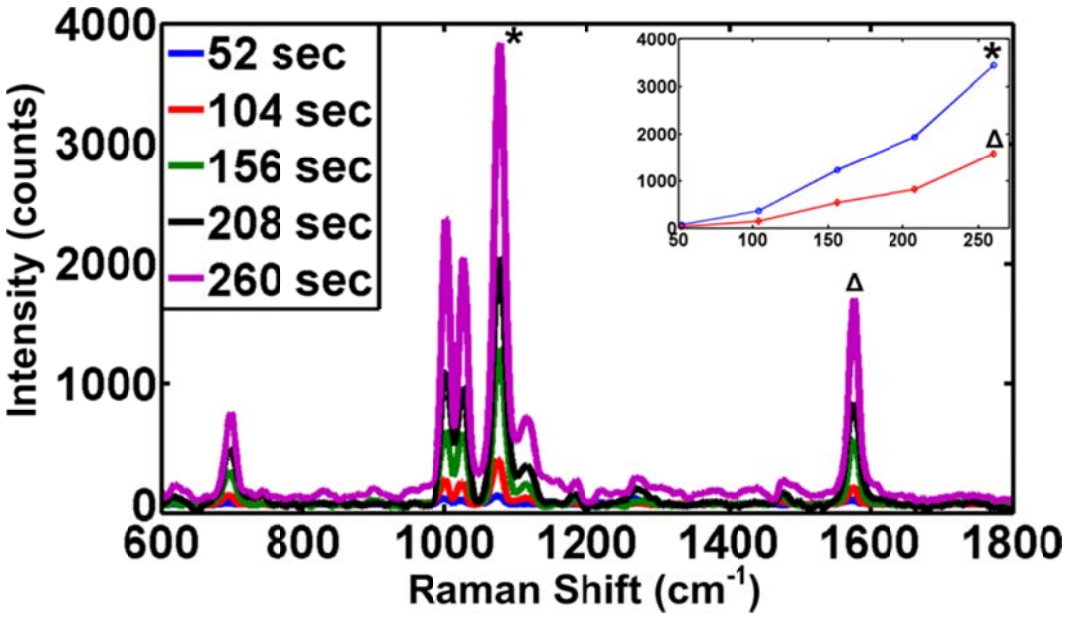

Figure 7.3 SERS spectra of benzenethiol SAM coated GNI substrates and dependence of SERS intensity on deposition time in the inset.

7.3.4 Characterization of SERS Uniformity Using Hyperspectral Raman Imaging

Confocal Raman microscope has been used to characterize the uniformity of plasmonic substrates [140, 141]. An alternative strategy to improve imaging speed is to employ parallel acquisition to obtain hyperspectral data, i.e., images consisting of both a spatial and a spectral dimension, e.g., (x, y, λ) in each camera shot. In Raman microscopy, parallelism has been implemented by global illumination [29, 142], line-scan [6, 7, 30], and active-illumination [90, 121, 143]. Global illumination uses tunable narrow-band filters and wide-field image collection to acquire a Raman map by sequentially scanning through multiple wavelengths. This is very time-consuming because out-of-band Raman photons are blocked by the filter in each scanning step. Moreover, global illumination does not allow the acquisition of hyperspectral data in a single camera shot, rather, it is limited to a "narrow band" image. In contrast, line-scan and active-illumination are truly parallel, hyperspectral acquisition schemes with substantial throughput advantages. In a typical line-scan system, the laser is shaped into a long line and focused onto the sample while the entire line is imaged to the spectrograph entrance slit. Thus, spatially-resolved spectra along the entire line can be recorded in a single camera snapshot. An active-illumination system, however, splits the laser into a semi-arbitrary pattern of micro-spots at the sample and collects the Raman spectra from all spots simultaneously in a single camera snapshot. An important advantage of active illumination over the line-scan approach is that semi-random parsimonious sampling in a two-dimentional plane can be employed to construct unbiased, representative statistics efficiently.

Here we have employed the active-illumination system to characterize SERS uniformity on the 208 sec GNI substrate. Each illumination pattern contained 62 laser

spots with randomly selected spatial positions. A reference measurement from silicon wafer was recorded for intensity calibration of each pattern. Figure 7.4 (a-e) show hyperspectral images acquired using five illumination patterns with background removed by a 5th order polynomial and intensity calibration [121, 144]. Figure 7.4 (f) shows the average SERS spectrum (red curve) with ± 1 standard deviation (gray shade). Similar data collected by the line-scan system are also presented in Fig. 7.4 (f), indicating the same major SERS bands and peak ratios were obtained by the active-illumination and line-scan systems. The overall mean and standard deviation of the SERS intensity from the 310 spots in 5 illumination patterns were $8.08 \times 10^4 \pm 6.26\%$, which agree well with those obtained from the line-scan system ($7.86 \times 10^4 \pm 5.92\%$). The comparison suggests that parsimonious semi-random sampling of only ~ 2.7% sample area can captures unbiased, representative statistics similar to those obtained by 100% sampling. Therefore, the sparse-sampling scheme can provide a highly efficient way to collect data from SERS substrates for the extraction of representative statistics.

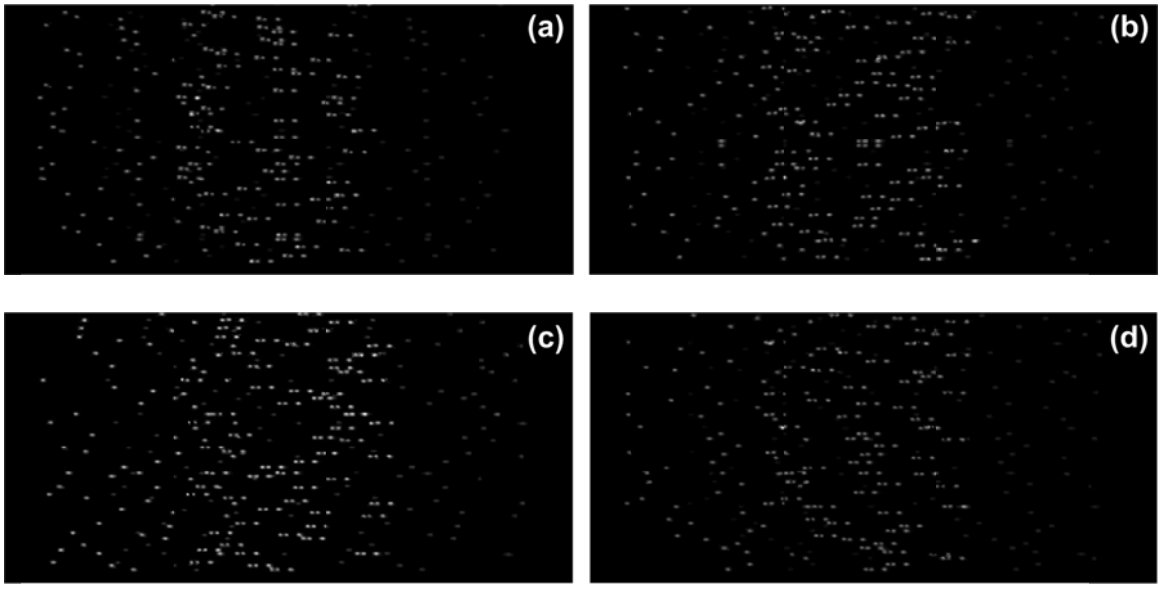

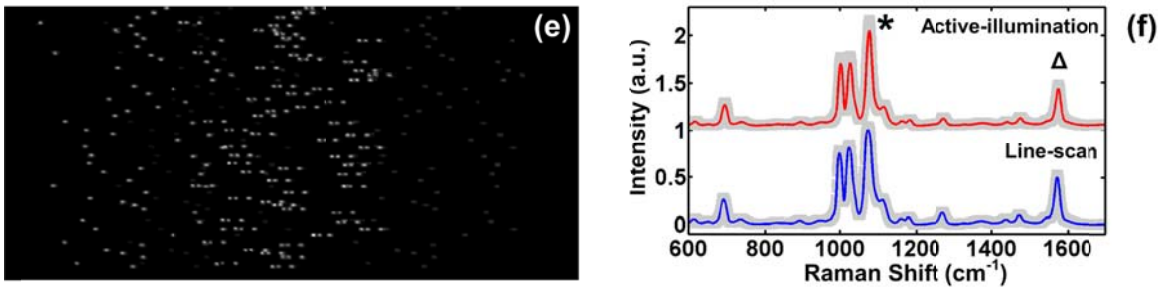

Figure 7.4 Hyperspectral SERS images and spectra: (a-e) Raw CCD images acquired using individual illumination patterns; (f) average SERS spectra from the active- illumination system and line-scan system with ±1 standard deviation (gray shade).

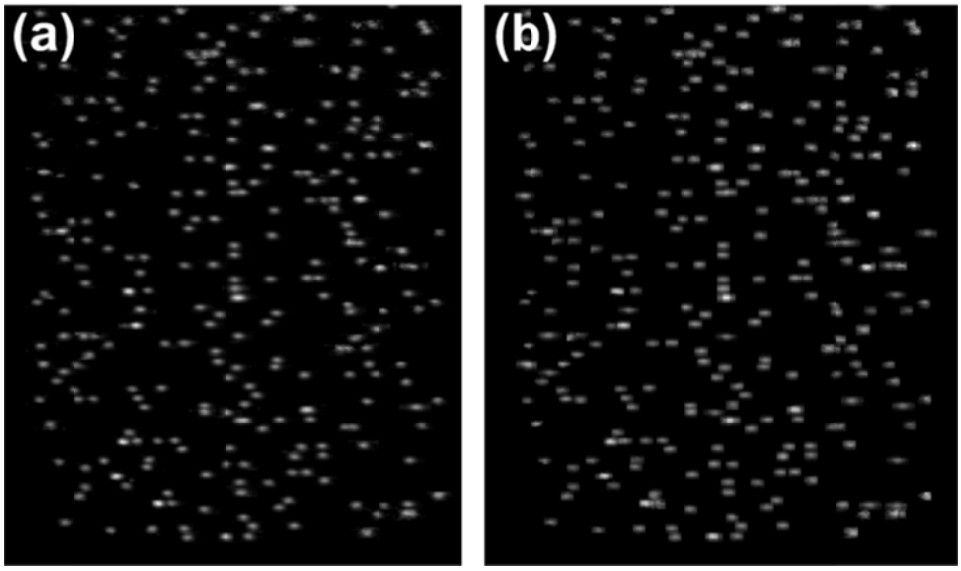

Figure 7.5 7.5 SERS maps of benzenethiol SAM using two peaks: (a) 1075 cm^{-1} and (b) 1575 cm^{-1}.

SERS maps are generated using the BT SERS bands at ~ 1075 cm^{-1} and ~ 1575 cm^{-1}, as shown in Fig. 7.5 (a) and 7.5 (b), respectively, based on a total of 310 spots that corresponding to ~ 2.7% fill-factor of the total field of view. The mean and standard deviation of SERS intensities measured from each illumination pattern was 7.60×10^4 ±

6.72%, $8.41 \times 10^4 \pm 4.11\%$, $8.11 \times 10^4 \pm 6.62\%$, $8.46 \times 10^4 \pm 7.75\%$ and $7.82 \times 10^4 \pm$ 6.12%.

7.4 Conclusion

In summary, we have demonstrated DC-sputtered gold nanoislands provide a low-cost, uniform SERS substrate with an enhancement factor comparable to commercial substrates. By correlating SEM, extinction spectroscopy, and SERS microscopy, GNI's plasmonic behavior has been investigated with respect to morphological changes as deposition time increased, as well as ambient environmental changes. The UV-VIS extinction spectra showed a stronger extinction for GNI samples prepared by longer deposition time. SERS performance has been characterized using benzenethiol self-assembled monolayer as the marker. The enhancement factor of GNIs increased with deposition time and the value for 260 sec was $\sim 5.2 \times 10^6$. Large-area SERS uniformity has been evaluated by two hyperspectral Raman imaging systems, active-illumination and line-scan, over randomly selected locations. The overall SERS intensity statistics were $8.08 \times 10^4 \pm 6.26\%$ and $7.86 \times 104 \pm 5.92\%$ using the active-illumination and the line-scan systems, respectively. The results suggest our parsimonious sampling scheme using active-illumination can obtain representative, unbiased statistics even when the total sampling area is only 2.7% of the entire field of view.

Related Publication

"Morphological, plasmonic, and SERS characterization of DC-sputtered gold nanoislands", J. Qi, S. –T. Lin, P. Motwani, J. Zeng, J. C. Wolfe and W. C. Shih, 2014 (submitted).

Chapter 8 Surface-enhanced Raman Spectroscopy with Monolithic Nanoporous Gold Disk Substrates

8.1 Introduction

In Chapter 3 - 5, effort has been made to improve the throughput of the Raman instrumentation significantly. However, the intrinsic limitation of Raman scattering has not been broken through. Consequently, SERS is employed in order to achieve more throughput and sensitivity. As mentioned in Chapter 2, although SERS provides 10^6 to 10^{14} signal enhancement, challenges on SERS substrates hinder further application of this technique. Plasmonic substrates with high EFs, uniformity, reproducibility and stability are desired.

SERS has been widely applied to molecular detection and identification [145-147]. The technique derives its sensitivity from electrical field amplification by localized surface plasmon resonance (LSPR), strongest at SERS hot-spots associated with nanoscale gaps, and protrusions [148]. These observations have sparked intense interest in nanoporous gold (NPG) as SERS substrates, where porosities and pore diameters in ranges of 35-50 % and 5-10 nm, respectively, have been reported [149-152]. An additional potential benefit is that internally adsorbed molecules and those that may be traversing the nanoporous network can also participate in Raman scattering [148]. Another potential advantage of NPG over non-monolithic SERS substrates, such as immobilized or aggregated nanoparticles, is the simplicity by which it can be integrated with sensor chip technology. It has been shown that the LSPR peak of NPG thin films exhibits a pore-size dependent red-shift [153, 154]. Although SERS activity has been documented, wide variations in SERS enhancement factors (EFs) have been reported

[149, 150, 152]; possibly reflecting differences in material composition and morphology, fabrication technique, SERS marker, and/or excitation wavelength. Several groups have explored the increase in EF due to further processing of the NPG films; Zhang *et al.* observed a ~ 100-fold increase in EF caused by wrinkling the substrate of an NPG film, an approach that suffers from very wide site-to-site EF variation [47]. Jiao *et al.* also achieved a ~ 100-fold EF increase in mechanically stamped NPG gratings, which they attributed to the combined effect of improved light-coupling by the grating structure and mechanical densification [155]. Wi e*t al.* reported a five-fold increase in the SERS signal from NPG disk substrates compared to solid gold disks [156], which are known to produce a SERS EF of 1000 - 10000 [157, 158]. In their work, NPGDs were formed by dealloying co-sputtered gold and copper targets and patterned using electron-beam lithography. The disks were ~ 200 nm in diameter and 80 nm in thickness.

In this Chapter, we explore further the effect of patterning on the SERS EF of NPG using disk-shaped structures (NPGD). Our approach features hybrid fabrication by combining top-down planar large-area sputter etching and bottom-up atomic self-assembly during dealloying. The resulted structure is thus hierarchical with the external disk shape and the internal porous network. We have selected 785 nm as the laser excitation wavelength and benzenethiol (BT) molecules as the SERS marker since the absence of a BT absorption peak near 785 nm minimizes the ambiguity presented by resonant Raman scattering, while the ability of BT to form self-assembled monolayers (SAMs) enables the number of molecules on individual NPG disks to be quantified. Additionally, the SERS activity at 785 nm laser excitation has critical significance for deep tissue penetration in any potential biomedical applications.

8.2 Fabrication of NPGD

The NPGD fabrication process is shown in Fig. 8.1. First, a 300 nm thick gold layer is sputter-deposited on a silicon wafer followed by a 75 nm Au/Ag alloy film using DC-magnetron with a 25 mm source (Lesker). The gold film was deposited using a 99.99 % pure gold target (Royal Canadian Mint). The Au/Ag alloy film was deposited using an alloy target with Au:Ag ratio of 28:72 (ACI Alloys). The Ar sputtering pressure and power were 5 mTorr and 50 W, respectively. A magnetic virtual anode, adapted from the cylindrical magnetron, was used to prevent electron bombardment of the growing film. The deposition rates for the gold and the alloy films were 37.5 nm/min and 25 nm/min, respectively.

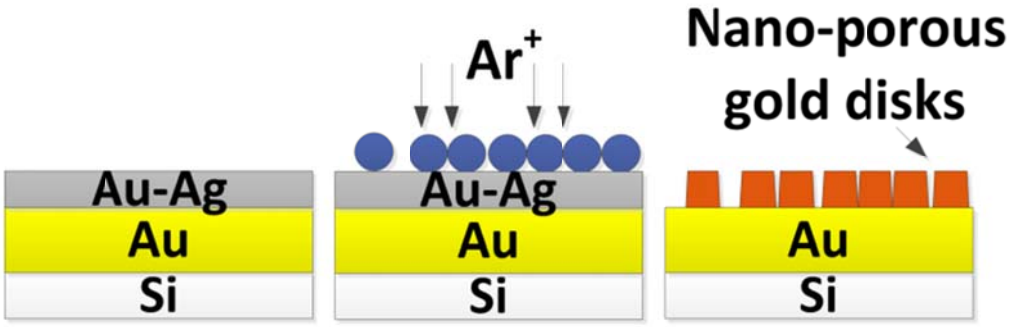

Figure 8.1 Fabrication process flow: (a) Au/Ag and Au film stack on silicon substrate; (b) Au/Ag by Ar+ sputter etching using drop-coated PS beads as a mask; (c) removal of PS beads and free corrosion in nitric acid to form nanoporous gold discs.

Next, 500 nm polystyrene (PS) beads (Polysciences, Inc.) are drop-coated onto the alloy film, followed by RF-sputter etching using the PS beads as an etch mask. Sputter-etching was carried out in a homemade reactor with a 150 mm cathode using 99.999% pure argon gas. The power density and argon gas pressure were 0.057 W/cm^2 and 2 mTorr, respectively. The etch rate of the alloy film was calibrated by scanning

electron microscopy to be ~30 nm/min. The etching step produces completely isolated alloy disks sitting on ~65 nm thick solid gold bases with a remaining underlying gold film ~235 nm thick (Fig. 8.2 (a)). The PS spheres are then removed by solvent and sonication. Finally, NPG is formed selective dissolution of the silver using a 1 sec dip in 70% nitric acid followed by deionized water rinse and nitrogen dry.

Figure 8.2 (a) shows the scanning electron micrograph (SEM) of the PS bead residues covering an etched alloy and gold film stack to confirm the thickness and the effectiveness of PS beads as the etch mask. The boundary between the alloy and gold base is visible in the high magnification image of Fig. 8.2 (b). The top surface of NPGD is revealed after the removal of the PS beads and nitric acid corrosion as shown in Fig. 8.2 (c). The NPGDs are ringed by a gold film which is redeposited during sputter etching of the base layer after the alloy discs are defined. These rings are not affected by HNO_3 etch. The ultra-fine nanoporous network inside the disk is similar to that obtained in unpatterned NPG thin films (Fig. 8.2 (d)) fabricated by the same dealloying procedure. The cracks caused by shrinkage during Ag dissolution are quite similar as well [159].

8.3 Determination EF of NPGD

Benzenethiol SAMs were deposited on unpatterned NPG, NPGD, and Klarite (SERS EF at least 10^6 for benzenethiol, Renishaw) substrates following the procedure described in Chapter 7, section 7.2.4. SERS measurements were carried out with 785 nm excitation using the home-built line-scan Raman microscopy system (LSRM) enabling SERS mapping over 133 × 133 μm^2 regions with ~ 1 μm^2 resolution (full width at half maximum, FWHM) at a spectral resolution ~ 8 cm^{-1}.

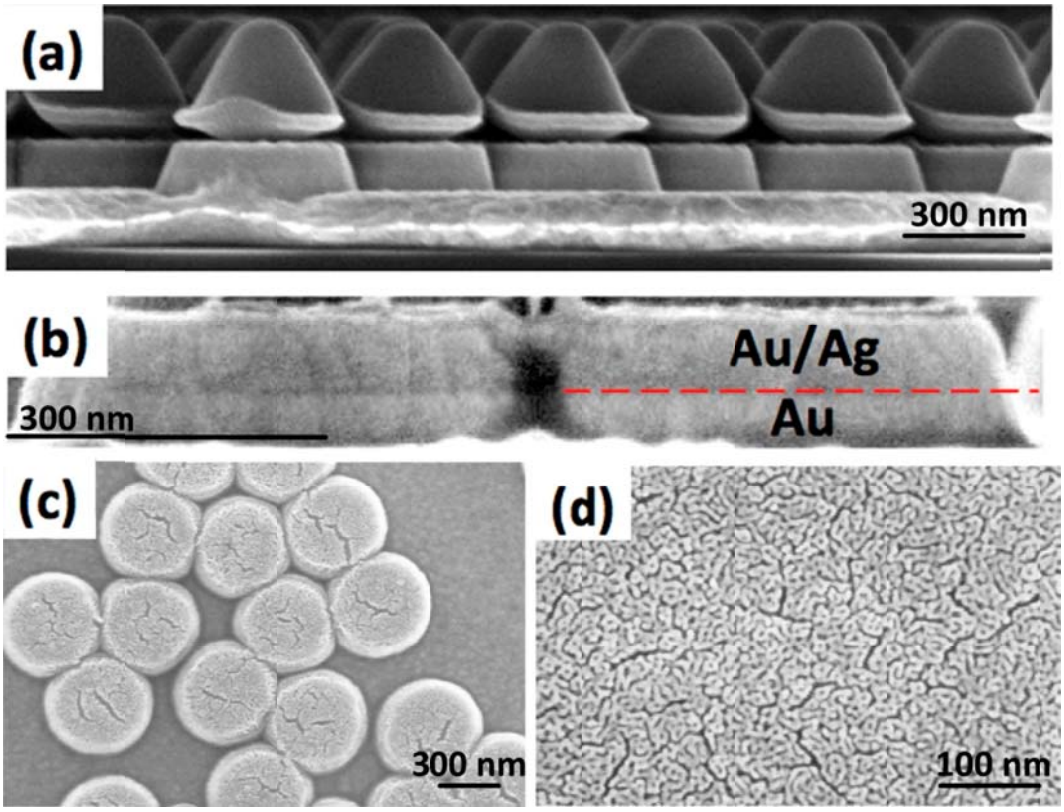

Figure 8.2 NPGD fabrication: (a) etched Au/Ag alloy disks on Au bases; (b) side view of alloy disks to show visible boundary between Au/Ag alloy and the Au base; (c) NPGD topview; (d) unpatterned NPG thin film.

Figure 8.3 shows the SERS spectra in CCD count rate (CR), normalized to laser power and the area of the laser spot, for BT SAMs on NPGD, NPG, and Klarite substrates, as well as the normal Raman spectrum obtained from neat benzenethiol solution. (The curves are offset for clarity.) The CR for NPGD substrates is 517 times larger than for unpatterned NPG and 396 times larger than for Klarite. Since the nanoporous structure and thickness are identical for the NPGD and unpatterned NPG substrates, including the density and average size of the cracks, the patterning process has produced a 517-fold increase in enhancement factor. The interpretation of the increased Raman scattering of the NPGD versus Klarite substrate requires an estimate of the total

number of BT molecules attached to a disk and how many of those are close enough to the surface to contribute to the measured photons.

The number of adsorbed BT molecules in and on an NPG disk is the product of the area of the disk, the roughness R of NPG (the ratio of the chemically active surface area to the geometrical surface area), and the BT surface density. Seker *et al.* developed a procedure for estimating the roughness of an NPG film from SEM images of the surface, assuming uniform nanostructure through the film [160]. In Ref. 160, equation 3 implies that roughness is given by 3hβ/r, where h, β, and r are the thickness, two-dimensional porosity, and mean pore radius, respectively. An analysis of Fig. 8.2, using ImageJ (http://rsbweb.nih.gov/ij/), gives β = 34 % and r = 3.5 nm, implying that the roughness is 22. Scanlon *et al.* reported electrochemically-measured roughness values in this range for 100 nm thick films with similar nanostructure [161]. The roughness of Klarite is about 1.6 because of the increased surface area of the anisotropically etched pits.

The contribution of adsorbed molecules to the total SERS signals decreases with depth because of the decreasing laser power density and increased absorption of the Raman-scattered light. The contribution dR' of an NPG layer of thickness dt at depth h to Raman scattering is characterized by a roughness$dR' = R/h \times \exp(-2t/\alpha_{NPG}) \times dt$. Integration gives the effective roughness of the NPG taking into account the round-trip absorption; $R' = R \times \alpha_{NPG}/2h \times [1 - \exp(-2t/\alpha_{NPG})]$ where $\alpha_{NPG} = \alpha_{Au}/f_{Au}$ is the skin-depth of NPG, α_{NPG} is the skin depth of gold (~ 12.6 nm [162]), and f_{Au} is the mole fraction of Au in the Au/Ag alloy. We find that $R' = 6.3$ and $\alpha_{NPG} = 45$ nm. Following Ref. 155, we have $EF_{NPGD}/EF_{Klarite} = (CR_{NPGD}/R'_{NPGD}) \times (CR_{Klarite}/R_{Klarite})$,

where the subscripts correspond to EF, CR, R, and R' of NPGD and Klarite. If the EF of Klarite is assumed as 1.0×10^6, although it is specified as *at least* according to the data sheet, the SERS enhancement factors calculated for 1076 cm^{-1} and 1575 cm^{-1} of NPGD substrates are 1.05×10^8 and 1.43×10^8 while those of unpatterned NPG film are 2.03×10^5 and 2.47×10^5, respectively (Table 8.1). We note that additional factors such as volumetric shrinkage may result in a slightly smaller R′, and consequently a slightly larger EF, but it is not considered here because there is no obvious shrinkage in our SEM images before and after dealloying.

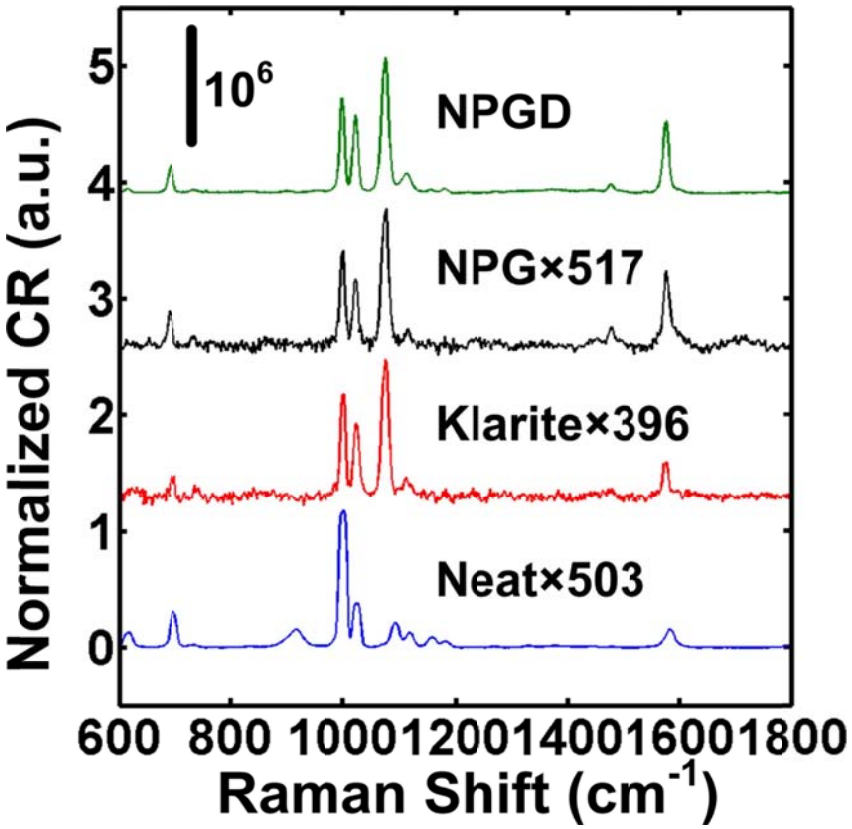

Figure 8.3 Normalized count rate (CR) from NPGD, unpatterned NPG, Klarite, and neat benzenethiol vs. Raman shift (cm^{-1}).

Alternatively, SERS enhancement factor can be obtained by comparing the SERS measurement to that from a neat benzenethiol sample, where the EF value is calculated by comparing the 1575 cm^{-1} peak in the SERS spectrum to the 1584 cm^{-1} peak in neat Raman spectrum [163]. When the SERS and normal Raman spectra are measured by the same instrument, the SERS EF is given by $EF = (I_{SERS}/I_{neat}) \times (N_{neat}/N_{SERS})$, where I_{SERS} and I_{neat} represent the normalized count rates of the SERS spectra from a single disk and normal Raman signal from a neat solution, respectively. N_{SERS} and N_{neat} are the number of molecules contributing to the SERS and neat Raman spectra, respectively. As discussed before, the surface area of NPGD is 6.3 times larger than its geometrical area. Assuming a packing density of 6.8×10^{18} molecules/m^2, approximately 8.4×10^6 molecules are adsorbed on a single disk. Therefore, the normalized count rate of the 1575 cm^{-1} peak from five NPG disks (which have a total area of ~ 1 μm^2) is 6.5×10^5 photons·$s^{-1}mW^{-1}$ (I_{SERS}; See Fig. 8.2), and is contributed by $5 \times 8.4 \times 10^6 = 4.2 \times 10^7$ molecules (N_{SERS}).

To obtain I_{neat} and N_{neat}, we performed two experiments with different ways to determine the optical probing depth. The optical probing volume was then calculated using the Gaussian beam with a 1.2 μm beam waist. In method 1, the depth of focus of our Raman instrument was experimentally characterized to be ~ 4.5 μm [164], and then used as the probing depth. In method 2, a sparse monolayer of 3 μm polystyrene beads were sandwiched between two glass coverslips, squeezed and fixed. A drop of 2 μL neat benzenethiol was then dispensed and drawn into the gap between the 25 mm × 25 mm coverslips by capillary force. Based on the spreading area of the solution, the average thickness of benzenethiol was calculated to be ~ 3 μm. Table 8.2 lists the optical probing

depth, probing volume, number of benzenethiol molecules (N_{neat}), normalized count rate of the 1584 cm^{-1} peak in the normal Raman spectra (I_{neat}, See Fig. 8.3), and enhancement factor (EF) from each method. The lowest EF value is slightly larger than the result obtained previously by assuming that Klarite has an enhancement factor of 1 million. We note again that Klarite is specified as *at least* 1 million.

Since there is no modification to the nanoporous network from our patterning technique, the EF increase is entirely due to the disk formation. A heuristic explanation to the substantial EF increase is a red shift of the plasmonic resonance peak toward the laser excitation wavelength (785 nm) by patterning into sub-micron disk [157, 158]. This is supported by known red-shifted plasmonic resonance peak in solid gold disks. Thus, it is plausible that plasmonic coupling between the external disk shape and the internal nanoporous network has contributed the high EF. Nevertheless, future work is needed to further unravel the interplay between the external shape and the internal network, as well as the identification of potential effects due to hot spot formation.

Table 8.1 SERS EF estimation using Klarite at 785 nm excitation.

	Klarite	**NPGD**	**NPG film**
EF of 1076 cm^{-1}	1×10^{6}	1.05×10^{8}	2.03×10^{5}
EF of 1575 cm^{-1}	1×10^{6}	1.43×10^{8}	2.47×10^{5}

Table 8.2 SERS EF estimation using neat solutions at 785 nm excitation.

	Probing Depth (μm)	**Probing Volume (μm^3)**	**N_{neat} (molecules)**	**I_{neat} (photons·s^{-1} mW^{-1})**	**EF**
Method 1	4.5	1025.3	6.0×10^{12}	310.8	2.9×10^{8}
Method 2	3	585.1	3.4×10^{12}	97.7	5.2×10^{8}

8.4 Characterization of Enhancement Uniformity

Figures 8.4 – 8.6 show line-scan SERS, bright-field optical, and scanning electron microscope images of the same region on a NPGD sample, respectively. The SERS map was generated using the peak at ~1076 cm^{-1} (CCC stretch, CS bending) as shown in Fig. 8.3. Clearly, SERS signal is maximum on the disks. The disks appear larger in the SERS map due to the limited resolution of the line-scan Raman system. Thus, given the spatial resolution of ~1 μm, the pixel intensity of Fig. 8.4 is contributed by ~ five NPGDs for densely populated regions and from one NPGD for isolated disks. We have verified that the intensity is proportional to the number of disks. The Raman count rates from different locations marked by boxes in Fig. 8.4 are shown in Fig. 8.7. The standard deviation of the normalized count rate obtained from individual disks within 6 areas is ±32%, signifying a decent disk-to-disk uniformity. We note that the pattern uniformity can be much improved by nanosphere lithography [165] or electron-beam lithography, but is not the focus of this study. We have performed large-area SERS mapping on several other regions on the NPGD samples and obtained similar results as shown in Fig. 8.8.

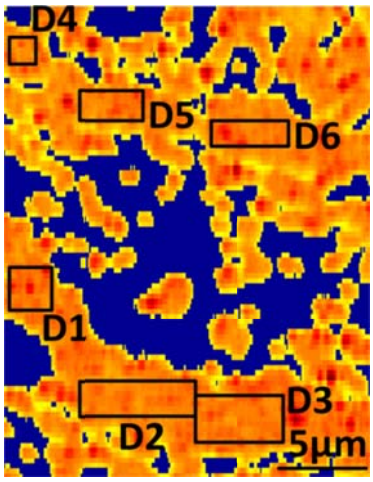

Figure 8.4 SERS map of NPGDs obtained by the line-scan Raman system.

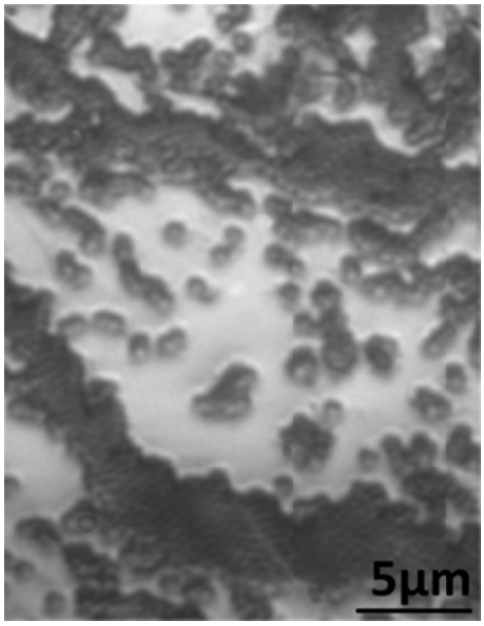

Figure 8.5 Bright-field image of NPGDs from the same region as in Fig. 8.4.

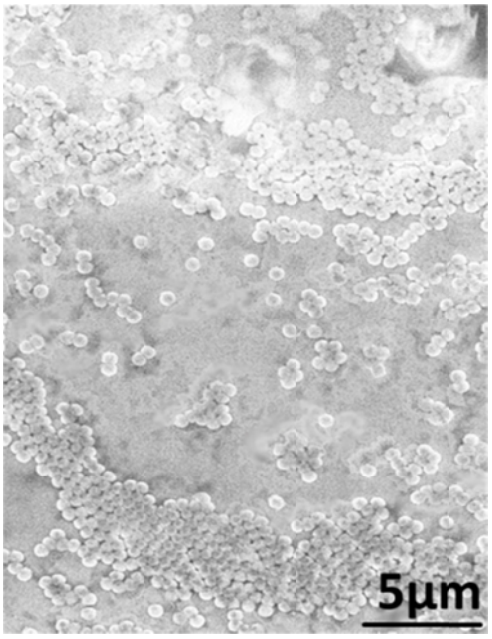

Figure 8.6 SEM image of NPGDs from the same region as in Fig. 8.4.

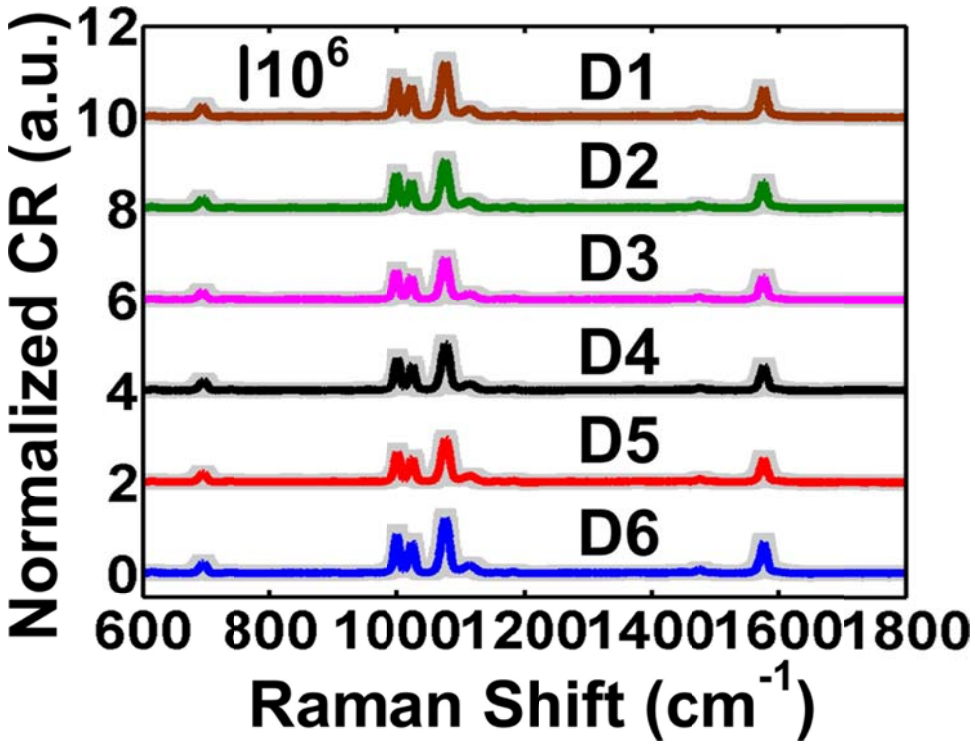

Figure 8.7 Mean SERS spectra and ±1 standard deviation (in grey shade) of BT SAMs obtained from 6 areas marked in Fig. 8.4.

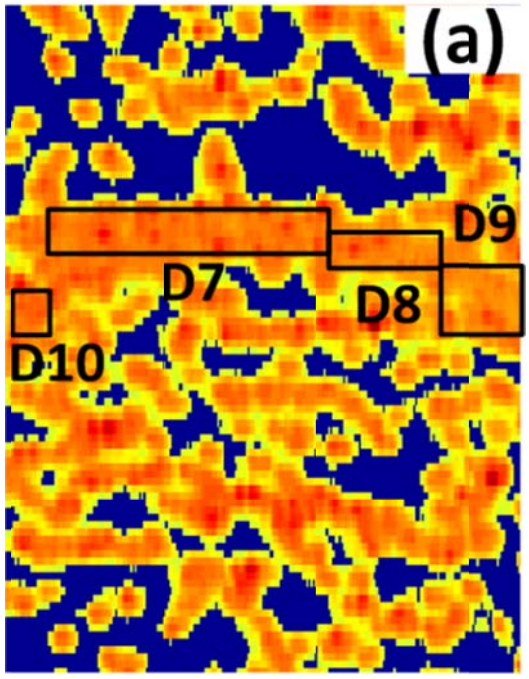

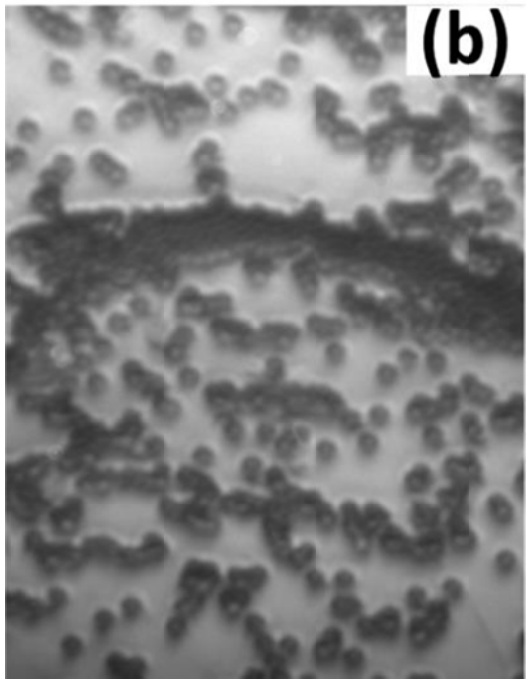
(b)

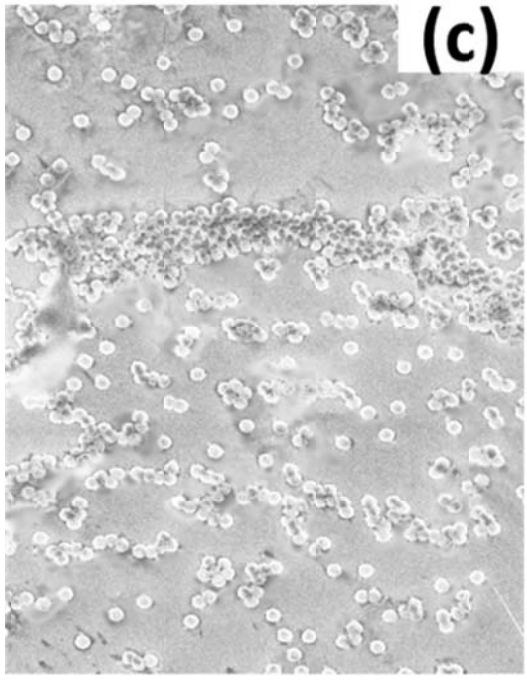
(c)

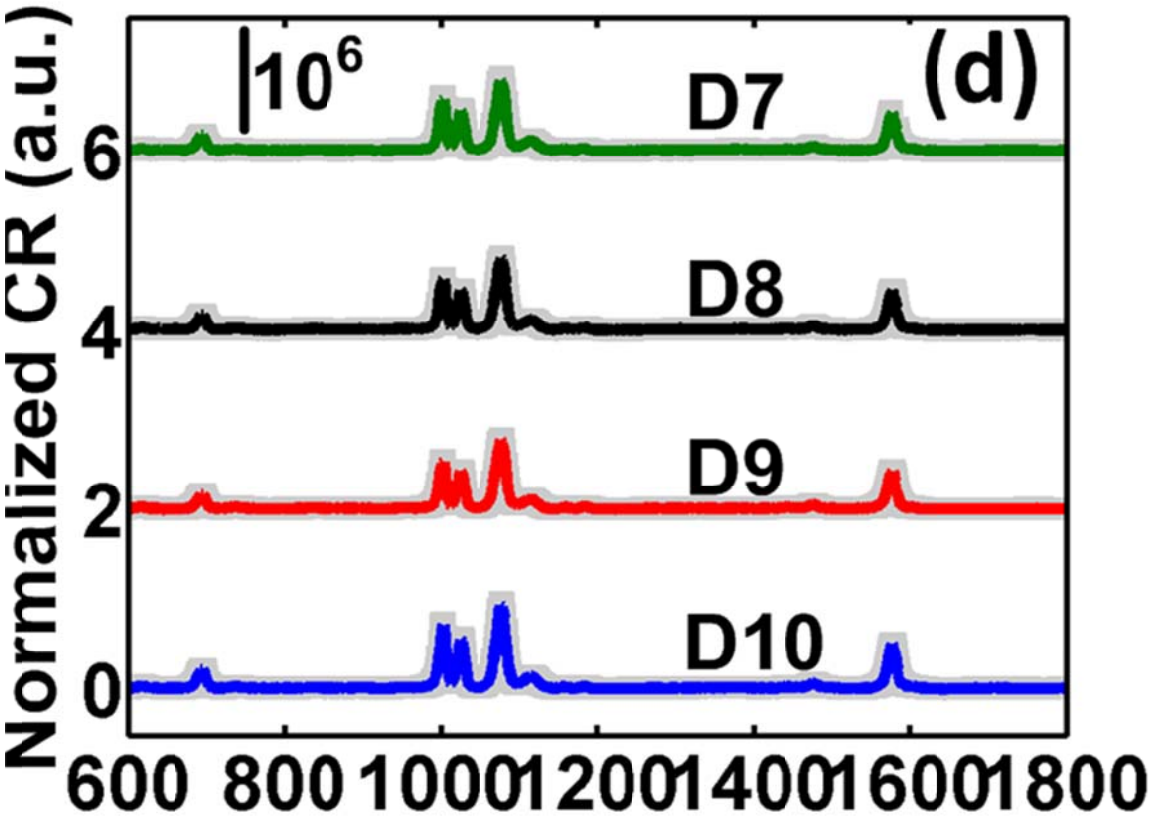

Figure 8.8 (a) SERS map of NPGD by the line-scan Raman system; (b) visual image and (c) SEM image; (d) average spectra with ± 1 standard deviation in gray shadows from 4 different locations shown in (a).

8.5 Detection Limit of NPGD

Given that the BT surface density on gold reported in the literature is 6.8 × 10^{14}/cm^2, the number of BT molecules on a single NPGD is ~ 14 attomoles. Since the signal-to-noise ratio (SNR) for NPGD is ~ 400 in Fig. 8.3, the detection limit is estimated to be ~ 22,100 BT molecules or 114 zeptomoles (SNR = 3) with 170 μW/μm^2 laser power density and 2-sec charge coupled device (CCD) integration time (Princeton BR400).

To demonstrate NPGD's potential in fast detection of trace molecular amounts, we have performed a series of experiments by varying the CCD integration time. In Fig.

8.9 (a), we show the results with integration time from 1 sec to 25 msec. The SNR (dB) vs. integration time is plotted in the inset of Fig. 8.9 (a), suggesting that a single NPGD coated with BT SAM can be detected with an SNR ~ 13 dB in 25 msec (the shortest integration time allowable in our system). The laser power density was 170 $\mu W/\mu m^2$.

All the previous results were obtained using a CCD cooled down to -70 °C. Next, we explore the detection capability of a single NPGD with various CCD temperatures with results shown in Fig. 8.9 (b). The SNR vs. CCD temperature is plotted in the inset of Fig. 8.9 (b), suggesting NPGD can be detected with SNR ~ 14 dB at CCD temperature as high as 25 °C. The laser power density was 1.7 $mW/\mu m^2$ and the integration time was 1 sec.

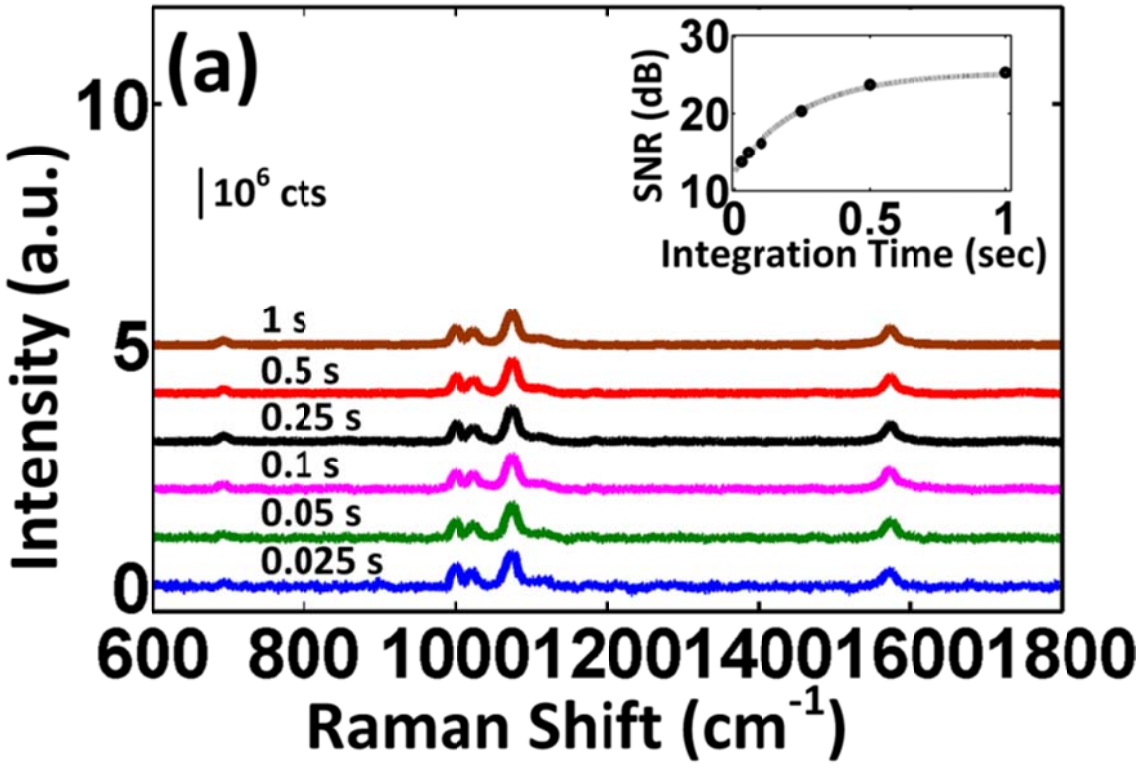

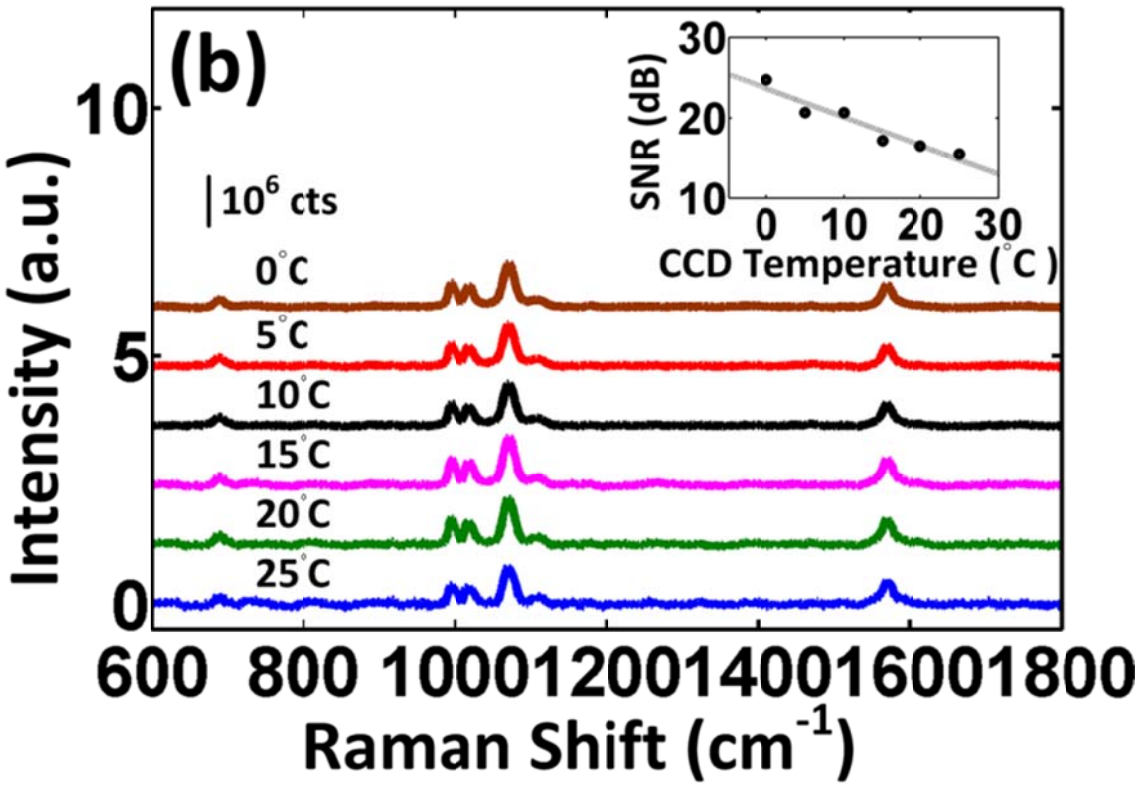

Figure 8.9 Normalized count rate (CR) and SNR from a single NPGD vs. CCD integration times (a) and CCD temperatures (b).

8.6 Stamping SERS for Label-free, Multiplexed, Molecular Sensing and Imaging Using NPGD

8.6.1 Motivation

SERS has been widely used in label-free molecular sensing and imaging. However, the practical use of SERS has often encountered a couple of inherent issues. The first one is regarding a molecule transfer step where target molecules need to be within the close proximity of a SERS surface by either mixing with nanoparticles or coating onto surface-bound nanostructures. In other words, target molecules are required to be transferred from non-SERS-active surfaces to SERS-active ones, normally in the solution phase, which can be problematic due to issues such as surface affinity variability

and uncertainty, competitive adsorption among different molecules, and contamination issues, causing irreproducible results and erroneous or biased interpretations. More importantly, if the spatial distribution of molecules on the surface prior to the transfer step is of importance, such information is completely lost. Practically, solution-phase processes are relatively more labor and time-consuming and require a "wet" laboratory. Furthermore, SERS measurements are always restricted to molecules adsorbed on metals such as Ag, Au, and Cu.

Consequently, we have developed a dry physical approach with decent sensitivity and SERS uniformity using a polydimethylsiloxane (PDMS) thin film and NPGD as the molecular carrier and plasmonic substrate, respectively. After stamping the SERS substrate onto the PDMS film, SERS measurements can be directly taken from the "sandwiched" target molecules. A potential advantage of this approach lies in that the SERS enhancement depends solely on distance, rather than surface affinity. Further benefits include cost-effectiveness, ease of fabrication, mechanical flexibility, biocompatibility, relatively few Raman peaks in the fingerprint spectral region, and low auto-fluorescence from PDMS.

8.6.2 Detection of Rhodamine 6G

Figure 8.10 illustrate the stamping SERS (S-SERS) approach with corresponding visual images to detect Rhodamine 6G (R6G). First, 4 μL of the prepared solution containing target molecules was dropped on the PDMS (Sylgard 184, Dow Corning) thin film having a thickness of ~ 125 μm and a dimension of ~ 1 × 1 cm^2 (Fig. 8.10 (a) and 8.10 (d)), which was prepared following standard protocols. The droplet was then dried on the PDMS substrate, forming an ultra-thin film of target molecules on the PDMS

surface after solvent evaporation in around 30 min (Fig. 8.10 (b) and 8.10 (e)). Finally, a NPGD substrate was stamped onto the PDMS surface with dried molecules, followed by focusing laser at the PDMS surface to detect SERS signals of sandwiched molecules (Fig. 8.10 (c) and 8.10 (f)). A SEM image was acquired to show the structure of the NPGD (Fig. 8.10 (g)) before stamping.

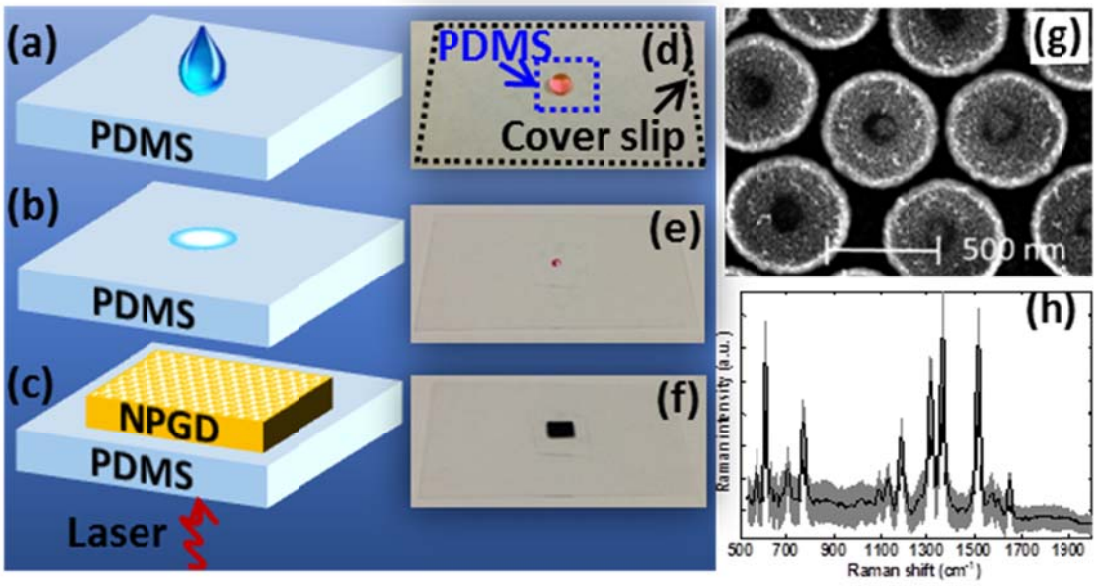

Figure 8.10 Schematics and corresponding images of S-SERS and NPGD: (a)-(f) See text for details; (g) SEM image of NPGDs. (h) SERS along the laser line from 100 μM R6G with average spectrum (black solid line) and ±1 standard deviation (gray shade).

LSRM described in Chapter 3 was used to evaluate the proposed technique. A 4 μL droplet of 100 μM R6G was dropped and dried on the PDMS surface, resulting in a ~ 1 mm spot. First, we examined the measurement uniformity by imaging a region around the mid-point between the center and circumference of the dried spot, which appeared visually uniform under bright-field microscopy. Figure 8.10 (h) shows the statistics of a total of 350 SERS spectra across the laser line where the solid line representing average

spectrum while the gray shade representing ± 1 standard deviation. The results suggest decent SERS uniformity across the sampled region.

Next, we show that S-SERS can reveal apparently invisible molecular coatings on PDMS. As shown in Fig. 8.11 (a), R6G Raman spectrum from dried 100 μM solutions on PDMS surface was measured and marked as "Normal". No normal Raman spectrum was observed from any samples with lower concentrations. NPGD substrate was then gently stamped against the PDMS, after which the sample was measured again and marked as "Stamped". Major Raman peaks for R6G at 611, 771, 1185, 1317, 1366, 1515 and 1650 cm^{-1} were observed. The 1366 cm^{-1} peak intensity for 100 μM R6G exhibits a ~ 10-fold enhancement after stamping.

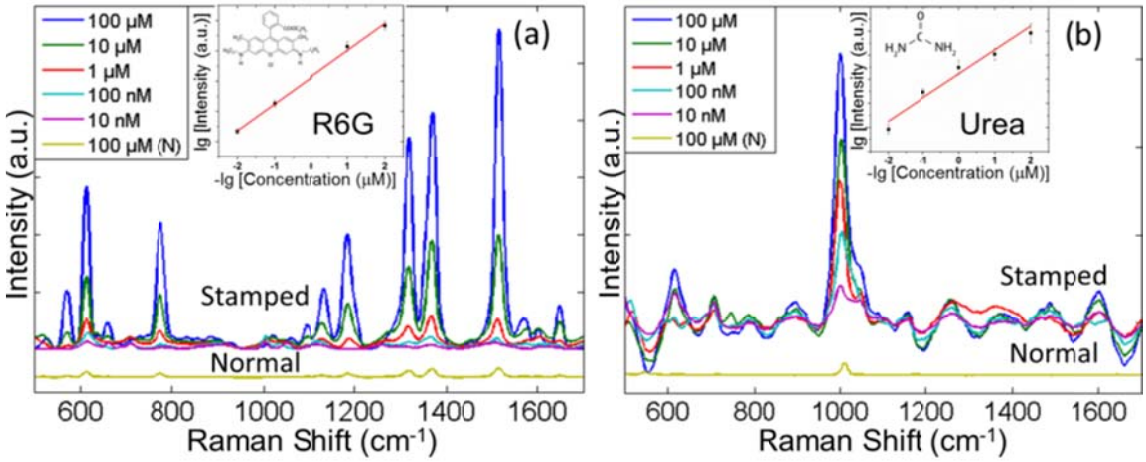

Figure 8.11 Before ("Normal") and after stamping ("Stamped") SERS for: (a) R6G, and (b) Urea. Insets show (a) R6G peak intensity at 1366 cm^{-1}, and (b) Urea peak intensity at 1001 cm^{-1} vs. concentrations.

8.6.3 Detection of Urea

To examine the capability of the stamping protocol for potential point-of-care and forensics applications, urea solutions with different concentrations ranging from 10 nM to

100 μM were used to simulate urine tests. The same sample preparation and measurement procedures aforementioned were applied. As shown in Fig. 8.11 (b), excellent intensity enhancement can be seen after stamping, with the primary Raman peak near 1001 cm^{-1} corresponding to the symmetrical C-N stretching vibration mode clearly observed. We note that the detection limit in the nanoMolar range is significantly lower than most SERS results reported in the literature in the milliMolar range [166], although direct comparison is not suggested because our technique employed dried samples as opposed to continuous-flow measurements in microfluidic configurations.

8.6.4 S-SERS Imaging of R6G

Conventional SERS measurements by transferring molecules of interest to SERS-active substrates can result in the unavoidable loss of spatial distribution of molecules on the original surface. To further demonstrate that the S-SERS technique has the capability to obtain spatio-chemical information from the PDMS surface, we have recorded a 3-dimensional (x,y,λ) SERS map from dried 100 μM R6G samples. The SERS map generated by peak intensity at 1366 cm^{-1} (Fig. 8.12 (b), marked by an asterisk) showed an identical yet clearer boundary of dried R6G droplet compared with the bright-field image (Fig. 8.12 (a)). Five different points inside the droplet were randomly chosen, and the corresponding spectra were shown in Fig. 8.12 (c).

8.6.5 Multiplexed S-SERS Imaging

To demonstrate multiplexed sensing and imaging capabilities, we have recorded a 3-dimensional (x,y,λ) SERS map from dried mixture samples of 100 μM urea and 1 mM acetaminophen (APAP). These concentrations are relevant for successful detection in urine. After stamping, we could not find the dry mark using bright-field microscopy

because both molecules are colorless, however, SERS maps successfully provided the spatial distribution information of both. As shown in Fig. 8.13, the SERS map generated by peak intensity at 1001 cm^{-1} for urea (Fig. 8.13 (a)) showed a similar overall boundary of dried droplet to the one generated by peak intensity at 856 cm^{-1} for APAP (Fig. 8.13 (b)), but different spatial distribution. As shown in Fig. 8.13 (c), spectra from five different positions were presented. For example, the peak intensity ratio of urea's major peak at 1001 cm^{-1} to that of APAP at 856 cm^{-1} is 2.45 at position 2 (P2), while the ratio is 0.67 at position 4 (P4). The results suggest that the two different molecules did not uniformly distributed on the PDMS surface during drying, likely due to differences in density, solubility, concentration, and affinity to the PDMS surface, etc. We note that the mixture data were collected from the circumference to emphasize the detection of the drying edge, where the well-known "coffee ring" effect caused more molecular accumulation.

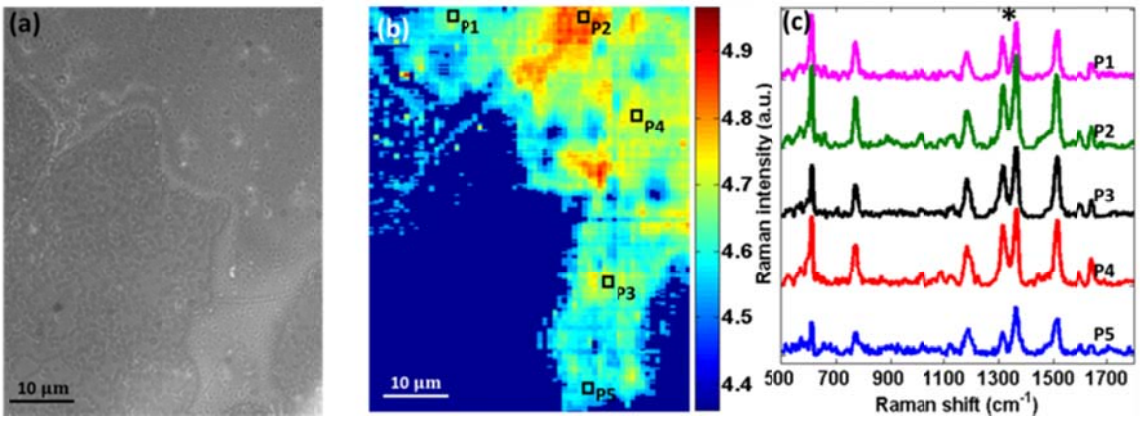

Figure 8.12 SERS image of dried 100 µM R6G : (a) bright filed image; (b) SERS map of peak intensity at 1366 cm^{-1} for R6G, and (c) spectra obtained at five different positions shown in (b),the 1366 cm^{-1} peak is marked by (*).

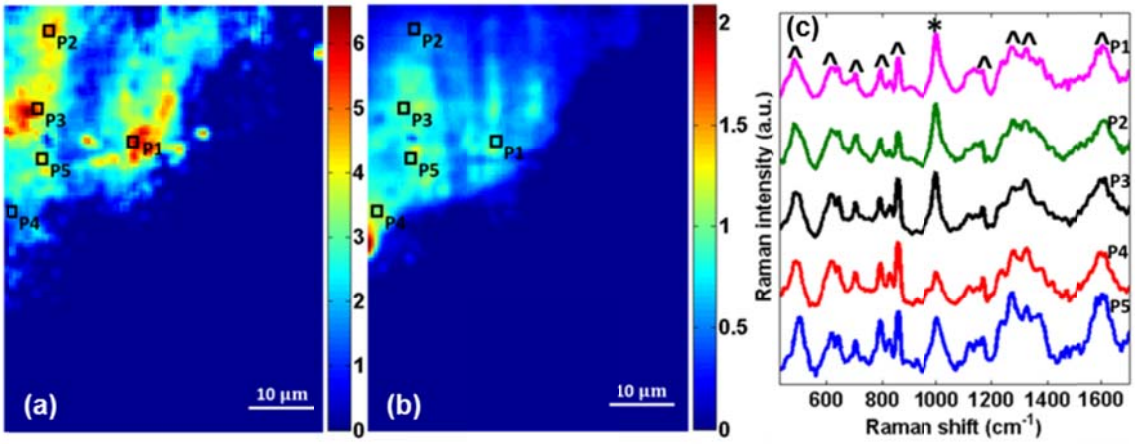

Figure 8.13 (a) SERS map of peak intensity at 1001 cm^{-1} for urea, (b) SERS map of peak intensity at 856 cm^{-1} for APAP, and (c) spectra obtained at five different positions shown in (a) and (e). Major peaks for urea (*) and APAP (^) are marked.

The proposed technique suggests new SERS applications. For example, PDMS is employed as a sample collector in solid-phase microextraction (SPME), while our results establish the feasibility for direct molecular analysis on PDMS without additional sample transfer required in current practice using gas chromatography. A second example is fingerprint sampling using PDMS for forensics, where our approach can provide chemical imaging of the latent fingerprint with associated exogenous molecules. Furthermore, our technique can provide label-free, multiplexed assay of biological fluids such as urine.

8.7 Conclusion

In conclusion, we have shown that nanoporous gold disks are highly effective SERS substrates with an enhancement factor of ~ 10^8, about 517 times higher than for unpatterned NPG films. This is significantly higher than the value 10^{3-4} that we estimate for the NPG disks discussed in Ref. 156 by comparing to solid gold disks published in

Ref. 157 and 158. The detection limit of benzenethiol self-assembled monolayer on a single NPGD is estimated to be 114 zeptomoles at SNR = 3. Our studies suggest that NPGDs may provide the basis for SERS substrates with very high sensitivity, uniformity, and capacity for monolithic sensor chip technology.

A novel label-free technique, stamping SERS (S-SERS) using NPGD as SERS substrates and PDMS as molecule carrier, has been demonstrated. R6G and urea detection with concentrations ranging from 10 nM to 100 μM can be detected using S-SERS. Moreover, the multiplexing capability has been demonstrated by large-area, high-resolution SERS mapping of mixture of urea and acetaminophen. By coupling with high-throughput Raman imaging systems based on line-scan or active-illumination, this technique can become a powerful tool for forensics analysis. The capabilities of detecting and imaging physiological concentrations of urea and APAP mixtures could lead to new point-of-care applications.

Related Publication

"Surface-enhanced Raman spectroscopy with monolithic nanoporous gold disk substrates", J. Qi, P. Motwani, M. Gheewala, C. Brennan, J. C. Wolfe and W. C. Shih, *Nanoscale*, 2013, **5**, 4105-4109.

"Stamping surface-enhanced Raman spectroscopy for label-free, multiplexed, molecular sensing and imaging", M. Li, J. Lu, J. Qi, F. Zhao, J. Zeng, J. C. Yu and W. C. Shih, *J Biomed Opt*, 2014, **19**, 50501.

"Monolithic nanoporous gold disks with large specific surface area, tunable plasmon resonance, and high-density, internal plasmonic hot-spots", F. Zhao, J. Zeng, M. M. Parvez Arnob, P. Sun, J. Qi, P. Motwani, M. Gheewala, C.-H. Li, A. Paterson, U. Strych,

B. Raja, R. C. Willson, J. C. Wolfe, T. R. Lee and W.-C. Shih, *Nanoscale*, 2014, **6**, 8199-8207.

"Internal and external morphology-dependent plasmonic resonance in monolithic nanoporous gold nanoparticles", J. Zeng, F. Zhao, Y. Li, C.-H. Li, Y. Yao, T. R. Lee and W.-C. Shih, *RSC Advance*, 2014 (under revision)

Chapter 9 Label-free, *In Situ* SERS Monitoring of Individual DNA Hybridization in Microfluidics

9.1 Introduction

Nanoporous disk has been characterized to be an attractive SERS substrate with ultrahigh EF, good uniformity and excellent reproducibility. To demonstrate the significant improvement of sensitivity in biomolecular sensing, *in situ* monitoring of DNA hybridization processes using NPGD are presented in this Chapter.

DNA hybridization, where two single-stranded DNA (ssDNA) molecules form duplex through non-covalent, sequence-specific interactions, is a fundamental process in biology [167]. Developing a better understanding of the kinetics and dynamic aspects of hybridization will help reveal molecular mechanisms involved in numerous biomolecular processes. To this end, sequence-specific detection of hybridization at the single-molecule level has been instrumental and gradually become a ubiquitous tool in a wide variety of biological and biomedical applications such as clinical diagnostics, biosensors, and drug development [168]. Label-free and amplification-free schemes are of particular interest because they could potentially provide *in situ* monitoring of individual hybridization events, which may lead to techniques for discriminating subtle variations due to single-base modification without stringency control or repetitive thermal cycling. To further increase experimental robustness and productivity and reduce complexity, single-step assays are highly desirable. For example, "sandwich" assay that involves multiple hybridization steps could generate highly convoluted results.

Currently, intermolecular diffusion of DNA molecules is commonly studied by fluorescence correlation spectroscopy (FCS) with an observation time limited to the

diffusion time of molecules through the observation volume [169]. Single-molecule fluorescence resonance energy transfer (smFRET) and other fluorescence techniques have also been employed to study conformational changes [170-175]. Unlike most fluorescence techniques, molecular beacons (MB) provide label-free detection. However like most other fluorescence techniques, MB also suffers from rapid photobleaching which prevents prolonged observation for slow processes [173, 176]. Recently, MB probes have been immobilized on plasmonic nanoparticles to harness metal-enhanced fluorescence and achieved a limit of detection (LOD) ~500 pM [177].

In addition to fluorescence techniques, label-free techniques for hybridization detection and biosensing include the use of localized surface plasmon resonance (LSPR) [178-180], extraordinary optical transmission [181, 182], electrochemistry [183, 184], circular dichroism spectroscopy [185] and mass measurements [186], but most of these techniques cannot provide the sensitivity for single-molecule detection. Recently, carbon nanotube field-effect transistor has been demonstrated to provide label-free, single-molecule detection at relatively high target concentrations (100 nM to 1 μM) [187].

We have explored the use of surface-enhanced Raman scattering (SERS) as a reporting mechanism for molecular sensing in Chapter 8. SERS is an attractive approach for label-free multiplexed DNA/RNA detection because of its single-molecule sensitivity [48, 146], molecular specificity [145, 188, 189], and freedom from quenching and photobleaching [190]. These distinct advantages have led to the development of a number of SERS sensing platforms for single DNA hybridization detection, including the crescent moon structures by Lu *et al.* [191], nanodumbbells by Lim *et al.* [192], and Au particle-on-wire sensors by Kang *et al.* [193]. These SERS sensing platforms were able to

achieve extremely high enhancement of local electromagnetic fields from "hot spots" by careful control of nanostructural assemblies.

In this Chapter, we present a SERS-based label-free approach capable of *in situ* monitoring of the *same* immobilized ssDNA molecules and their individual hybridization events over more than an hour. To achieve such performance, we have successfully implemented molecular sentinel (MS) [194-196] immobilized on nanoporous gold (NPG) disks [197] inside microfluidics. The microfluidic environment prevents sample drying, allows small sample volume, and permits agile fluid manipulation. MS involves the design of the complementary sequence of a target ssDNA into a stem-loop "hairpin". As shown in Fig. 9.1 (a), the hairpin probe has a thiol group at the 5' end for robust immobilization on gold nanostructures, and a fluorophore such as cyanine 3 (Cy3) at the 3' end for SERS detection. Cy3 yields a strongly enhanced SERS signal when the probe is in the hairpin configuration; this signal decreases when the probe is hybridized with the target and moves away from the surface. MS is label-free, requires only a single hybridization step, and can be multiplexed. MS has been employed to detect breast cancer marker genes ERBB2 and RSAD2 at concentrations of 1-500 nM using colloidal silver nanoparticles [195, 196]. Detection of Ki-67 at ~1 μM has been demonstrated using a triangular-shaped nanowire substrate, resembling a "biochip" approach [194], which is particular attractive for point-of-care applications where minimal sample preparation is desired.

We first demonstrate that the patterned NPG disk substrates provide enough SERS enhancement to enable single-molecule observation of immobilized MS probes. Second, we demonstrate that MS probes on NPG disks can be employed to perform time-

lapse *in situ* monitoring of hybridization. We then show that individual DNA hybridization events can be observed and quantified as early as ~10 min after introducing 20 pM complementary target ssDNA molecules.

9.2 Material and Methods

9.2.1 Molecular Sentinel Probes and ssDNA Molecules

We selected the ERBB2 gene, a critical biomarker of breast cancer, as the ssDNA target molecules. The hairpin probe consists of a complementary sequence of ERBB2 as shown in Table 9.1 ("ERBB2-sentinel"). Table 1 also shows the sequences of the ssDNA target ("ERBB-target") and non-complementary ssDNA ("Non-complementary control"). The underlined portion indicates the complementary stem sequences of the MS probe, and the bolded portion represents the target sequences complementary to the loop region of the MS hairpin probe. All ssDNA molecules were purchased from Integrated DNA Technologies (IDT, Coralville, IA).

Table 9.1 MS probe, target and non-complementary ssDNA.

ssDNA	Sequence
ERBB2-sentinel	5'-SH-CGCCAT CCACCCCCAAGACCACGACCAGC AGAATATGGCG-Cy3-3'
ERBB2-target	5'-**GTTGGCATTCTGCTGGTCGTGGTCTTGGGG GTGGTCTTTG**-3'
Non-complementary control	5'-GCCAGCGTCGAGTTGGTTTGCAGCTCCTGA-3'

9.2.2 NPG Disks

NPG disks, 500 nm in diameter, 75 nm in thickness and 5 nm in pore size, were fabricated by a process described previously in Chapter 8. [66] [66] A SERS enhancement factor of ~5×10^8 was obtained using benzenethiol self-assembled monolayer with 785 nm laser excitation.

9.2.3 MS Probes Immobilization on NPG Disks and Hybridization

MS hairpin probes were immobilized onto NPG disk substrates at the bottom of a PDMS microwell (2 mm diameter, 4 mm height) by incubation. 10 µL hairpin probe solutions were dispensed into the PDMS well and incubated for 40 min, following which the PDMS wells were removed and the substrates rinsed thoroughly in DI water. They were then immersed in 0.1 mM 6-mercapto-1-hexanol (MCH) for 10 min, followed by another DI water rinse. The substrates were then mounted inside a temperature-controlled microscope microfluidic cell culture stage (FCS2, Bioptechs) as shown in Fig. 9.1 (b). The microscope stage was locked to ensure SERS measurements from a fixed region. A syringe pump was used to deliver target solutions of known concentration for hybridization.

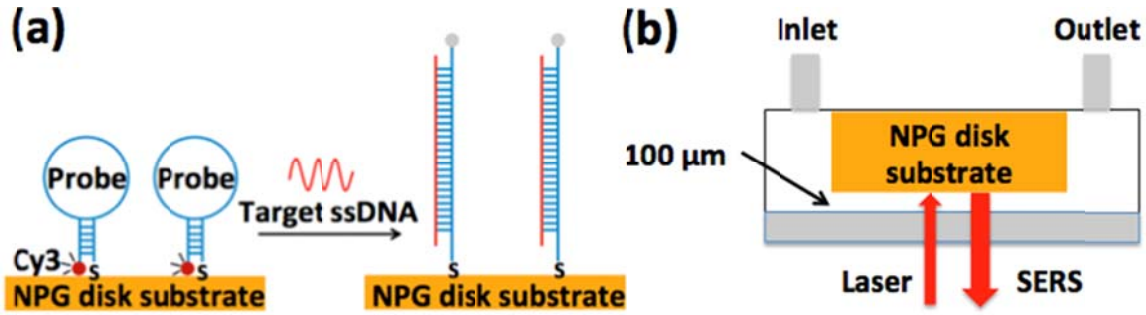

Figure 9.1 Schematic of MS sensing mechanism in microfluidics: (a) (left) ssDNA MS probes in a hairpin configuration are immobilized on NPG disk substrates; (b) Microfluidic configuration for SERS data acquisition.

9.2.4 SERS Measurement

SERS measurements were carried out using a line-scan Raman microscopy described in Chapter 3. The acquisition time for each CCD frame was 10 s at a laser power density of 0.1 mW/µm^2. Full-frame data of dimension 133 (spatial) x 1340 (λ)

were collected, equivalent to 133 "point-spectra", each from a 1-μm^2 spot. A "line-spectrum" was obtained by averaging the 133 point-spectra in one CCD frame.

9.3 SERS Detection of Immobilized MS Probes on NPGD

Figure 9.2 shows SERS line-spectra from different concentrations of ERBB2-sentinel probes on NPG disk substrates by incubation (500 pM–5 nM) and drop cast (100 pM), respectively. Each line-spectrum is an average of 133 point-spectra from a single CCD frame (133 (spatial) x 1340 (λ)). The baselines were approximated by a 5^{th} order polynomial and removed. The major peaks at 1197 cm^{-1}, 1393 cm^{-1}, 1468 cm^{-1} and 1590 cm^{-1} were assigned to Cy3 [188]. The presence of these major peaks indicates that the probe molecules were in their hairpin configuration, with the 3'-Cy3 near the gold surface. The Raman band at 1078 cm^{-1} (marked with an asterisk) is assigned to MCH. In the following experiments, we use the Cy3 peak height at 1197 cm^{-1} as the SERS intensity indicator. The immobilized probe density of drop cast onto NPG disk substrates was estimated from the number of probe molecules pipetted onto the NPG disk surface. Drop cast of 5 μL 100 pM probe solution resulted in about 2 probe molecules/μm^2 after the rinse-MCH-rinse protocol described previously.

9.4 Probe Density Estimation

To quantify and calibrate the surface density of the immobilized MS probes, we also developed an alternative technique for probe immobilization by drop casting 5 μL of probe solution directly onto the NPG disk substrate. After drying, the substrate was processed by the same rinse-MCH-rinse procedure described in the incubation approach. Thus, with known area of dried droplet, the concentration of the probe solution and SERS intensity of Cy3, the number of probe molecules on the surface can be estimated. For

example, five SERS measurements were taken near the center of the dried spot by 2 μL 100 pM MS probe solution. This was to avoid taking data from the circumferences where "coffee ring" effect is apparent. The average SERS spectra are shown in Fig. 9.3 (a). The round shaped area was ~ 3mm diameter, resulting in a surface density of 42.6 molecules/μm^2 (blue spectrum). We observed a ~ 80% intensity decrease after MCH rinse (red spectrum), suggesting the probe density was 8.5 molecules/μm^2. An additional 50% intensity drop was observed after the following DI water rinse, leading to 4.2 molecules (black spectrum). Considering the surface coverage of the NPG disks to be ~ 50%, the average probe density on NPG disks is ~ 2 molecules/μm^2. We note that this represents a conservative estimate (i.e. upper bound) because we intentionally avoided the circumferences where more molecules accumulated.

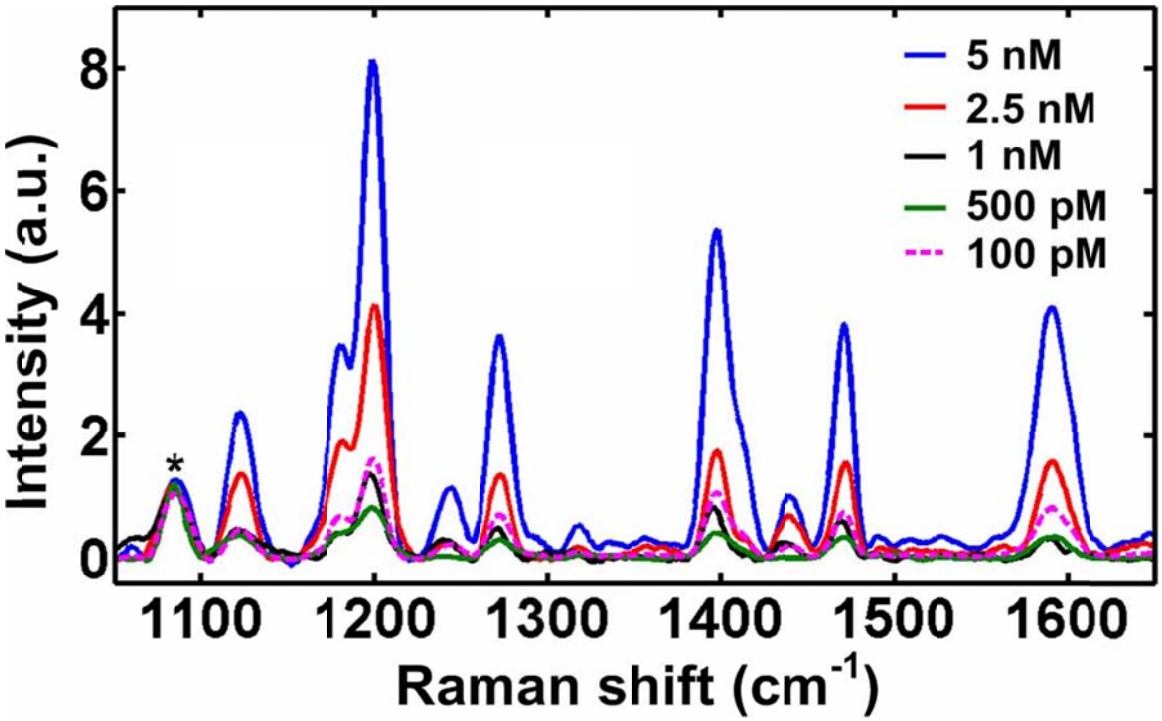

Figure 9.2 SERS spectra of the MS probes on NPG disk substrates by incubation (500 pM–5 nM) and drop cast (100 pM) immobilization protocols.

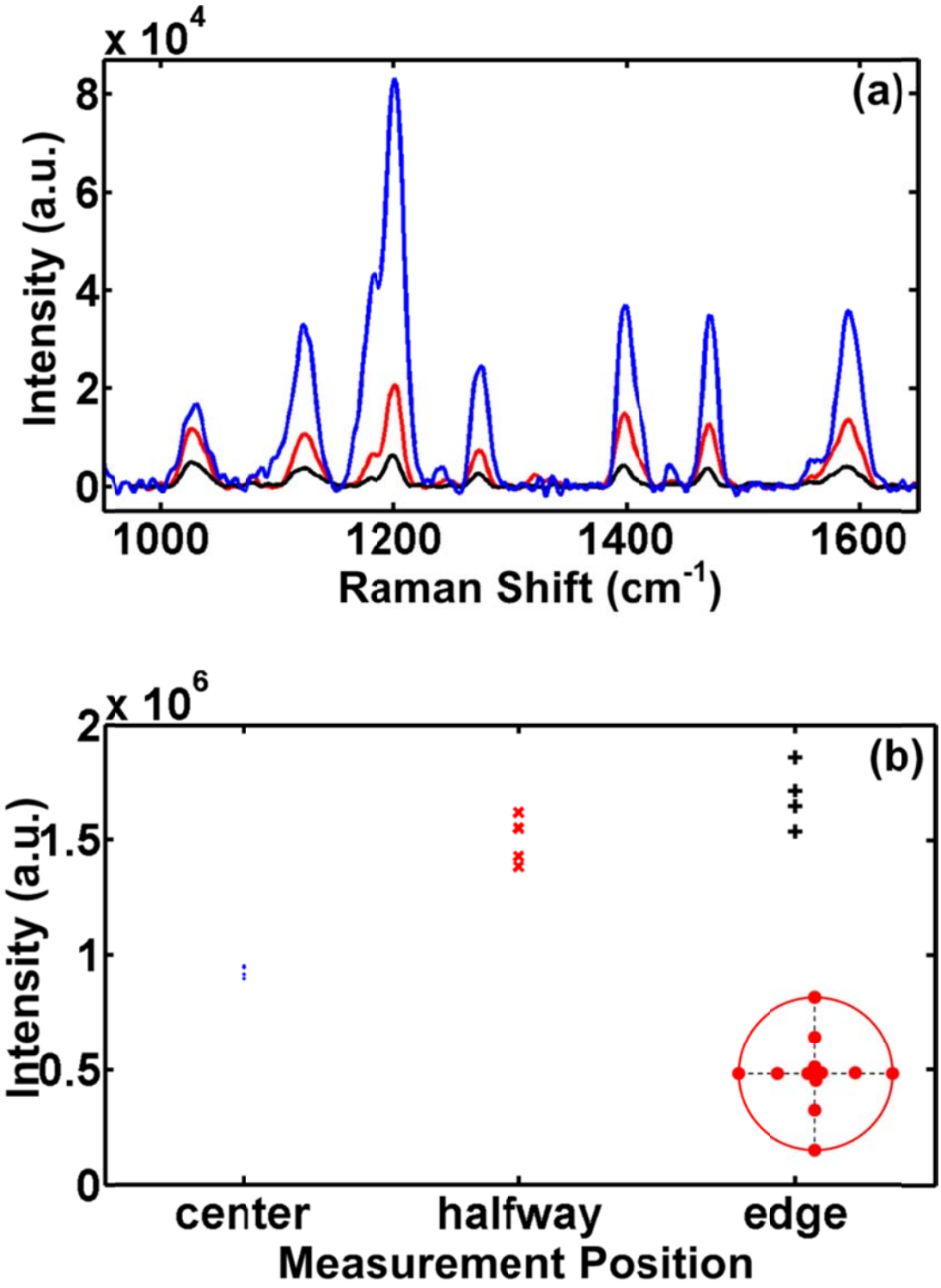

Figure 9.3 (a) averaged SERS spectra before (blue), after (red) MCH treatment and after buffer wash step (black); (b) Cy3 intensities at different positions, the red circle and red dots represents the dried area of probe solution and measurement positions, respectively.

We also studied the probe density distribution over the entire dried spot. Four SERS measurements were performed at the center, halfway and circumference of the dried spot, respectively. Figure 9.3 (b) shows the Cy3 intensities at different positions just after the final rinse. The 12 red dots and the red circle schematically in the lower right corner represent measurement positions with respect to the dried spot. Cy3 intensities were lower at the center and higher at the edge. This again suggests our probe density estimate likely represents an upper bound. The probe density on NPG disk substrates using the incubation method was estimated by comparing the SERS intensity with the drop cast method. As shown in Fig. 9.3 (b), the average SERS intensity from substrates incubated in 1 nM probe solution was similar to substrates using drop cast. Thus we concluded that the probe density was ~ 2 molecules/μm^2 for NPG disk substrates incubated in 1 nM probe solution. Similarly, the probe density for NPG disk substrates incubated in 5 nM probe solution was estimated to be ~ 10 molecules/μm^2.

9.5 *In Situ* Monitoring of DNA Hybridization with Varying Target ssDNA Concentrations Using Incubation for Probe Immobilization

In the first series of experiments, we employed the incubation technique to immobilize 5 nM sentinel probe solutions, along with target concentrations from 5 to 20 nM. SERS monitoring began after the substrate was mounted into the microscope microfluidic chamber with 10 – 15 min acquisition intervals. Figure 9.4 shows the Cy3 intensities at 1197 cm^{-1} from the line-spectra after introducing the target ssDNA molecules. Three representative line-spectra from the hybridization and the plateau phases of this experiment are shown in the upper-right corner.

As shown in Fig. 9.4, the SERS intensity began to decrease due to hybridization after introducing the 20 nM target solution. The SERS intensity reached a plateau phase at ~170 min, indicating the endpoint of hybridization. Measurements over another 40 min indicated that no further hybridization occurred. We observed a 60% SERS intensity decrease from the 5 nM/20 nM (probe/target) experiment, i.e., 60% of the immobilized probes reacted with the target ssDNA molecules. A plausible explanation for the incomplete consumption of all immobilized probes is inefficient mass transfer of target ssDNA molecules to the NPG disk surface. According to the adsorption kinetics model of biomolecules, only a tiny fraction of target ssDNA molecules were able to react with probes in the current diffusion-limited configuration.

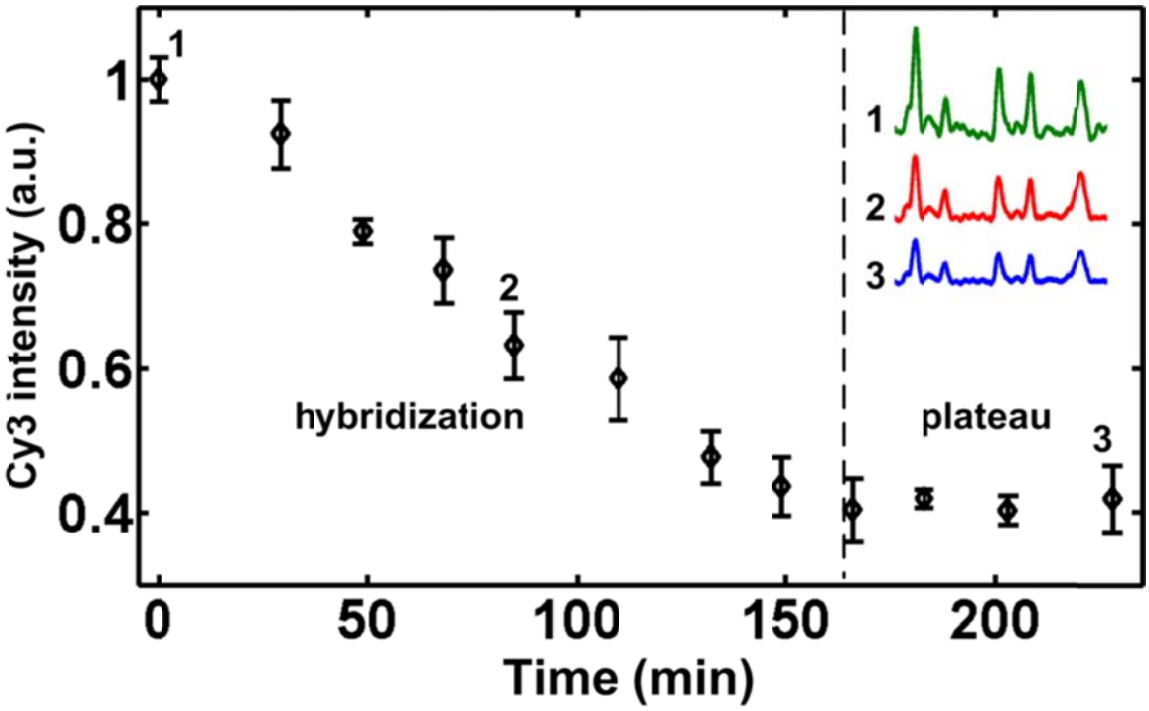

Figure 9.4 *In situ* hybridization monitoring using SERS line-spectra: (a) 5 nM MS probe hybridization with 20 nM target.

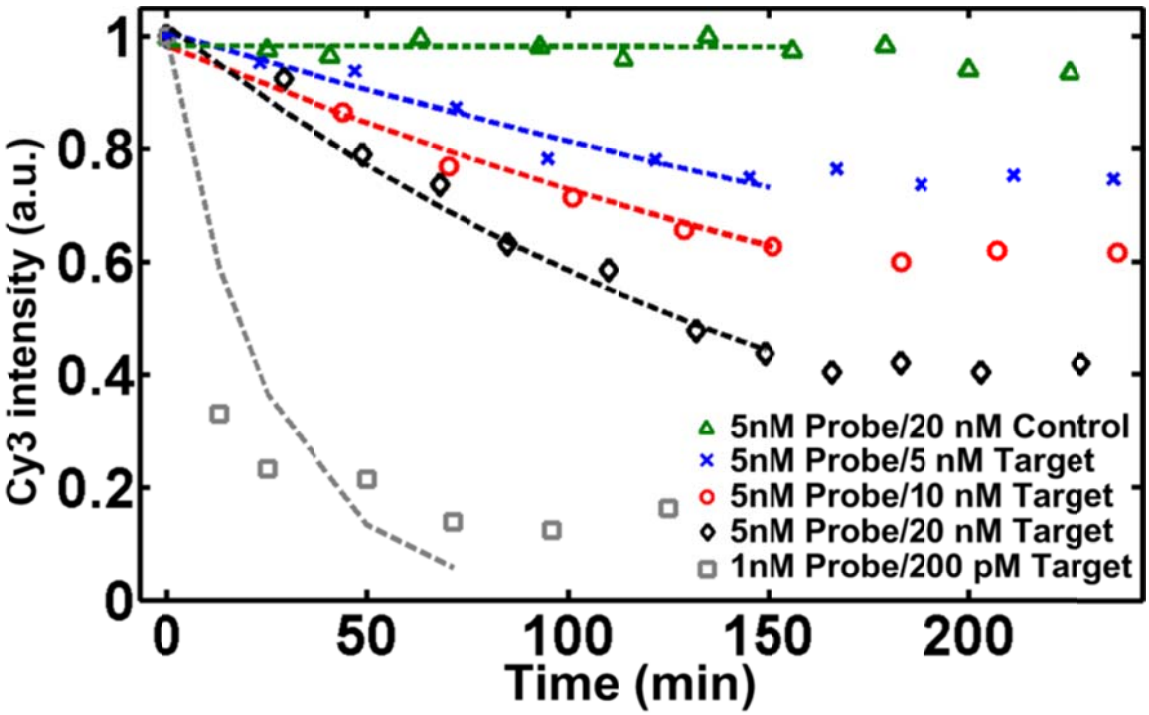

Figure 9.5 *In situ* hybridization monitoring using SERS line-spectra: 5 nM MS probe hybridization with 5, 10, 20 nM target and 20 nM non-complementary ssDNA; 1 nM MS probe hybridization with 200 pM target.

Figure 9.5 shows the hybridization and plateau phase of experiments with different target concentrations and non-complementary ssDNA molecules. The dashed curves are exponential fits. We observed a greater time constant at higher target concentrations, suggesting that target concentration can be determined by monitoring the decrease rate of Cy3 intensity. Alternatively, the final intensity value was also indicative of the target concentration. In the negative control experiment, 20 nM non-complementary ssDNA molecules did not cause a statistically meaningful SERS intensity change (± 5%). Since the non-complementary ssDNA molecules could not hybridize with the ERBB-sentinel probe, the Cy3 label remained close to the gold surface, thus maintaining a strong and stable SERS signal. Furthermore, the stable SERS signal

indicated that there was no photobleaching during experiments and the probe immobilization was robust. We thus attributed any signal decrease after adding target ssDNA molecules to hybridization. To explore the detection limit in terms of number of target DNA molecules for our sensor, we reduced the concentration of the sentinel probe to 1 nM for immobilization by incubation, resulting in a probe density of about 2 molecules/μm^2. The Cy3 SERS intensity time trace after adding a 200 pM target solution is displayed as squares in Fig. 9.5. The Cy3 intensity decreased significantly within the first 13 min after the introduction of target and reached a plateau phase 90 min later. About 80% overall intensity decrease was observed.

Instead of the overall time trace extracted from the line-spectra as shown in Fig. 9.4 and Fig. 9.5, we next study individual time traces from point-spectra by taking advantage of the spatial resolution of the line-scan Raman system. Ideally, there were 133 time traces using the point-spectrum, each from a 1-μm^2 spot. Since the probe density was estimated to be about 2 molecules/μm^2 for substrates incubated in 1 nM MS probe solutions, and we observed an average SERS intensities of 200 CCD counts, we interpret each 100 CCD counts as a single MS probe. Equivalently, each intensity decrease of 100 CCD counts during hybridization is attributed to a single hybridization event. We consequently use an interval of 100 CCD counts between centers of bins in the following statistical analyses.

Figure 9.6 displays the histograms of immobilized probe count and hybridization event count by studying individual time traces. The point-spectra showing extremely high SERS intensities at different peak locations different from Cy3, likely from impurities in the solution, were excluded from the statistical study. The number of time traces involved

in the statistical analyses are 106, 101, 112 and 93 for probe/target pairs of 5 nM/5 nM, 5 nM/10 nM, 5 nM/20 nM and 1 nM/200 pM, respectively. The blue bars in Fig. 9.6 represent the frequency of the immobilized probe count on 1-μm^2 NPG disk surface before hybridization. We found that these histograms (blue bars) can be better fit by Poisson distribution than Gaussian with an average of 10 and 2 (shown as magenta diamonds) for substrates incubated in 5 nM and 1 nM probe solutions, respectively. This agrees well with our previous interpretation that 100 CCD counts represent a single probe.

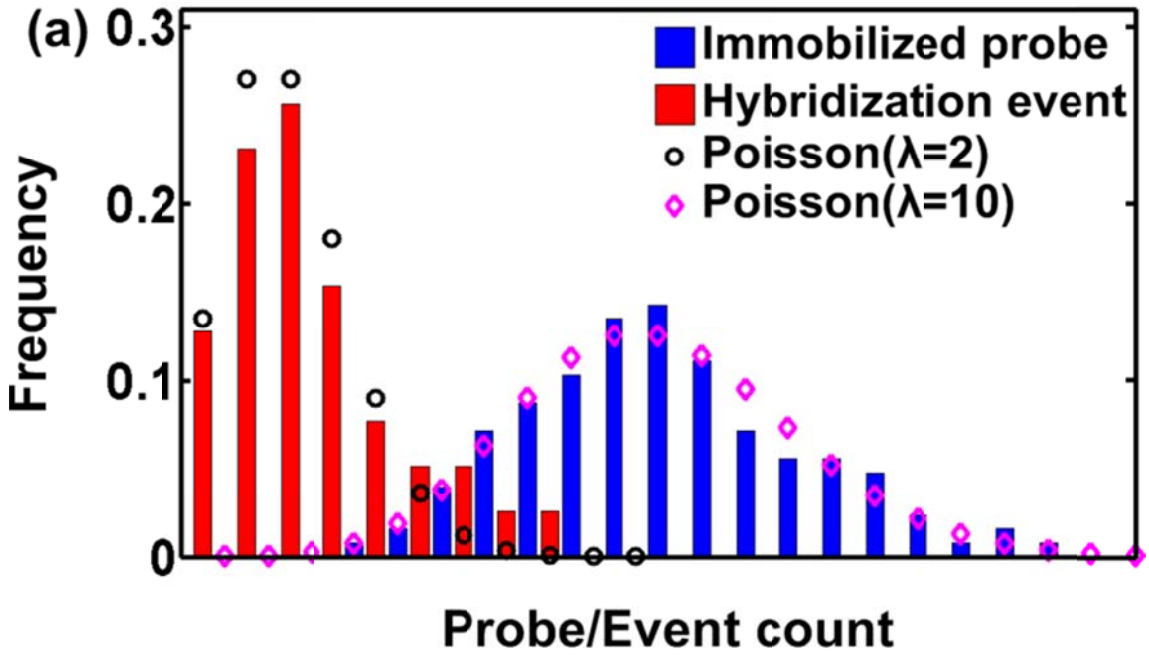

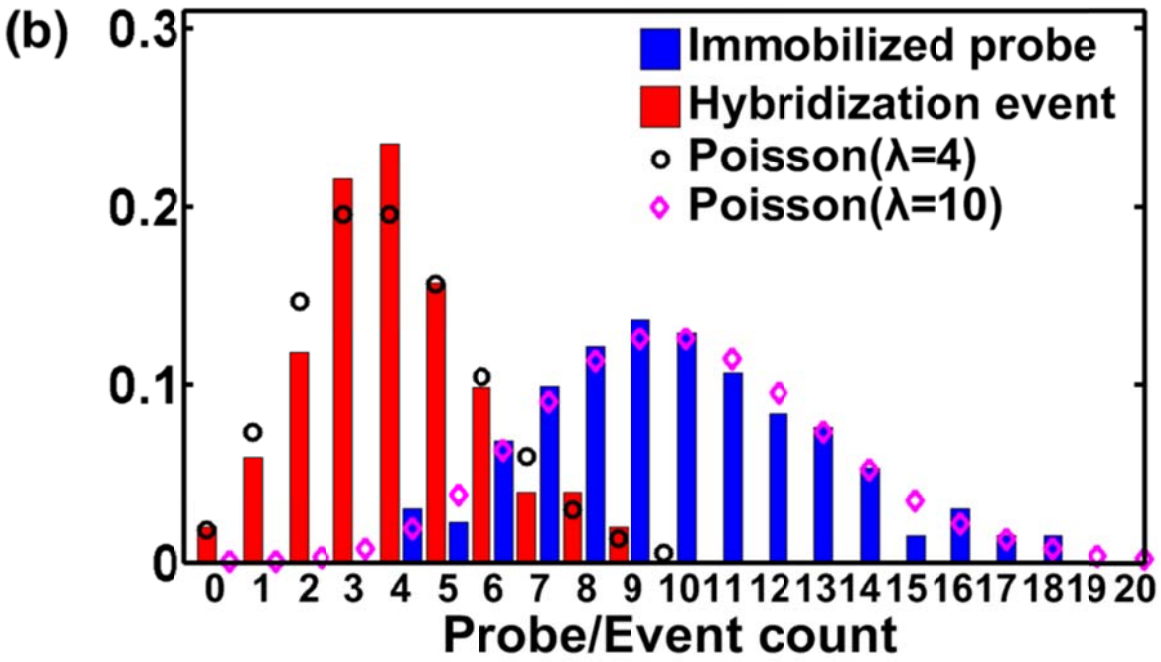
(b)
0.3
0.2
0.1
0
Immobilized probe
Hybridization event
Poisson(λ=4)
Poisson(λ=10)
0 1 2 3 4 5 6 7 8 9 10 11 12 13 14 15 16 17 18 19 20
Probe/Event count

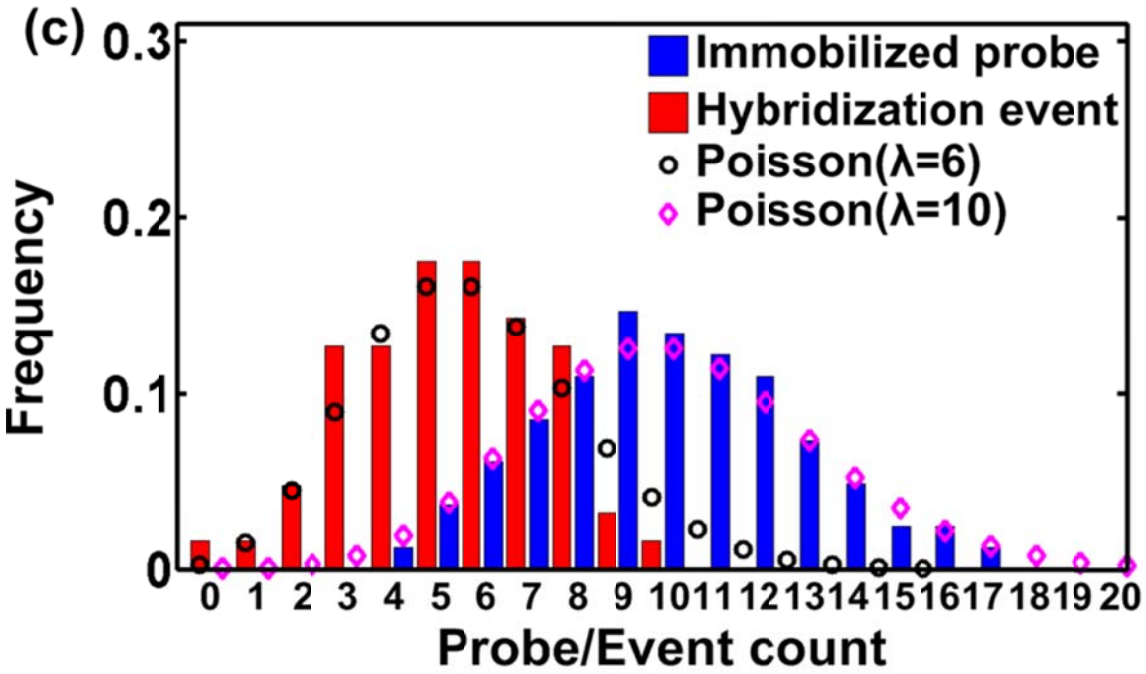
(c)
Frequency
0.3
0.2
0.1
0
Immobilized probe
Hybridization event
Poisson(λ=6)
Poisson(λ=10)
0 1 2 3 4 5 6 7 8 9 10 11 12 13 14 15 16 17 18 19 20
Probe/Event count

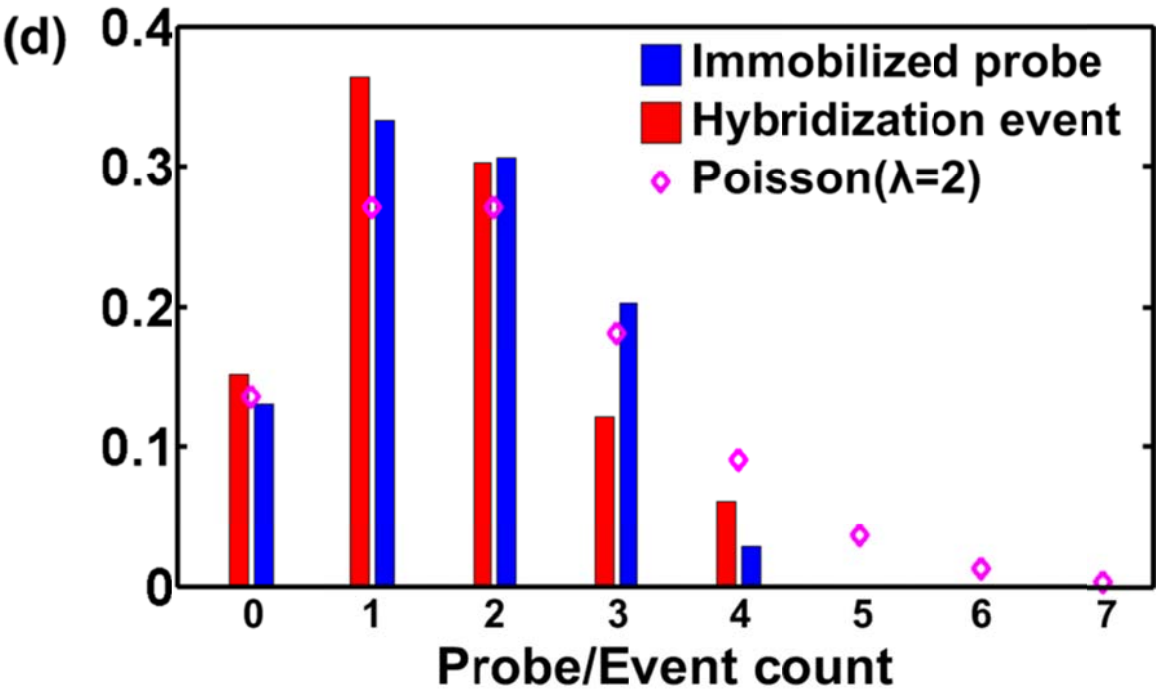

Figure 9.6 Statistical analysis of individual time traces at probe/target concentrations of (a) 5 nM/5 nM, (b) 5 nM/10 nM, (c) 5 nM/20 nM and (d) 1 nM/200 pM. See text for details.

The red bars represent the frequency of hybridization event count. We observe more hybridization events at higher target concentrations in 5 nM incubation experiments, which is consistent with the intensity time traces in Fig. 9.5. Similarly, the histograms of hybridization event count can be better fit by Poisson distribution (black circle in Fig. 9.6 (a)-(c), magenta diamond in Fig. 9.6 (d)) with averages of 2, 4, 6, and 2 for 5 nM, 10 nM, 20 nM and 200 pM target concentrations, respectively. In other words, 2, 4, 6, and 2 hybridization events were observed on average for 5 nM, 10 nM, 20 nM, and 200 pM target solutions, respectively.

9.6 *In Situ* Monitoring of DNA Hybridization with 20 pM Target ssDNA Concentration Using Drop Cast for Probe Immobilization

In this series of experiments, we employed drop cast as an alternative approach for probe immobilization. As mentioned in section 9.4, the probe surface density by drop cast of 100 pM probe solutions is equivalent to that from incubating in 1 nM solutions, with both methods resulting in about 2 probe molecules/μm^2 before hybridization. A protocol identical to the previous experiment was followed except that a 20 pM target solution was used. As shown in Fig. 9.7 (a), the line-spectra SERS intensity decreased substantially after the 20 pM target was introduced with the earliest detection at 10 min. Figure 9.7 (b), (c) and (d) show the full-frame SERS images just before adding the target, during hybridization and at the last measurements (time points 1, 2 and 3 in Fig. 9.7 (a)), respectively. The major peaks from Cy3 clearly visible in Fig. 9.7 (b) diminished significantly in Fig. 9.7 (d). The overall Cy3 intensity decrease was ~80% at 90 min after introducing the target. As shown in Fig. 9.8 (a), the histogram (blue bars) of the immobilized probe count agrees well with Poisson distribution with an average of 2. A similar distribution is observed in the histogram of hybridization event count as discussed later. Analyzing the point-spectra from 64 spots, four representative intensity patterns are observed and shown in Fig. 9.8 (b). Trace 1 (red), Trace 2 (blue) and Trace 4 (black) exhibit a single-step intensity drop of 100, 200, and 400 CCD counts, respectively. Trace 3 (magenta) exhibits a two-step intensity drop with 200 CCD counts in the first step and then 100 in the second. The observation of quantized intensity decreases in individual time traces provide further support that individual hybridization events were observed. In the experiment using incubation in 1 nM probe solution, we also observed similar

quantized intensity decreases in individual time traces. The intensity patterns 1-4 correspond to 1-4 hybridization events (red bars) taking place on the 1-μm^2 spots.

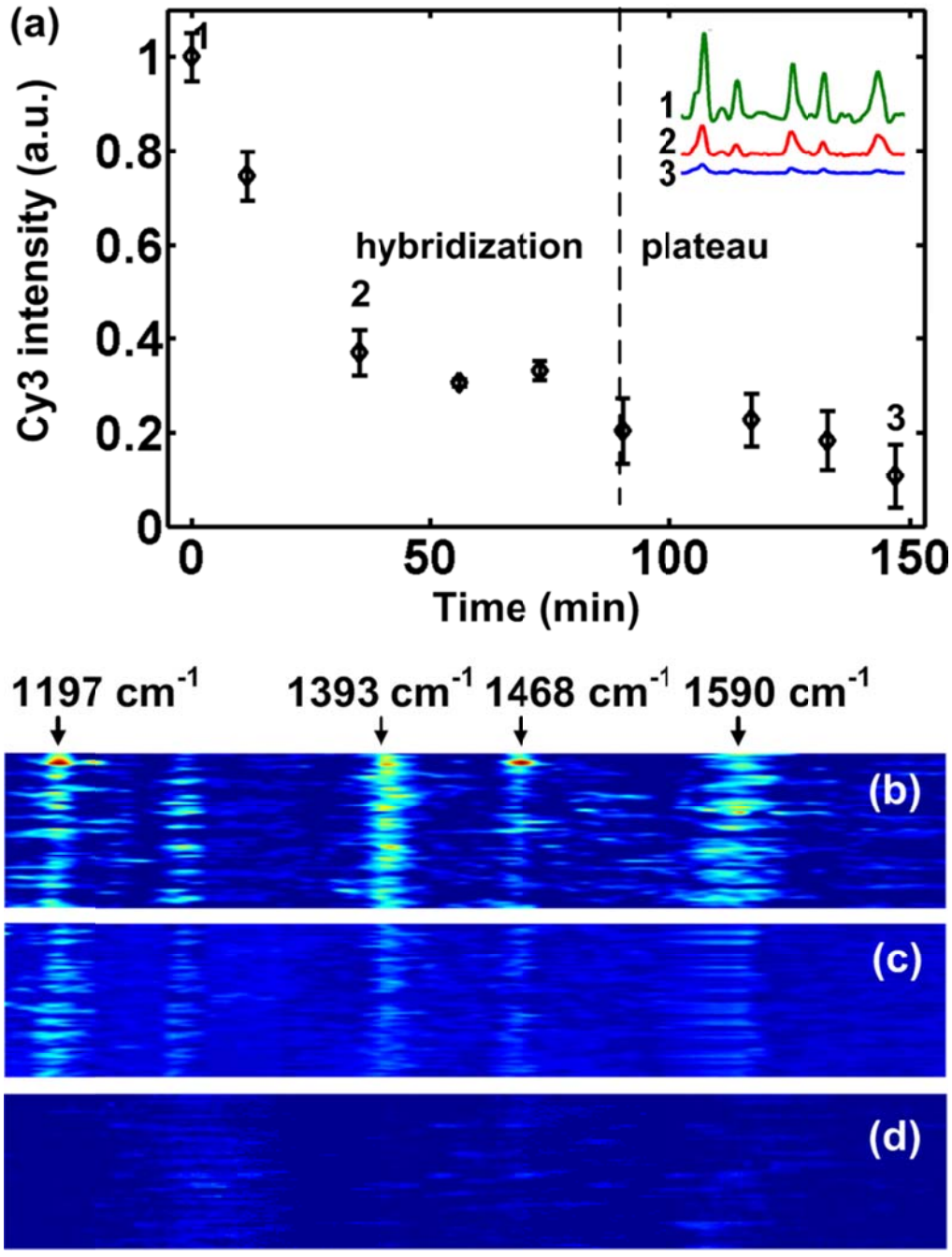

Figure 9.7 (a) Overall Cy3 intensity trace with 20 pM target DNA; SERS image at (b) t=0 min, (c) t=40 min and (d) t= 150 min; the horizontal axis represents wavenumbers. Each row in the SERS image is a single point-spectrum. The major bands of Cy3 are labelled.

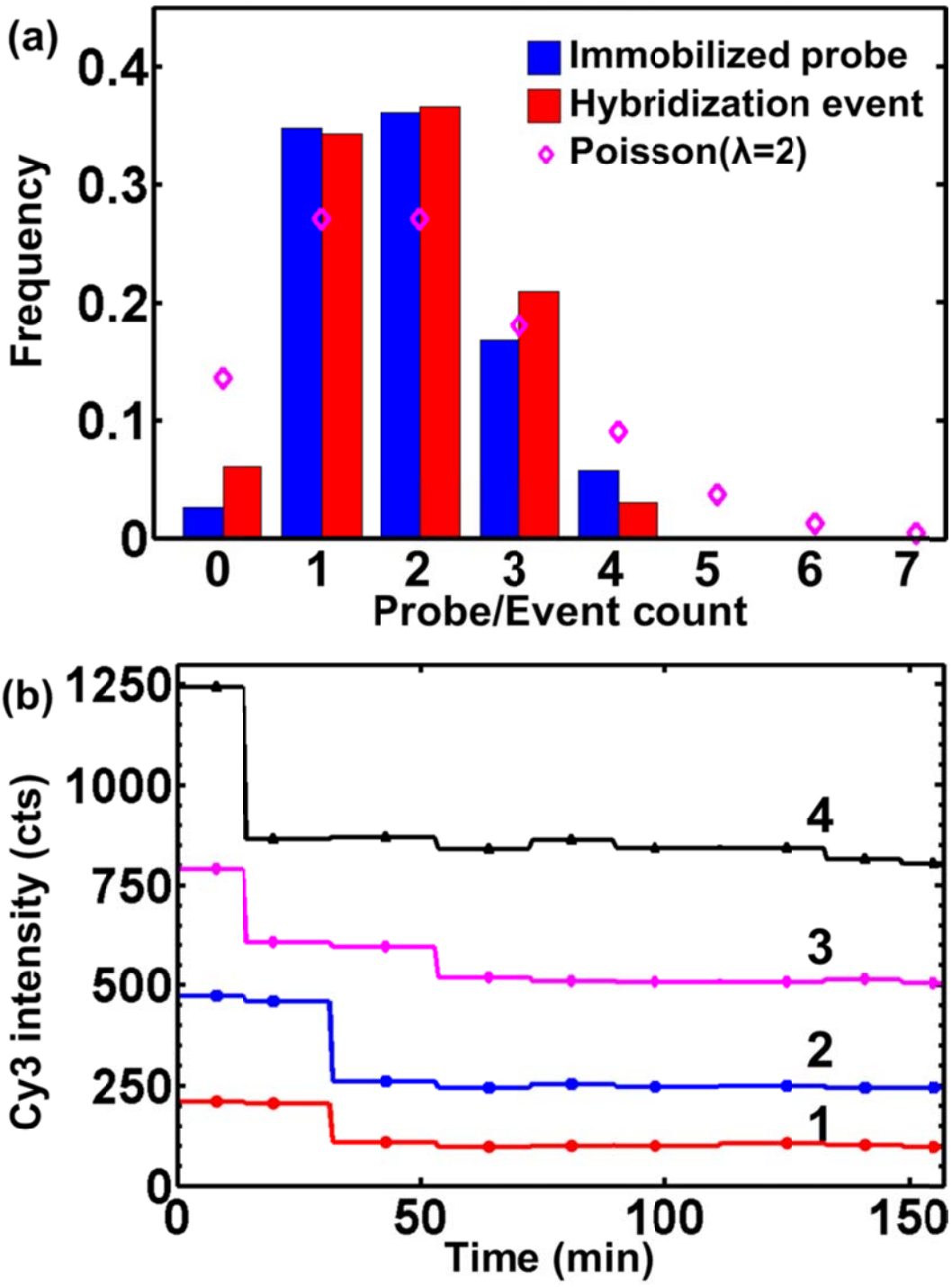

Figure 9.8 (a) Histogram analysis of individual time traces from 64 1-μm^2 spots; (b) representative intensity patterns 1-4 corresponding to the hybridization counts 1-4 in Fig. 7.8 (a) (red bars).

Using the representative intensity patterns shown in Fig. 9.8 (b), we have performed a statistical analysis of 64 individual hybridization time traces with results shown in Fig. 9.8 (a). As mentioned earlier, the blue bars represent the statistics of immobilized MS probes. The red bars represent total hybridization events during the hybridization phase over individual 1-μm^2 spots. Both histograms can be better fit with a Poisson distribution of $\lambda = 2$ (diamond in Fig. 9.8 (a)) than with a Gaussian distribution. Although there has been debate on whether to expect a Poisson distribution of SERS intensities at ultra-low concentrations [148, 198, 199], here it is only employed to provide additional insight into our results, not to justify the claim of single-molecule detection. In addition, the enhancements of SERS signals from the NPG disk substrates were uniform across a large area (at least 100 ×100 μm^2) [197]. Therefore, our measurements of SERS intensities are reliable, and not affected by the factors [198] that could potentially invalidate interpreting Poisson statistics as single-molecule events.

Next we discuss the implications of our results within the context of microfluidic sensors, where the static or laminar flow nature poses significant challenges for achieving low LOD. Unlike sensors implemented in un-restricted fluidic environments, e.g., beaker, where active mixing is readily available, the transport of target molecules to the sensing surface largely depends on diffusion in microchannels. Compared with several recently published label-free microfluidic sensors, our demonstrated LOD (20 pM) is respectable even without any attempt of optimization [177, 200-202]. After all, the technique does have sensitivity approaching single-molecule. So a future challenge appears to be implementing efficient means for bringing target molecules to the MS probes for

hybridization. For example, it is quite possible to lower the LOD with the help of active concentrating mechanisms such as dielectrophoresis [203].

9.7 Conclusion

We have developed a label-free technique to *in situ* monitor DNA hybridization using molecular sentinel probes immobilized on patterned nanoporous gold disk SERS substrates by taking advantage of the ultrahigh SERS sensitivity of these novel substrates. In addition, we were able to detect the onset of hybridization events within ~10 min after introducing 20 pM target ssDNA molecules. Given sensitivity approaching the single-molecule limit, robust SERS signals, and simple detection system, this approach could find potential applications in time-lapsed monitoring of DNA interactions and point-of-care applications.

Related publication

This chapter has been published as "Label-free, *in situ* SERS monitoring of individual DNA hybridization in microfluidics", J. Qi, J. Zeng, F. Zhao, S. H. Lin, B. Raja, U. Strych, R. C. Willson and W.-C. Shih, *Nanoscale*, 2014 DOI: 10.1039/C4NR01951B.

Chapter 10 Conclusions and Future Directions

The work presented in this thesis mainly aims at: (1) improving the throughput line-scan Raman microscope and evaluating the performance on chemical mapping of cell population; (2) developing parallel Raman microscope based on multiple-point illumination and the application of rapid hyperspectral Raman imaging for label-free compositional microanalysis; (3) cancer diagnosis and margin detection using LSRM combined with OCT; (4) characterization of GNI as a SERS substrate using LSRM and active-illumination Raman microscope; (5) developing and characterizing NPGD as a SERS substrates and the applications in biomolecular sensing; and (6) *in situ* monitoring of individual DNA hybridization event using NPGD.

10.1 Summary

10.1.1 Improving the Line-scan Raman Microscope

The line-scan Raman microscope (LSRM) achieves significant throughput advantage over conventional point-scan Raman microscopy by projecting a laser line onto the sample and imaging the Raman scattered light from the entire line using a grating spectrograph and a charge-coupled device (CCD) camera. The resolution in the x- and y-direction has been characterized to be ~600-800 nm for 785 nm laser excitation. The line-scan Raman microscope enables rapid classification of microparticles with similar shape, size and refractive index based on their chemical composition. Several applications such as identification and counting of organic microparticles, chemical imaging of spore and microalgae have been demonstrated. The overall image acquisition time is significantly reduced by ~100 times compared to conventional Raman imaging methods but provides comparable spatial and spectral resolution.

10.1.2 Development of Novel Active-Illumination Raman Microscope

The novel active-illumination Raman microscope developed in Chapter 4 provides the flexibility to simultaneously image multiple points that are not aligned along a line in contrast to line-scan Raman microscope presented in Chapter 3. The spatial (x-y-z) resolution has been characterized to be 0.9, 0.9 and 4.5 μm, respectively. As many as about 1,000 micro-sized laser spots semi-randomly distributed among 100 × 100 μm^2 field of view has been achieved. In addition, rapid imaging capability of parallel Raman microscope has been demonstrated by several applications, for example, chemical imaging 245 mixed polystyrene and PMMA microspheres within 1.5 sec and identification of about 100 bacterial spores within 40 sec. The new capabilities of the parallel Raman microscope could have significant impact in Raman imaging in biological and biomedical applications.

10.1.3 Cancer Diagnosis and Margin Detection

Classification of mouse tissues including small intestine, kidney and liver, margin detection in well differentiated liposarcoma as well as identification of gastrointestinal sarcoma tumor and Myxoma have been demonstrated using LSRM. In contract, structural images from optical coherence tomography (OCT) are indistinguishable in these applications. However, Raman spectroscopy is lack of real-time imaging capability due to the weak signal intensity. Therefore, combing the two techniques provides the potential for tissue analysis and margin detection as a quantitative and qualitative approach.

10.1.4 Characterization of DC-sputtered GNI

DC-sputtered GNI substrates have attracted significant attention recently due to its excellent plasmonic enhancement, structural stability, and simple fabrication. Chapter 6 provides multimodal characterization of GNI morphological evolution by correlating data obtained from SEM, LSPR extinction spectroscopy, and SERS microscopy. A rigorous determination of the SERS enhancement factor for benzenethiol SAMs on evolving GNI substrates is presented. Rapid statistical analysis shows excellent large-area SERS uniformity by hyperspectral Raman imaging systems based on active-illumination which enables parsimonious sampling of only 2.7% of the total sampled area by LSRM.

10.1.5 NPGD as a SERS Substrate

NPGD has a SERS enhancement factor of about 10^8, 450 times larger than that of unpatterned NPG thin films of the same thickness. The effective surface area of NPGD is estimated to be about 6.3times of its projected area, and can provide more attachment sites for target analyte adsorbates within a 3-dimensional volume. A single NPGD decorated with attomole level benzenethiol molecules can be detected within 20 seconds by an uncooled detector or within 25 milliseconds by a cooled detector. The proposed NPGD can be fabricated with controlled size and provide highly reproducible SERS measurements, demonstrated by large-area mapping of benezenthiol SAM.

10.1.4 *In Situ* Monitoring of Individual DNA Hybridization

A label-free, PCR-free DNA sensor based on implementing molecular sentinels on NPGD. Taking the advantage of the ultrahigh SERS sensitivity of the substrates, which enables detection of individual Cy3-labeled DNA probes molecule, single DNA hybridization events have been observed by *in situ* monitoring the hybridization process.

The entire process takes about 90 min, while hybridization events can be detected within 10 min after adding 20 pM target oligonucleotides. Given the high sensitivity, rapid assay, robust SERS substrate, and simple detection system, this approach could find potential applications in point-of-care disease diagnosis and low-cost biological detection.

10.2 Future Directions

To advance Raman spectroscopy as a versatile and reliable technique in biological and biomedical applications, future development should focus on further improvement of the throughput. In line-scan Raman microscope, the performance is limited primarily on the hardware, for example, dimension of CCD detector and the back aperture of the objective. However in parallel Raman microscope system, several parameters can be optimized to improve the performance, such as replace current tube lens with a custom one that has a matched focal length with the microscope objective. Besides, possible approaches to improve the throughput include combing compressive sensing into pattern generation process. When the regions of interest are very sparse, relatively few incoherent observations are necessary to reconstruct the most significant non-zero regions. Thus it requires less laser spots, i.e., illumination patterns to image the sample, which may improve the throughput a lot. Another approach of interest is applying Hadamard transform algorithm to the parallel Raman microscope system.

To further improve the NPGD SERS substrates, several optimizations can be performed. Since the extinction peak shifts with the ratio of disk diameter and height, NPG disks with different diameter should be made to determine to an optimized dimension in order to achieve maximum enhancement.

In detection of DNA sequences by applying molecular sentinel on NPGD, lower target oligonucleotides should be used in order to determine the LOD. Currently in molecular sentinel method, a signal decrease due to hybridization is detected. This is known as "signal-off" scheme. In contrast, "signal-on" schemes detect signal increases due to hybridization processes and are able to achieve enormous signal gain as background observed in the absence of target is pushed toward to zero, thus a lower LOD can be achieved. It is possible to apply "signal-on" schemes on NPGD substrates by various designs of the DNA probe. Besides, since surface-enhance resonance Raman scattering (SERRS) is able to improve the sensitivity by 10^3-10^5 compared to SERS, further study on SERS label selection is preferred.

Mutations in DNA are the cause of a wide range of genetic diseases, including cystic fibrosis. Typically, mutations in DNA sequences are identified through differential denaturation, in which differences in structural stability are identified by thermally melting a sequence of interest and determining the melting temperature. Differential denaturation experiments also form a key aspect of forensic assays, where short tandem repeats (STRs) are used in DNA fingerprinting, and in the emerging field of pharmacogenetics, where patients who have a genetically pre-disposed risk of adverse side effects to certain medications can be identified. Since DNA mutations can be detected by thermal or electrochemical dehybridization, detection of the dehybridization process of dsDNA is expected using the NPGD substrate. A possible protocol using the same DNA sequences in Chapter 7 may be: (1) immobilization of dsDNA on NPGD and followed by MCH treatment, no SERS signal from Cy3 can be detected since the fluorophore is about 10 nm away from NPGD surface; (2) after applying voltage or

thermal heating, dehybridization results in formation of the loop-shaped probes, thus inducing strong SERS signal from Cy3. By determining different melting temperatures from the relation of Cy3 intensity and temperature, mutations can be identified.

References

1. R. S. Das and Y. K. Agrawal, "Raman spectroscopy: Recent advancements, techniques and applications," Vibrational Spectroscopy **57**, 163-176 (2011).
2. R. M. Jarvis and R. Goodacre, "Discrimination of bacteria using surface-enhanced Raman spectroscopy," Anal Chem **76**, 40-47 (2004).
3. K. A. Willets and R. P. Van Duyne, "Localized surface plasmon resonance spectroscopy and sensing," Annual review of physical chemistry **58**, 267-297 (2007).
4. P. L. Stiles, J. A. Dieringer, N. C. Shah, and R. P. Van Duyne, "Surface-enhanced Raman spectroscopy," Annual review of analytical chemistry **1**, 601-626 (2008).
5. M. Ivanda and K. Furic, "Line Focusing in Micro-Raman Spectroscopy," Appl Optics **31**, 6371-6375 (1992).
6. K. A. Christensen and M. D. Morris, "Hyperspectral Raman microscopic imaging using Powell lens line illumination," Applied Spectroscopy **52**, 1145-1147 (1998).
7. Y. Harada, T. Ota, D. Ping, Y. Yamaoka, K. Hamada, K. Fujita, and T. Takamatsu, "Imaging of anticancer agent distribution by a slit-scanning Raman microscope," in 2008), 685308-685308-685305.
8. K. Hamada, K. Fujita, N. I. Smith, M. Kobayashi, Y. Inouye, and S. Kawata, "Raman microscopy for dynamic molecular imaging of living cells," J Biomed Opt **13**(2008).
9. D. Cialla, A. Marz, R. Bohme, F. Theil, K. Weber, M. Schmitt, and J. Popp, "Surface-enhanced Raman spectroscopy (SERS): progress and trends," Analytical and bioanalytical chemistry **403**, 27-54 (2012).
10. R. L. McCreery, *Raman Spectroscopy for Chemical Analysis* (John Wiley & Sons, Inc., 2000).
11. M. Fleischmann, P. J. Hendra, and Mcquilla.Aj, "Raman-Spectra of Pyridine Adsorbed at a Silver Electrode," Chem Phys Lett **26**, 163-166 (1974).
12. D. L. Jeanmaire and R. P. Vanduyne, "Surface Raman Spectroelectrochemistry .1. Heterocyclic, Aromatic, and Aliphatic-Amines Adsorbed on Anodized Silver Electrode," J Electroanal Chem **84**, 1-20 (1977).
13. B. J. Kennedy, S. Spaeth, M. Dickey, and K. T. Carron, "Determination of the distance dependence and experimental effects for modified SERS substrates based on self-assembled monolayers formed using alkanethiols," J Phys Chem B **103**, 3640-3646 (1999).
14. G. J. Kovacs, R. O. Loutfy, P. S. Vincett, C. Jennings, and R. Aroca, "Distance Dependence of Sers Enhancement Factor from Langmuir-Blodgett Monolayers on Metal Island Films - Evidence for the Electromagnetic Mechanism," Langmuir **2**, 689-694 (1986).
15. A. Otto, I. Mrozek, H. Grabhorn, and W. Akemann, "Surface-Enhanced Raman-Scattering," J Phys-Condens Mat **4**, 1143-1212 (1992).
16. Z. Q. Tian, B. Ren, and D. Y. Wu, "Surface-enhanced Raman scattering: From noble to transition metals and from rough surfaces to ordered nanostructures," J Phys Chem B **106**, 9463-9483 (2002).

17. A. G. Brolo, Z. Jiang, and D. E. Irish, "The orientation of 2,2 '-bipyridine adsorbed at a SERS-active Au(111) electrode surface," J Electroanal Chem **547**, 163-172 (2003).
18. H. X. Xu, J. Aizpurua, M. Kall, and P. Apell, "Electromagnetic contributions to single-molecule sensitivity in surface-enhanced Raman scattering," Phys Rev E **62**, 4318-4324 (2000).
19. A. M. Michaels, M. Nirmal, and L. E. Brus, "Surface enhanced Raman spectroscopy of individual rhodamine 6G molecules on large Ag nanocrystals," J Am Chem Soc **121**, 9932-9939 (1999).
20. J. R. Lombardi and R. L. Birke, "A unified approach to surface-enhanced Raman spectroscopy," J Phys Chem C **112**, 5605-5617 (2008).
21. J. R. Lombardi and R. L. Birke, "A Unified View of Surface-Enhanced Raman Scattering," Accounts Chem Res **42**, 734-742 (2009).
22. M. Delhaye and P. Dhamelincourt, "Raman Microprobe and Microscope with Laser Excitation," J Raman Spectrosc **3**, 33-43 (1975).
23. K. Kaminska, J. Lefebvre, D. Austing, and P. Finnie, "Real-time global Raman imaging and optical manipulation of suspended carbon nanotubes," Physical Review B **73**(2006).
24. J. M. Amigo, J. Cruz, M. Bautista, S. Maspoch, J. Coello, and M. Blanco, "Study of pharmaceutical samples by NIR chemical-image and multivariate analysis," TrAC Trends in Analytical Chemistry **27**, 696-713 (2008).
25. H. R. Morris, C. C. Hoyt, and P. J. Treado, "Imaging Spectrometers for Fluorescence and Raman Microscopy - Acoustooptic and Liquid-Crystal Tunable Filters," Applied Spectroscopy **48**, 857-866 (1994).
26. P. J. Treado and M. D. Morris, "Hadamard-Transform Raman Imaging," Applied Spectroscopy **42**, 897-901 (1988).
27. J. Y. Ma and D. Ben-Amotz, "Rapid micro-Raman imaging using fiber-bundle image compression," Applied Spectroscopy **51**, 1845-1848 (1997).
28. J. C. George Turrell, *Raman Microscopy* (Academic Press, San Diego, 1996).
29. S. Schlucker, M. D. Schaeberle, S. W. Huffman, and I. W. Levin, "Raman microspectroscopy: A comparison of point, line, and wide-field imaging methodologies," Anal Chem **75**, 4312-4318 (2003).
30. J. Qi and W.-C. Shih, "Performance of line-scan Raman microscopy for high-throughput chemical imaging of cell population," Appl Optics **53**, 2881-2885 (2014).
31. S. Bernard, O. Beyssac, and K. Benzerara, "Raman Mapping Using Advanced Line-Scanning Systems: Geological Applications," Applied Spectroscopy **62**, 1180-1188 (2008).
32. S. Stewart, R. J. Priore, M. P. Nelson, and P. J. Treado, "Raman imaging," Annual review of analytical chemistry **5**, 337-360 (2012).
33. K. Hering, D. Cialla, K. Ackermann, T. Dorfer, R. Moller, H. Schneidewind, R. Mattheis, W. Fritzsche, P. Rosch, and J. Popp, "SERS: a versatile tool in chemical and biochemical diagnostics," Analytical and bioanalytical chemistry **390**, 113-124 (2008).
34. P. F. Liao and A. Wokaun, "Lightning Rod Effect in Surface Enhanced Raman-Scattering," J Chem Phys **76**, 751-752 (1982).

35. L. Gunnarsson, E. J. Bjerneld, H. Xu, S. Petronis, B. Kasemo, and M. Käll, "Interparticle coupling effects in nanofabricated substrates for surface-enhanced Raman scattering," Applied Physics Letters **78**, 802 (2001).
36. D. P. Tsai, J. Kovacs, Z. H. Wang, M. Moskovits, V. M. Shalaev, J. S. Suh, and R. Botet, "Photon Scanning-Tunneling-Microscopy Images of Optical-Excitations of Fractal Metal Colloid Clusters," Phys Rev Lett **72**, 4149-4152 (1994).
37. P. Zhang, T. L. Haslett, C. Douketis, and M. Moskovits, "Mode localization in self-affine fractal interfaces observed by near-field microscopy," Physical Review B **57**, 15513-15518 (1998).
38. X. M. Lin, Y. Cui, Y. H. Xu, B. Ren, and Z. Q. Tian, "Surface-enhanced Raman spectroscopy: substrate-related issues," Analytical and bioanalytical chemistry **394**, 1729-1745 (2009).
39. C. Jennings, R. Aroca, A. M. Hor, and R. O. Loutfy, "SURFACE-ENHANCED RAMAN-SCATTERING FROM COPPER AND ZINC PHTHALOCYANINE COMPLEXES BY SILVER AND INDIUM ISLAND FILMS," Anal Chem **56**, 2033-2035 (1984).
40. R. P. Vanduyne, J. C. Hulteen, and D. A. Treichel, "ATOMIC-FORCE MICROSCOPY AND SURFACE-ENHANCED RAMAN-SPECTROSCOPY .1. AG ISLAND FILMS AND AG FILM OVER POLYMER NANOSPHERE SURFACES SUPPORTED ON GLASS," J Chem Phys **99**, 2101-2115 (1993).
41. T. Vo-Dinh, "Surface-enhanced Raman spectroscopy using metallic nanostructures," Trac-Trends in Analytical Chemistry **17**, 557-582 (1998).
42. E. Vogel, W. Kiefer, V. Deckert, and D. Zeisel, "Laser-deposited Silver Island films: An investigation of their structure, optical properties and SERS activity," J Raman Spectrosc **29**, 693-702 (1998).
43. Y. Jiao, D. S. Koktysh, N. Phambu, and S. M. Weiss, "Dual-mode sensing platform based on colloidal gold functionalized porous silicon," Applied Physics Letters **97**(2010).
44. T. L. Williamson, X. Y. Guo, A. Zukoski, A. Sood, D. J. Diaz, and P. W. Bohn, "Porous GaN as a template to produce surface-enhanced Raman scattering-active surfaces," J Phys Chem B **109**, 20186-20191 (2005).
45. L. H. Qian, X. Q. Yan, T. Fujita, A. Inoue, and M. W. Chen, "Surface enhanced Raman scattering of nanoporous gold: Smaller pore sizes stronger enhancements," Applied Physics Letters **90**, 153120 (2007).
46. Y. Jiao, J. D. Ryckman, P. N. Ciesielski, C. A. Escobar, G. K. Jennings, and S. M. Weiss, "Patterned nanoporous gold as an effective SERS template," Nanotechnology **22**, 295302 (2011).
47. L. Zhang, X. Y. Lang, A. Hirata, and M. W. Chen, "Wrinkled Nanoporous Gold Films with Ultrahigh Surface-Enhanced Raman Scattering Enhancement," Acs Nano **5**, 4407-4413 (2011).
48. S. M. Nie and S. R. Emery, "Probing single molecules and single nanoparticles by surface-enhanced Raman scattering," Science **275**, 1102-1106 (1997).
49. N. R. Yaffe and E. W. Blanch, "Effects and anomalies that can occur in SERS spectra of biological molecules when using a wide range of aggregating agents for hydroxylamine-reduced and citrate-reduced silver colloids," Vibrational Spectroscopy **48**, 196-201 (2008).

50. S. J. Oldenburg, R. D. Averitt, S. L. Westcott, and N. J. Halas, "Nanoengineering of optical resonances," Chem Phys Lett **288**, 243-247 (1998).
51. X. Y. Zhang, J. Zhao, A. V. Whitney, J. W. Elam, and R. P. Van Duyne, "Ultrastable substrates for surface-enhanced Raman spectroscopy: Al2O3 overlayers fabricated by atomic layer deposition yield improved anthrax biomarker detection," J Am Chem Soc **128**, 10304-10309 (2006).
52. T. Vo-Dinh, M. Y. K. Hiromoto, G. M. Begun, and R. L. Moody, "Surface-Enhanced Raman Spectrometry for Trace Organic-Analysis," Anal Chem **56**, 1667-1670 (1984).
53. A. J. Haes, L. Chang, W. L. Klein, and R. P. Van Duyne, "Detection of a biomarker for Alzheimer's disease from synthetic and clinical samples using a nanoscale optical biosensor," J Am Chem Soc **127**, 2264-2271 (2005).
54. D. Cialla, R. Siebert, U. Hubner, R. Moller, H. Schneidewind, R. Mattheis, J. Petschulat, A. Tunnermann, T. Pertsch, B. Dietzek, and J. Popp, "Ultrafast plasmon dynamics and evanescent field distribution of reproducible surface-enhanced Raman-scattering substrates," Analytical and bioanalytical chemistry **394**, 1811-1818 (2009).
55. G. J. Puppels, F. F. M. Demul, C. Otto, J. Greve, M. Robertnicoud, D. J. Arndtjovin, and T. M. Jovin, "Studying Single Living Cells and Chromosomes by Confocal Raman Microspectroscopy," Nature **347**, 301-303 (1990).
56. C. Matthaus, S. Boydston-White, M. Miljkovic, M. Romeo, and M. Diem, "Raman and infrared microspectral imaging of mitotic cells," Applied Spectroscopy **60**, 1-8 (2006).
57. L. Hartsuiker, N. J. L. Zeijen, L. Terstappen, and C. Otto, "A comparison of breast cancer tumor cells with varying expression of the Her2/neu receptor by Raman microspectroscopic imaging," Analyst **135**, 3220-3226 (2010).
58. A. S. Haka, K. E. Shafer-Peltier, M. Fitzmaurice, J. Crowe, R. R. Dasari, and M. S. Feld, "Diagnosing breast cancer by using Raman spectroscopy," P Natl Acad Sci USA **102**, 12371-12376 (2005).
59. V. V. Pully, A. T. M. Lenferink, and C. Otto, "Time-lapse Raman imaging of single live lymphocytes," J Raman Spectrosc **42**, 167-173 (2011).
60. B. D. Beier, R. G. Quivey, and A. J. Berger, "Identification of different bacterial species in biofilms using confocal Raman microscopy," J Biomed Opt **15**(2010).
61. T. Chernenko, C. Matthaus, L. Milane, L. Quintero, M. Amiji, and M. Diem, "Label-Free Raman Spectral Imaging of Intracellular Delivery and Degradation of Polymeric Nanoparticle Systems," Acs Nano **3**, 3552-3559 (2009).
62. Y. Y. Huang, C. M. Beal, W. W. Cai, R. S. Ruoff, and E. M. Terentjev, "Micro-Raman Spectroscopy of Algae: Composition Analysis and Fluorescence Background Behavior," Biotechnology and Bioengineering **105**, 889-898 (2010).
63. T. L. Weiss, H. J. Chun, S. Okada, S. Vitha, A. Holzenburg, J. Laane, and T. P. Devarenne, "Raman Spectroscopy Analysis of Botryococcene Hydrocarbons from the Green Microalga Botryococcus braunii," Journal of Biological Chemistry **285**, 32458-32466 (2010).
64. C. L. Evans, E. O. Potma, M. Puoris'haag, D. Cote, C. P. Lin, and X. S. Xie, "Chemical imaging of tissue in vivo with video-rate coherent anti-Stokes Raman scattering microscopy," P Natl Acad Sci USA **102**, 16807-16812 (2005).

65. C. W. Freudiger, W. Min, B. G. Saar, S. Lu, G. R. Holtom, C. W. He, J. C. Tsai, J. X. Kang, and X. S. Xie, "Label-Free Biomedical Imaging with High Sensitivity by Stimulated Raman Scattering Microscopy," Science **322**, 1857-1861 (2008).
66. J. Qi, P. Motwani, M. Gheewala, C. Brennan, J. C. Wolfe, and W.-C. Shih, "Surface-enhanced Raman spectroscopy with monolithic nanoporous gold disk substrates," Nanoscale **5**, 4105-4109 (2013).
67. B. R. Masters and A. A. Thaer, "Real-time scanning slit confocal microscopy of the in-vivo human cornea," Appl Optics **33**, 695-701 (1994).
68. M. B. Sinclair, J. A. Timlin, D. M. Haaland, and M. Werner-Washburne, "Design, construction, characterization, and application of a hyperspectral microarray scanner," Appl Optics **43**, 2079-2088 (2004).
69. A. M. K. Enejder, T. G. Scecina, J. Oh, M. Hunter, W. C. Shih, S. Sasic, G. L. Horowitz, and M. S. Feld, "Raman spectroscopy for noninvasive glucose measurements," J Biomed Opt **10**, 031114 (2005).
70. A. D. Gift, J. Y. Ma, K. S. Haber, B. L. McClain, and D. Ben-Amotz, "Near-infrared Raman imaging microscope based on fiber-bundle image compression," J Raman Spectrosc **30**, 757-765 (1999).
71. M. Okuno and H. Hamaguchi, "Multifocus confocal Raman microspectroscopy for fast multimode vibrational imaging of living cells," Optics Letters **35**, 4096-4098 (2010).
72. W. C. Shih, K. L. Bechtel, and M. S. Feld, "Constrained regularization: Hybrid method for multivariate calibration," Anal Chem **79**, 234-239 (2007).
73. W. C. Shih, K. L. Bechtel, and M. S. Feld, "Intrinsic Raman spectroscopy for quantitative biological spectroscopy Part I: Theory and simulations," Optics Express **16**, 12726-12736 (2008).
74. J. Qi, J. Li, and W.-C. Shih, "High-speed hyperspectral Raman imaging for label-free compositional microanalysis," Biomedical Optics Express **4**, 2376-2382 (2013).
75. J. Qi and W.-C. Shih, "Parallel Raman Microspectroscopy using Programmable Multi-point Illumination," Optics Letters **37**, 1289-1291 (2012).
76. O. Dalby, D. Butler, and J. W. Birkett, "Analysis of gunshot residue and associated materials-a review," Journal of forensic sciences **55**, 924-943 (2010).
77. H. Meng and B. Caddy, "Gunshot residue analysis-a review," Journal of forensic sciences **42**, 553-570 (1997).
78. F. Saverio Romolo and P. Margot, "Identification of gunshot residue: a critical review," Forensic Science International **119**, 195-211 (2001).
79. D. Laza, B. Nys, J. D. Kinder, K. D. Mesmaeker, and C. Moucheron, "Development of a Quantitative LC-MS/MS Method for the Analysis of Common Propellant Powder Stabilizers in Gunshot Residue," Journal of forensic sciences **52**, 842-850 (2007).
80. A. D. Becke, "Density-functional exchange-energy approximation with correct asymptotic behavior," Physical Review A **38**, 3098 (1988).
81. A. D. Becke, "Density-functional thermochemistry. III. The role of exact exchange," The Journal of Chemical Physics **98**, 5648 (1993).

82. J. Baker, A. A. Jarzecki, and P. Pulay, "Direct scaling of primitive valence force constants: An alternative approach to scaled quantum mechanical force fields," The Journal of Physical Chemistry A **102**, 1412-1424 (1998).
83. J. Bueno and I. K. Lednev, "Attenuated Total Reflectance-FT-IR Imaging for Rapid and Automated Detection of Gunshot Residue," Anal Chem **86**, 3389–3396 (2014).
84. Y. Zhang, H. Hong, and W. Cai, "Imaging with Raman spectroscopy," Current pharmaceutical biotechnology **11**, 654 (2010).
85. L. Kong, Z. P, P. Setlow, and Y. Li, "Multifocus confocal Raman microspectroscopy for rapid single-particle analysis," J Biomed Opt **16**, 120503 (2011).
86. R. Liu, D. S. Taylor, D. L. Matthews, and J. W. Chan, "Parallel Analysis of Individual Biological Cells Using Multifocal Laser Tweezers Raman Spectroscopy," Applied Spectroscopy **64**, 1308-1310 (2010).
87. J. Qi, P. Motwani, J. Wolfe, and W. Shih, "High-throughput Raman and Surface-enhanced Raman Microscopy," in *SPIE Photonics West,* (SPIE, San Francisco, 2012).
88. V. Nikolenko, B. O. Watson, R. Araya, A. Woodruff, D. S. Peterka, and R. Yuste, "SLM microscopy: scanless two-photon imaging and photostimulation with spatial light modulators," Front Neural Circuit **2**(2008).
89. J. E. Curtis, B. A. Koss, and D. G. Grier, "Dynamic holographic optical tweezers," Optics Communications **207**, 169-175 (2002).
90. J. Qi and W. C. Shih, "Parallel Raman microspectroscopy using programmable multipoint illumination," Optics Letters **37**, 1289-1291 (2012).
91. S. Stockel, S. Meisel, R. Bohme, M. Elschner, P. Rosch, and J. Popp, "Effect of supplementary manganese on the sporulation of Bacillus endospores analysed by Raman spectroscopy," J Raman Spectrosc **40**, 1469-1477 (2009).
92. D. I. Ellis and R. Goodacre, "Metabolic fingerprinting in disease diagnosis: biomedical applications of infrared and Raman spectroscopy," Analyst **131**, 875-885 (2006).
93. R. Postma and F. H. Schroder, "Screening for prostate cancer," Eur J Cancer **41**, 825-833 (2005).
94. R. S. Punglia, A. V. D'Amico, W. J. Catalona, K. A. Roehl, and K. M. Kuntz, "Effect of verification bias on screening for prostate cancer by measurement of prostate-specific antigen," New Engl J Med **349**, 335-342 (2003).
95. B. E. Sirovich, L. M. Schwartz, and S. Woloshin, "Screening men for prostate and colorectal cancer in the United States - Does practice reflect the evidence?," Jama-J Am Med Assoc **289**, 1414-1420 (2003).
96. T. A. Stamey, M. Caldwell, J. E. McNeal, R. Nolley, M. Hemenez, and J. Downs, "Re: The prostate specific antigen era in the United States is over for prostate cancer: What happened in the last 20 years? Reply," J Urology **174**, 1155-1156 (2005).
97. M. S. Anscher, P. Jones, L. R. Prosnitz, W. Blackstock, M. Hebert, R. Reddick, A. Tucker, R. Dodge, G. Leight, J. D. Iglehart, and J. Rosenman, "Local failure and margin status in early-stage breast carcinoma treated with conservation surgery and radiation therapy," Annals of surgery **218**, 22-28 (1993).

98. D. H. Roukos, A. M. Kappas, and N. J. Agnantis, "Perspectives and risks of breast-conservation therapy for breast cancer," Annals of surgical oncology **10**, 718-721 (2003).
99. N. Lawrentschuk, A. Evans, J. Srigley, J. L. Chin, B. Bora, A. Hunter, R. McLeod, and N. E. Fleshner, "Surgical margin status among men with organ-confined (pT2) prostate cancer: a population-based study," Cuaj-Can Urol Assoc **5**, 161-166 (2011).
100. W. C. Lin, S. A. Toms, M. Johnson, E. D. Jansen, and A. Mahadevan-Jansen, "In vivo brain tumor demarcation using optical spectroscopy," Photochem Photobiol **73**, 396-402 (2001).
101. M. H. Katz, E. A. Choi, and R. E. Pollock, "Current concepts in multimodality therapy for retroperitoneal sarcoma," Expert Rev Anticancer Ther **7**, 159-168 (2007).
102. C. C. Park, M. Mitsumori, A. Nixon, A. Recht, J. Connolly, R. Gelman, B. Silver, S. Hetelekidis, A. Abner, J. R. Harris, and S. J. Schnitt, "Outcome at 8 years after breast-conserving surgery and radiation therapy for invasive breast cancer: Influence of margin status and systemic therapy on local recurrence," J Clin Oncol **18**, 1668-1675 (2000).
103. J. Walls, F. Knox, A. D. Baildam, D. L. Asbury, R. E. Mansel, and N. J. Bundred, "Can Preoperative Factors Predict for Residual Malignancy after Breast Biopsy for Invasive Cancer," Ann Roy Coll Surg **77**, 248-251 (1995).
104. I. J. Bigio, S. G. Bown, G. Briggs, C. Kelley, S. Lakhani, D. Pickard, P. M. Ripley, I. G. Rose, and C. Saunders, "Diagnosis of breast cancer using elastic-scattering spectroscopy: preliminary clinical results," J Biomed Opt **5**, 221-228 (2000).
105. C. A. Patil, N. Bosschaart, M. D. Keller, T. G. van Leeuwen, and A. Mahadevan-Jansen, "Combined Raman spectroscopy and optical coherence tomography device for tissue characterization," Opt Lett **33**, 1135-1137 (2008).
106. C. A. Patil, J. Kalkman, D. J. Faber, J. S. Nyman, T. G. van Leeuwen, and A. Mahadevan-Jansen, "Integrated system for combined Raman spectroscopy-spectral domain optical coherence tomography," J Biomed Opt **16**, 011007 (2011).
107. C. A. Patil, H. Kirshnamoorthi, D. L. Ellis, T. G. van Leeuwen, and A. Mahadevan-Jansen, "A clinical instrument for combined raman spectroscopy-optical coherence tomography of skin cancers," Lasers in surgery and medicine **43**, 143-151 (2011).
108. M. G. Ghosn, V. V. Tuchin, and K. V. Larin, "Nondestructive quantification of analyte diffusion in cornea and sclera using optical coherence tomography," Investigative ophthalmology & visual science **48**, 2726-2733 (2007).
109. Z. M. Zhang, S. Chen, and Y. Z. Liang, "Baseline correction using adaptive iteratively reweighted penalized least squares," Analyst **135**, 1138-1146 (2010).
110. L. Yi and Y. F. Zheng, "One-against-all multi-class SVM classification using reliability measures," in *Neural Networks, 2005. IJCNN '05. Proceedings. 2005 IEEE International Joint Conference on*, 2005), 849-854 vol. 842.
111. W. F. Cheong, S. A. Prahl, and A. J. Welch, "A review of the optical properties of biological tissues," Quantum Electronics, IEEE Journal of **26**, 2166-2185 (1990).

112. A. Shen, B. Zhang, J. Ping, W. Xie, P. Donfack, S.-J. Baek, X. Zhou, H. Wang, A. Materny, and J. Hu, "In vivostudy on the protection of indole-3-carbinol (I3C) against the mouse acute alcoholic liver injury by micro-Raman spectroscopy," J Raman Spectrosc **40**, 550-555 (2009).
113. N. Huang, M. Short, J. Zhao, H. Wang, H. Lui, M. Korbelik, and H. Zeng, "Full range characterization of the Raman spectra of organs in a murine model," Optics Express **19**, 22892-22909 (2011).
114. N. Stone, C. Kendall, N. Shepherd, P. Crow, and H. Barr, "Near-infrared Raman spectroscopy for the classification of epithelial pre-cancers and cancers," J Raman Spectrosc **33**, 564-573 (2002).
115. A. W. Auner, R. E. Kast, R. Rabah, J. M. Poulik, and M. D. Klein, "Conclusions and data analysis: a 6-year study of Raman spectroscopy of solid tumors at a major pediatric institute," Pediatric surgery international **29**, 129-140 (2013).
116. A. Mahadevan-Jansen, M. F. Mitchell, N. Ramanujamf, A. Malpica, S. Thomsen, U. Utzinger, and R. Richards-Kortumt, "Near-Infrared Raman Spectroscopy for In Vitro Detection of Cervical Precancers," Photochem Photobiol **68**, 123-132 (1998).
117. C. H. Liu, B. B. Das, W. L. S. Glassman, G. C. Tang, K. M. Yoo, H. R. Zhu, D. L. Akins, S. S. Lubicz, J. Cleary, R. Prudente, E. Celmer, A. Caron, and R. R. Alfano, "Raman, fluorescence, and time-resolved light scattering as optical diagnostic techniques to separate diseased and normal biomedical media," Journal of photochemistry and photobiology. B, Biology **16**, 187-209 (1992).
118. Z. Huang, H. Lui, D. I. McLean, M. Korbelik, and H. Zeng, "Raman spectroscopy in combination with background near-infrared autofluorescence enhances the in vivo assessment of malignant tissues," Photochem Photobiol **81**, 1219-1226 (2005).
119. E. F. Carbajal, S. A. Baranov, V. G. R. Manne, E. D. Young, A. J. Lazar, D. C. Lev, R. E. Pollock, and K. V. Larin, "Revealing retroperitoneal liposarcoma morphology using optical coherence tomography," J Biomed Opt **16**(2011).
120. F. Loubignac, C. Bourtoul, and F. Chapel, "Myxoid liposarcoma: a rare soft-tissue tumor with a misleading benign appearance," World J Surg Oncol **7**, 42 (2009).
121. J. Qi, J. T. Li, and W. C. Shih, "High-speed hyperspectral Raman imaging for label-free compositional microanalysis," Biomedical Optics Express **4**, 2376-2382 (2013).
122. R. Manoharan, Y. Wang, and M. S. Feld, "Histochemical analysis of biological tissues using Raman spectroscopy," Spectrochim Acta A **52**, 215-249 (1996).
123. J. S. Thakur, H. B. Dai, G. K. Serhatkulu, R. Naik, V. M. Naik, A. Cao, A. Pandya, G. W. Auner, R. Rabah, M. D. Klein, and C. Freeman, "Raman spectral signatures of mouse mammary tissue and associated lymph nodes: normal, tumor and mastitis," J Raman Spectrosc **38**, 127-134 (2007).
124. N. Y. Huang, M. Short, J. H. Zhao, H. Q. Wang, H. Lui, M. Korbelik, and H. S. Zeng, "Full range characterization of the Raman spectra of organs in a murine model," Optics Express **19**, 22892-22909 (2011).
125. J. N. Anker, W. P. Hall, O. Lyandres, N. C. Shah, J. Zhao, and R. P. Van Duyne, "Biosensing with plasmonic nanosensors," Nat. Mater. **7**, 442-453 (2008).

126. M. Moskovits, "Surface-enhanced spectroscopy," Reviews of Modern Physics **57**, 783-826 (1985).
127. M. Moskovits, "Surface-enhanced Raman spectroscopy: a brief retrospective," J Raman Spectrosc **36**, 485-496 (2005).
128. K. A. Willets and R. P. Van Duyne, "Localized surface plasmon resonance spectroscopy and sensing," Annu Rev Phys Chem **58**, 267-297 (2007).
129. L. Maya, "Sputtered gold films for surface-enhanced Raman scattering," Journal of Vacuum Science & Technology A: Vacuum, Surfaces, and Films **15**, 238 (1997).
130. I. Doron-Mor, H. Cohen, Z. Barkay, A. Shanzer, A. Vaskevich, and I. Rubinstein, "Sensitivity of transmission surface plasmon resonance (T-SPR) spectroscopy: self-assembled multilayers on evaporated gold island films," Chemistry **11**, 5555-5562 (2005).
131. G. Kalyuzhny, A. Vaskevich, G. Ashkenasy, A. Shanzer, and I. Rubinstein, "UV/vis spectroscopy of metalloporphyrin and metallophthalocyanine monolayers self-assembled on ultrathin gold films," J Phys Chem B **104**, 8238-8244 (2000).
132. A. B. Tesler, B. M. Maoz, Y. Feldman, A. Vaskevich, and I. Rubinstein, "Solid-State Thermal Dewetting of Just-Percolated Gold Films Evaporated on Glass: Development of the Morphology and Optical Properties," The Journal of Physical Chemistry C **117**, 11337-11346 (2013).
133. A. Merlen, V. Gadenne, J. Romann, V. Chevallier, L. Patrone, and J. C. Valmalette, "Surface enhanced Raman spectroscopy of organic molecules deposited on gold sputtered substrates," Nanotechnology **20**, 215705 (2009).
134. A. Merlen, F. Lagugne-Labarthet, and E. Harte, "Surface-Enhanced Raman and Fluorescence Spectroscopy of Dye Molecules Deposited on Nanostructured Gold Surfaces," J Phys Chem C **114**, 12878-12884 (2010).
135. Z. W. Liu, W. B. Hou, P. Pavaskar, M. Aykol, and S. B. Cronin, "Plasmon Resonant Enhancement of Photocatalytic Water Splitting Under Visible Illumination," Nano Lett **11**, 1111-1116 (2011).
136. P. Pavaskar, J. Theiss, and S. B. Cronin, "Plasmonic hot spots: nanogap enhancement vs. focusing effects from surrounding nanoparticles," Optics Express **20**, 14656-14662 (2012).
137. M. E. Abdelsalam, P. N. Bartlett, J. J. Baumberg, S. Cintra, T. A. Kelf, and A. E. Russell, "Electrochemical SERS at a structured gold surface," Electrochem. Commun. **7**, 740-744 (2005).
138. B. Brian, B. Sepulveda, Y. Alaverdyan, L. M. Lechuga, and M. Kall, "Sensitivity enhancement of nanoplasmonic sensors in low refractive index substrates," Optics Express **17**, 2015-2023 (2009).
139. M. D. Malinsky, K. L. Kelly, G. C. Schatz, and R. P. Van Duyne, "Chain length dependence and sensing capabilities of the localized surface plasmon resonance of silver nanoparticles chemically modified with alkanethiol self-assembled monolayers," J Am Chem Soc **123**, 1471-1482 (2001).
140. M. R. Gartia, Z. Xu, E. Behymer, H. Nguyen, J. A. Britten, C. Larson, R. Miles, M. Bora, A. S. Chang, T. C. Bond, and G. L. Liu, "Rigorous surface enhanced

Raman spectral characterization of large-area high-uniformity silver-coated tapered silica nanopillar arrays," Nanotechnology **21**, 395701 (2010).
141. C. Y. Wu, C. C. Huang, J. S. Jhang, A. C. Liu, C. C. Chiang, M. L. Hsieh, P. J. Huang, D. T. Le, Q. M. Le, T. S. Yang, L. K. Chau, H. C. Kan, and C. C. Hsu, "Hybrid surface-enhanced Raman scattering substrate from gold nanoparticle and photonic crystal: Maneuverability and uniformity of Raman spectra," Optics Express **17**, 21522-21529 (2009).
142. J. M. Chalmers and P. R. Griffiths, *Handbook of vibrational spectroscopy*, p. 5 volumes.
143. S. T. McCain, M. E. Gehm, Y. Wang, N. P. Pitsianis, and D. J. Brady, "Coded aperture Raman spectroscopy for quantitative measurements of ethanol in a tissue phantom," Applied Spectroscopy **60**, 663-671 (2006).
144. W. C. Shih, K. L. Bechtel, and M. S. Feld, *Handbook Of Optical Sensing Of Glucose In Biological Fluids And Tissues* (2008).
145. C. L. Haynes, A. D. McFarland, and R. P. Van Duyne, "Surface-enhanced Raman spectroscopy," Anal Chem **77**, 338a-346a (2005).
146. K. Kneipp, Y. Wang, H. Kneipp, L. T. Perelman, I. Itzkan, R. Dasari, and M. S. Feld, "Single molecule detection using surface-enhanced Raman scattering (SERS)," Phys Rev Lett **78**, 1667-1670 (1997).
147. L. Malfatti, P. Falcaro, B. Marmiroli, H. Amenitsch, M. Piccinini, A. Falqui, and P. Innocenzi, "Nanocomposite mesoporous ordered films for lab-on-chip intrinsic surface enhanced Raman scattering detection," Nanoscale **3**, 3760-3766 (2011).
148. J. P. Camden, J. A. Dieringer, J. Zhao, and R. P. Van Duyne, "Controlled Plasmonic Nanostructures for Surface-Enhanced Spectroscopy and Sensing," Accounts Chem Res **41**, 1653-1661 (2008).
149. D. Gloria, J. J. Gooding, G. Moran, and D. B. Hibbert, "Electrochemically fabricated three dimensional nano-porous gold films optimised for surface enhanced Raman scattering," J Electroanal Chem **656**, 114-119 (2011).
150. S. O. Kucheyev, J. R. Hayes, J. Biener, T. Huser, C. E. Talley, and A. V. Hamza, "Surface-enhanced Raman scattering on nanoporous Au," Applied Physics Letters **89**(2006).
151. A. Wittstock, V. Zielasek, J. Biener, C. M. Friend, and M. Baumer, "Nanoporous Gold Catalysts for Selective Gas-Phase Oxidative Coupling of Methanol at Low Temperature," Science **327**, 319-322 (2010).
152. Y. Yang, Y. Xia, W. Huang, J. Zheng, and Z. Li, "Fabrication of nano-network gold films via anodization of gold electrode and their application in SERS," J Solid State Electrochem **16**, 1733-1739 (2012).
153. J. Biener, G. W. Nyce, A. M. Hodge, M. M. Biener, A. V. Hamza, and S. A. Maier, "Nanoporous plasmonic metamaterials," Adv Mater **20**, 1211-1217 (2008).
154. X. Y. Lang, L. H. Qian, P. F. Guan, J. Zi, and M. W. Chen, "Localized surface plasmon resonance of nanoporous gold," Applied Physics Letters **98**(2011).
155. Y. Jiao, J. D. Ryckman, P. N. Ciesielski, C. A. Escobar, G. K. Jennings, and S. M. Weiss, "Patterned nanoporous gold as an effective SERS template," Nanotechnology **22**(2011).
156. J. S. Wi, S. Tominaka, K. Uosaki, and T. Nagao, "Porous gold nanodisks with multiple internal hot spots," Phys Chem Chem Phys **14**, 9131-9136 (2012).

157. S.-W. Lee, K.-S. Lee, J. Ahn, J.-J. Lee, M.-G. Kim, and Y.-B. Shin, "Highly Sensitive Biosensing Using Arrays of Plasmonic Au Nanodisks Realized by Nanoimprint Lithography," Acs Nano **5**, 897-904 (2011).
158. Q. Yu, P. Guan, D. Qin, G. Golden, and P. M. Wallace, "Inverted Size-Dependence of Surface-Enhanced Raman Scattering on Gold Nanohole and Nanodisk Arrays," Nano Lett **8**, 1923-1928 (2008).
159. D. Kramer, R. N. Viswanath, and J. Weissmüller, "Surface-Stress Induced Macroscopic Bending of Nanoporous Gold Cantilevers," Nano Lett **4**, 793-796 (2004).
160. E. Seker, Y. Berdichevsky, M. R. Begley, M. L. Reed, K. J. Staley, and M. L. Yarmush, "The fabrication of low-impedance nanoporous gold multiple-electrode arrays for neural electrophysiology studies," Nanotechnology **21**, 7 (2010).
161. M. D. Scanlon, U. Salaj-Kosla, S. Belochapkine, D. MacAodha, D. Leech, Y. Ding, and E. Magner, "Characterization of Nanoporous Gold Electrodes for Bioelectrochemical Applications," Langmuir **28**, 2251-2261 (2011).
162. P. B. Johnson and R. W. Christy, "Optical Constants of the Noble Metals," Physical Review B **6**, 4370-4379 (1972).
163. R. L. Aggarwal, L. W. Farrar, E. D. Diebold, and D. L. Polla, "Measurement of the absolute Raman scattering cross section of the 1584-cm(-1) band of benzenethiol and the surface-enhanced Raman scattering cross section enhancement factor for femtosecond laser-nanostructured substrates," J Raman Spectrosc **40**, 1331-1333 (2009).
164. J. Qi, P. Motwani, J. C. Wolfe, and W. C. Shih, "High-throughput Raman and Surface-enhanced Raman Microscopy," Biomedical Vibrational Spectroscopy V: Advances in Research and Industry **8219**, 6 (2012).
165. C. L. Haynes and R. P. Van Duyne, "Nanosphere Lithography: A Versatile Nanofabrication Tool for Studies of Size-Dependent Nanoparticle Optics," The Journal of Physical Chemistry B **105**, 5599-5611 (2001).
166. H.-Y. Wu, C. J. Choi, and B. T. Cunningham, "Sers: Plasmonic Nanogap-Enhanced Raman Scattering Using a Resonant Nanodome Array (Small 18/2012)," Small **8**, 2769-2769 (2012).
167. Y. D. Yin and X. S. Zhao, "Kinetics and Dynamics of DNA Hybridization," Accounts Chem Res **44**, 1172-1181 (2011).
168. A. Sassolas, B. D. Leca-Bouvier, and L. J. Blum, "DNA biosensors and microarrays," Chemical Reviews **108**, 109-139 (2008).
169. M. Kinjo and R. Rigler, "Ultrasensitive Hybridization Analysis Using Fluorescence Correlation Spectroscopy," Nucleic Acids Res **23**, 1795-1799 (1995).
170. B. S. Gaylord, A. J. Heeger, and G. C. Bazan, "DNA detection using water-soluble conjugated polymers and peptide nucleic acid probes," P Natl Acad Sci USA **99**, 10954-10957 (2002).
171. O. P. Kallioniemi, A. Kallioniemi, W. Kurisu, A. Thor, L. C. Chen, H. S. Smith, F. M. Waldman, D. Pinkel, and J. W. Gray, "Erbb2 Amplification in Breast-Cancer Analyzed by Fluorescence Insitu Hybridization," P Natl Acad Sci USA **89**, 5321-5325 (1992).

172. D. J. Lockhart, H. L. Dong, M. C. Byrne, M. T. Follettie, M. V. Gallo, M. S. Chee, M. Mittmann, C. W. Wang, M. Kobayashi, H. Horton, and E. L. Brown, "Expression monitoring by hybridization to high-density oligonucleotide arrays," Nat Biotechnol **14**, 1675-1680 (1996).
173. S. Tyagi and F. R. Kramer, "Molecular beacons: Probes that fluoresce upon hybridization," Nat Biotechnol **14**, 303-308 (1996).
174. H. C. Yeh, J. Sharma, J. J. Han, J. S. Martinez, and J. H. Werner, "A DNA-Silver Nanocluster Probe That Fluoresces upon Hybridization," Nano Lett **10**, 3106-3110 (2010).
175. X. W. Zhuang, L. E. Bartley, H. P. Babcock, R. Russell, T. J. Ha, D. Herschlag, and S. Chu, "A single-molecule study of RNA catalysis and folding," Science **288**, 2048-+ (2000).
176. G. Yao, X. H. Fang, H. Yokota, T. Yanagida, and W. H. Tan, "Monitoring molecular beacon DNA probe hybridization at the single-molecule level," Chem-Eur J **9**, 5686-5692 (2003).
177. H. I. Peng, C. M. Strohsahl, and B. L. Miller, "Microfluidic nanoplasmonic-enabled device for multiplex DNA detection," Lab on a chip **12**, 1089-1093 (2012).
178. Y. Chen, K. Munechika, and D. S. Ginger, "Dependence of fluorescence intensity on the spectral overlap between fluorophores and plasmon resonant single silver nanoparticles," Nano Lett **7**, 690-696 (2007).
179. Y. Shen, J. H. Zhou, T. R. Liu, Y. T. Tao, R. B. Jiang, M. X. Liu, G. H. Xiao, J. H. Zhu, Z. K. Zhou, X. H. Wang, C. J. Jin, and J. F. Wang, "Plasmonic gold mushroom arrays with refractive index sensing figures of merit approaching the theoretical limit," Nature Communications **4**(2013).
180. C. Sonnichsen, B. M. Reinhard, J. Liphardt, and A. P. Alivisatos, "A molecular ruler based on plasmon coupling of single gold and silver nanoparticles," Nat Biotechnol **23**, 741-745 (2005).
181. R. Gordon, D. Sinton, K. L. Kavanagh, and A. G. Brolo, "A new generation of sensors based on extraordinary optical transmission," Accounts Chem Res **41**, 1049-1057 (2008).
182. A. A. Yanik, M. Huang, O. Kamohara, A. Artar, T. W. Geisbert, J. H. Connor, and H. Altug, "An Optofluidic Nanoplasmonic Biosensor for Direct Detection of Live Viruses from Biological Media," Nano Lett **10**, 4962-4969 (2010).
183. T. G. Drummond, M. G. Hill, and J. K. Barton, "Electrochemical DNA sensors," Nat Biotechnol **21**, 1192-1199 (2003).
184. J. Wang, G. D. Liu, and A. Merkoci, "Electrochemical coding technology for simultaneous detection of multiple DNA targets," J Am Chem Soc **125**, 3214-3215 (2003).
185. W. Ma, H. Kuang, L. G. Xu, L. Ding, C. L. Xu, L. B. Wang, and N. A. Kotov, "Attomolar DNA detection with chiral nanorod assemblies," Nature Communications **4**(2013).
186. P. Ross, L. Hall, I. Smirnov, and L. Haff, "High level multiplex genotyping by MALDI-TOF mass spectrometry," Nat Biotechnol **16**, 1347-1351 (1998).
187. S. Sorgenfrei, C. Y. Chiu, R. L. Gonzalez, Y. J. Yu, P. Kim, C. Nuckolls, and K. L. Shepard, "Label-free single-molecule detection of DNA-hybridization kinetics

with a carbon nanotube field-effect transistor," Nature Nanotechnology **6**, 125-131 (2011).
188. Y. C. Cao, R. Jin, and C. A. Mirkin, "Nanoparticles with Raman spectroscopic fingerprints for DNA and RNA detection," Science **297**, 1536-1540 (2002).
189. H. Im, K. C. Bantz, N. C. Lindquist, C. L. Haynes, and S. H. Oh, "Vertically Oriented Sub-10-nm Plasmonic Nanogap Arrays," Nano Lett **10**, 2231-2236 (2010).
190. W. E. Doering and S. M. Nie, "Spectroscopic tags using dye-embedded nanoparticles and surface-enhanced Raman scattering," Anal Chem **75**, 6171-6176 (2003).
191. Y. Lu, G. L. Liu, J. Kim, Y. X. Mejia, and L. P. Lee, "Nanophotonic crescent moon structures with sharp edge for ultrasensitive biomolecular detection by local electromagnetic field enhancement effect," Nano Lett **5**, 119-124 (2005).
192. D. K. Lim, K. S. Jeon, H. M. Kim, J. M. Nam, and Y. D. Suh, "Nanogap-engineerable Raman-active nanodumbbells for single-molecule detection," Nat Mater **9**, 60-67 (2010).
193. T. Kang, S. M. Yoo, I. Yoon, S. Y. Lee, and B. Kim, "Patterned multiplex pathogen DNA detection by Au particle-on-wire SERS sensor," Nano Lett **10**, 1189-1193 (2010).
194. H. N. Wang, A. Dhawan, Y. Du, D. Batchelor, D. N. Leonard, V. Misra, and T. Vo-Dinh, "Molecular sentinel-on-chip for SERS-based biosensing," Phys Chem Chem Phys **15**, 6008-6015 (2013).
195. H. N. Wang, A. M. Fales, A. K. Zaas, C. W. Woods, T. Burke, G. S. Ginsburg, and T. Vo-Dinh, "Surface-enhanced Raman scattering molecular sentinel nanoprobes for viral infection diagnostics," Analytica chimica acta **786**, 153-158 (2013).
196. H. N. Wang and T. Vo-Dinh, "Multiplex detection of breast cancer biomarkers using plasmonic molecular sentinel nanoprobes," Nanotechnology **20**, 065101 (2009).
197. J. Qi, P. Motwani, M. Gheewala, C. Brennan, J. C. Wolfe, and W. C. Shih, "Surface-enhanced Raman spectroscopy with monolithic nanoporous gold disk substrates," Nanoscale **5**, 4105-4109 (2013).
198. P. G. Etchegoin, M. Meyer, and E. C. Le Ru, "Statistics of single molecule SERS signals: is there a Poisson distribution of intensities?," Phys Chem Chem Phys **9**, 3006-3010 (2007).
199. J. Kneipp, H. Kneipp, and K. Kneipp, "SERS - a single-molecule and nanoscale tool for bioanalytics," Chem Soc Rev **37**, 1052-1060 (2008).
200. S. W. Dutse and N. A. Yusof, "Microfluidics-Based Lab-on-Chip Systems in DNA-Based Biosensing: An Overview," Sensors **11**, 5754-5768 (2011).
201. P. Lin, X. T. Luo, I. M. Hsing, and F. Yan, "Organic Electrochemical Transistors Integrated in Flexible Microfluidic Systems and Used for Label-Free DNA Sensing," Adv Mater **23**, 4035-+ (2011).
202. J. Wang, D. Onoshima, M. Aki, Y. Okamoto, N. Kaji, M. Tokeshi, and Y. Baba, "Label-Free Detection of DNA-Binding Proteins Based on Microfluidic Solid-State Molecular Beacon Sensor," Anal Chem **83**, 3528-3532 (2011).

203. A. Barik, L. M. Otto, D. Yoo, J. Jose, T. W. Johnson, and S.-H. Oh, "Dielectrophoresis-Enhanced Plasmonic Sensing with Gold Nanohole Arrays," Nano Lett **14**, 2006-2012 (2014).